Multi-phase flow modeling of
soil contamination and soil remediation

945425

Multi-phase flow modeling of
soil contamination and soil remediation

M.I.J. van Dijke

N*W*O

Cover: Air saturation contours during air sparging in a layered soil. Light blue indicates low saturations and dark blue indicates high saturations.

Stellingen

1. Om de beweging van een drijflaag van organische verontreiniging onafhankelijk van de waterbeweging te analyseren, wordt vaak aangenomen dat de waterdrukgradiënten in horizontale richting verwaarloosbaar zijn. Deze aanname wordt niet gerechtvaardigd door een groot verschil tussen de verticaal geïntegreerde mobiliteiten van water en organische vloeistof, zoals Bear veronderstelt, maar door een groot verschil tussen de lokale mobiliteiten.

   J. Bear, Transport in Porous Media 25, pag. 283-311.

2. De dipool-oplossing van de poreuze-media-vergelijking in twee ruimtelijke dimensies geeft in veel gevallen een goede beschrijving van de onttrekking van een drijflaag van organische verontreiniging in een drie-dimensionaal domein.

3. Bij persluchtinjectie in een homogene of in een horizontaal gelaagde bodem heeft het injectiedebiet vrijwel geen effect op de invloedsstraal van geïnjecteerde lucht.

   Dit proefschrift.

4. Persluchtinjectie in een horizontaal gelaagde bodem leidt bij overgang van een goed doorlatende naar een slecht doorlatende laag tot een toename van de invloedsstraal van geïnjecteerde lucht. Een model waarin voor beide lagen intree-drukken voor lucht zijn opgenomen, geeft aanleiding tot een stationaire toestand waarin de invloedsstraal oneindig is, terwijl een model zonder intree-drukken een eindige invloedsstraal voorspelt.

5. Stolling van halfgeleidermateriaal door warmteafvoer via de randen van het koelingsapparaat wordt beschreven door het Stefan probleem. In tegenstelling tot de één-dimensionale benadering van dit probleem geeft de meer-dimensionale beschrijving geen aanleiding tot het ontstaan van 'mushy' gebieden waar de vaste en vloeibare fase in thermisch evenwicht naast elkaar bestaan.

6. Automatisering en computertechnologie hebben het leven sneller en meer gespannen gemaakt, omdat we onze tijd niet langer hoeven te besteden aan het tijdrovende routinewerk waarmee onze grootouders hun geest ontspanden.

   J.I. Packer, Oppervlakkigheid troef?

7. De 'suggestiestrook' langs de rijbaan suggereert meer voor automobilisten dan voor fietsers.

8. De eenmalige overwinning van Deep Blue op Kasparov geeft alleen aan dat de schaakcomputer een gelijkwaardige tegenstander van de menselijke schaker is geworden.

9. De toegepast wiskundige moet tijdens zijn opleiding ook iets meekrijgen van het fundamentele raamwerk dat zich bevindt achter de foefjes en regeltjes die tijdens de opleiding worden geleerd.

   Naar een uitspraak van **F. den Hollander, Trouw, 25 juni 1997.**

10. De keuze om over te gaan van een traditionele kerk naar een evangelische groepering, of omgekeerd, wordt voornamelijk bepaald door iemands karakter.

Stellingen behorend bij het proefschrift **Multi-phase flow modeling of soil contamination and soil remediation.** Rink van Dijke, 5 december 1997.

Abstract

Van Dijke, M.I.J., 1997, **Multi-phase flow modeling of soil contamination and soil remediation**, Doctoral thesis, Wageningen Agricultural University, The Netherlands.
ISBN 90-5485-802-8, 149 pages.

In this thesis multi-phase flow models are used to study the flow behavior of liquid contaminants in aquifers and of gases that are injected below the groundwater table for remediation purposes. Considered problems are redistribution of a lens of light nonaqueous phase liquid (LNAPL) on a horizontal water table with emphasis on the effect of NAPL entrapment by water and its removal through a well with appropriate multi-phase seepage conditions at the well boundary. In addition, air injection into groundwater (air sparging) in a homogeneous soil and in a layered soil are modeled. Accurate but very time-consuming numerical simulations for the various problems are performed. For further analysis appropriate reductions are made. Assuming vertical equilibrium and vertical averaging of the flow equations reduce the geometrical dimensionality of the LNAPL lens problems and of the problem of air sparging in a layered soil. The air sparging problems are analyzed at steady state, which eliminates the time dependence. Sparging in a homogeneous soil admits further reduction by neglecting capillary forces in vertical direction. For all problems the resulting equations are of nonlinear diffusion type, that can be cast into the porous medium equation. For the various problems similarity solutions to the porous medium equation exist, that show good agreement with numerical results. These analytical solutions give the main features of the spreading velocity of an LNAPL lens and the amount of NAPL that becomes trapped, of the LNAPL removal rate and the extension of the remaining NAPL in case of extraction, and of the air sparging radius of influence in a homogeneous and in a layered soil.

Additional index words: soil remediation, multi-phase flow, vertical flow equilibrium, fluid entrapment, fluid extraction, air sparging, numerical modeling, porous medium equation, similarity solutions.

Contents

The contents of this thesis are based on the following self-contained papers:

Section 1.9 Van Dijke, M.I.J., Horizontal redistribution of oil and water in-
volving oil entrapment (technical note). *Adv. Water Resour.*, submitted.

Chapter 2 Van Dijke, M.I.J. & Van der Zee, S.E.A.T.M., A similarity solu-
tion for oil lens redistribution including capillary forces and oil entrap-
ment. *Transport in Porous Media*, in press.

Chapter 3 Van Dijke, M.I.J. & Van der Zee, S.E.A.T.M., Analysis of oil
lens removal by extraction through a seepage face. *Comp. Geosciences.*,
submitted.

Chapter 4 Van Dijke, M.I.J., Van der Zee, S.E.A.T.M. & Van Duijn, C.J.,
Multi-phase flow modeling of air sparging. *Adv. Water Resour.*, **18**
(1995) 319-333.

Chapter 5 Van Dijke, M.I.J. & Van der Zee, S.E.A.T.M., Modeling of air
sparging in a layered soil: numerical and analytical approximations.
Water Resour. Res., in press.

Chapter 1

General introduction

1.1 Soil contamination and soil remediation

An important threat of our environment is pollution of the soil. Since con-
taminants may adsorb to soil particles or remain trapped in soil pores and
desorb or dissolve slowly, they can affect crops and infiltrate into the ground-
water for years or even decades. Therefore, remediation of contaminated soils,
preferably on-site or in-situ, has high priority. Effective clean-up requires
knowledge about the contaminant, the soil and the remediation techniques.
Below we discuss several important issues that are considered in this thesis.

One class of contaminants is commonly referred to as nonaqueous phase
liquids (NAPL's): organic fluids that are slightly miscible with water. The
behavior of NAPL's after infiltration into the soil leads to consideration of two
important types of these fluids: the NAPL may accumulate at the groundwater
table in the form of so called lenses, if it is lighter than water (LNAPL), or the
NAPL may infiltrate downward to deeper soil layers, if it is heavier than water
(DNAPL). A LNAPL lens further spreads out along the water table and may be
moved in the direction of groundwater flow. For the two NAPL classes differ-
ent soil remediation techniques are required. Both NAPL types may become
immobile by entrapment, i.e. the NAPL is fixed in the soil pore structure as
discrete drops enclosed by water. The mobile fraction of the NAPL may be
removed by classical pumping methods, but pumping may enlarge the NAPL
invaded region and thus increase the potential for entrapment.

Trapped NAPL is removed in-situ by remobilization, e.g. by adding deter-
gents that reduce fluid surface tension, by bioremediation or by volatilization.
Volatilization and in many cases also bioremediation require injection of gas
c.q. oxygen into the soil. Gas flushing in the vadose zone is commonly referred
to as bioventing, whereas gas injection below the groundwater table is called
(air) sparging. Remediation by sparging is a relatively cheap method that has
become very popular in the last decade. However, gas flow in groundwater is

1

quite unpredictable, because the large density and viscosity ratios of gas and water cause unstable flow patterns, that are very sensitive to soil heterogeneity.

Mechanical soil clean-up methods, which we distinguish from chemical and biotechnological processes, depend not only on fluid properties, but are also greatly affected by soil structure. Variations in soil properties such as permeability and porosity, always affect fluid flow. Due to geological processes these variations are usually not completely random, but they are structured. In many cases these patterns concern almost horizontal layers. As a result infiltrated DNAPL spreads out horizontally on top of a low permeable layer and the flow pattern of injected air is deflected just below such a layer.

The mechanical remediation methods always use either injection or extraction wells. Although sometimes horizontally drilled wells are used, which may inject or extract more effectively, vertical wells are most commonly used, because they are much simpler to install. The depth and the length of the well filter may regulate the remediation technique. Furthermore, at injection wells the required rate and composition of injected gas or fluid can be prescribed, although high rates may cause soil deformations. At extraction wells, however, only the total rate but not the composition of extracted fluid can be imposed, which means that in the worst case only water instead of NAPL is removed.

1.2   Multi-phase flow modeling

To analyze the above described processes, multi-phase flow models are used. These models have been developed in oil reservoir engineering, e.g. see [3, 14], and are commonly used for environmental problems as well, e.g. see [1, 9, 35]. In multi-phase flow models gas, water and NAPL are considered as three immiscible phases, whose pressures are related through capillary pressures. The affinity of the phases to infiltrate in soil pores (the wettability) increases in the order gas, NAPL, water. The phases are allowed to coexist in the pores, which leads macroscopically to fluid saturations, i.e. the fractions of pore volume filled with a fluid, that vary between zero and one. In the analyses of this thesis we assume additionally incompressibility of the phases. Flow is described by the phase mass balances and by Darcy's law, that specify the phase velocities. Saturations and capillary pressures, and relative permeabilities and saturations are coupled by constitutive relations.

Since multi-phase flow models are developed for flow in oil reservoirs, simultaneous flow of NAPL and water is reasonably well understood and has been studied extensively. Combination with the third, gaseous, phase in the unsaturated zone is more complicated and is still under investigation [9, 11]. Natural events, such as rainfall and seasonal fluctuation of the water table, cause variations of the water saturation, which variations are hysteretic and

involve fluid entrapment, e.g. see [23, 51]. Hysteresis and fluid entrapment are accounted for in multi-phase flow models, specifically in the constitutive relations [37, 38, 48].

Another complication is the appropriate definition of the outflow conditions at a well or a ditch, where fluid is extracted. The concept behind the conditions stems from classical studies on water seepage, like the dam problem [9, 18]. The latter describes outflow of water from a dam that separates two water reservoirs of different water levels, at the side of the dam where the water level is lowest. At this side the position of the water table, the length of the so called seepage face and the water outflow rate are a priori unknown. Most studies on seepage faces neglected for simplicity the unsaturated zone, assuming a sharp interface between air and water. Including an unsaturated zone requires at the dam boundary a condition that prescribes either a pressure, at the saturated part, or no outflow, at the unsaturated part. Incorporation of a second fluid phase, NAPL, at this boundary, which is the well or ditch in our case, requires similar conditions [14, 24]. The resulting NAPL outflow may, however, occur at very small saturations, which introduces additional computational difficulties.

Application of multi-phase flow modeling to air sparging is not straight-forward. Until recently, not much was known about the nature of air flow in groundwater. With respect to air phase continuity, it was postulated that air flow occurs as moving isolated bubbles, but it turned out that this happens only for very coarse media [34, 32]. Furthermore, air flow likely occurs through small channels, i.e. so called preferential flow paths in regions with relatively large permeabilities [15, 62]. Assuming that the density of these flow paths is sufficiently large, the air flow can be regarded macroscopically as continuous. Another rigorous assumption concerns air compressibility, which is generally not negligible, but is small under most sparging conditions [41]. Further-more, air is certainly not immiscible with fluids phases, but the investigation of sparging by multi-phase flow modeling is still a reasonable first approach, see also [43, 46]. If the air flow field is known, a more complete description of clean-up by air sparging can be given by coupling the multi-phase flow model to transport models that incorporate, for example, air dissolution in water, NAPL volatilization in air and reaction of oxygen and contaminant [57, 62].

Although the term multi-phase flow indicates flow of more than one phase, in many cases the behavior of one of the phases dominates the flow process. In the LNAPL flow problems the air mobility is much larger than the liquid mobil-ities. Hence, neglecting air pressure gradients still yields a good description of the flow process. According to this assumption, which is called the Richards assumption [56], air flow can be eliminated from the description of flow. Fur-thermore, LNAPL and water movement often happen at vertical equilibrium,

which means that vertical flow velocities are negligible, e.g. see [9, 65]. If additionally the water saturations and thus the water mobilities are much larger than the NAPL mobilities, water and NAPL flow are segregated and water flow can be eliminated [10]. Analysis of air sparging shows similarly that only considering the air flow leads to a very good description of the entire flow process.

1.3   Outline of the thesis

Two chapters of this thesis deal with behavior of LNAPL on the water table and two chapters concern air sparging. Chapter 2 describes redistribution of a LNAPL lens on a horizontal water table with emphasis on the effect of NAPL entrapment. We aim at finding the spreading velocity of the lens and the amount of NAPL that becomes trapped. Chapter 3 deals with removal of LNAPL through an extraction well with special attention to the incorporation of multi-phase seepage conditions. The aim is to obtain the removal rate and the extension of the remaining NAPL. Chapter 4 presents and analyzes a multi-phase flow model for air sparging in a homogeneous soil and Chapter 5 describes air sparging in a layered soil. For the effectiveness of sparging it is crucial to determine the horizontal extension of injected air. Solutions to all of these problems are obtained by numerical and analytical methods and provide quantitative information that supports optimization of the soil remediation techniques.

In the following sections of this introduction we discuss the main features of the thesis. In Section 1.4 we present the basic formulation of our multi-phase flow model. Section 1.5 introduces the numerical method, which is used for computing solutions to the general model of Section 1.4. For the specific contamination and remediation cases the global model is reduced to subproblems that can be treated mathematically, as indicated in Section 1.6. Most of the reduced problems admit so called similarity solutions. These explicit or almost explicit analytical solutions are presented in Section 1.7. In Section 1.8 we discuss the criteria for the applicability of the analytical solutions to the non-reduced problems. As an illustrative example Section 1.9 shows how a relatively simple flow problem involving NAPL entrapment is solved by a similarity solution.

1.4   General model

The multi-phase flow model consists basically of the mass balance equations

$$\phi \frac{\partial S_j}{\partial T} + \frac{1}{R^{N-1}} \frac{\partial}{\partial R} \left(R^{N-1} U_j \right) + \frac{\partial}{\partial Z} V_j = 0, \quad j = w, n, \qquad (1.1)$$

with $N = 1, 2$, and Darcy's Law

$$U_j \;=\; -\frac{K_{abs}\,k_{rj}}{\mu_j}\frac{\partial\,P_j}{\partial\,R} \tag{1.2}$$

$$V_j \;=\; -\frac{K_{abs}\,k_{rj}}{\mu_j}\left(\frac{\partial\,P_j}{\partial\,Z}+\rho_j\,g\right),\quad j=w,n, \tag{1.3}$$

for both the wetting (w) and the non-wetting (n) phase. T is time and R and Z are the horizontal and vertical coordinates respectively, where $N = 1$ represents a planar and $N = 2$ an axisymmetric two-dimensional domain. S_j is the effective phase saturation, U_j and V_j are phase horizontal and vertical flow velocities respectively, P_j is phase pressure, ρ_j phase density, k_{rj} phase relative permeability, μ_j phase viscosity, ϕ porosity, K_{abs} absolute permeability and g gravitation. For the two-phase problem of air sparging water is the wetting and air the non-wetting phase. For the three-phase problem involving LNAPL the latter is the non-wetting phase and air is the third phase. Air is present with saturation S_a and has constant pressure $(P_a = 0)$ due to the Richards assumption, such that the equations for two phases analyze the flow sufficiently.

To describe three-phase flow completely including possible non-wetting phase entrapment, it is convenient [48] to define additionally total fluid saturation S_t, trapped non-wetting phase saturation S_{nt}, free non-wetting phase saturation S_{nf}, apparent water saturation S_{wa} and the capillary pressures P_{nw} and P_{an}, which satisfy the relations

$$\begin{aligned}
S_w + S_n &= S_t \\
S_t + S_a &= 1 \\
S_w + S_{nt} &= S_{wa} \\
S_{nf} + S_{nt} &= S_n \\
P_{nw} &= P_n - P_w \\
P_{an} &= -P_n.
\end{aligned} \tag{1.4}$$

The definition of S_{wa} reflects that trapped NAPL is enclosed by the water phase and S_{wa} coincides with S_w if $S_{nt} = 0$. For the constitutive relations we take functions that were originally developed by van Genuchten and that were extended for multi-phase flow by Parker and Lenhard [47]. For the hysteretic relation between capillary pressures and saturations we use [48]

$$S_{wa} \;=\; \begin{cases}
1 & \text{if } P_w > 0 \text{ and } P_n < P_w \\[2mm]
\left(1+\left(\dfrac{\alpha_{nw}}{\rho_w\,g}P_{nw}\right)^n\right)^{\frac{1}{n}-1} & \text{if }\begin{cases} 0 < P_w < P_n \ \text{ or} \\ P_w < 0 \text{ and } P_n > \dfrac{1}{\beta_{an}}P_w \end{cases} \\[4mm]
\left(1+\left(\dfrac{-\alpha}{\rho_w\,g}P_w\right)^n\right)^{\frac{1}{n}-1} & \text{if } P_n < \dfrac{1}{\beta_{an}}P_w < 0
\end{cases} \tag{1.5}$$

$$S_t = \begin{cases} 1 & \text{if } P_n > 0 \text{ or } P_w > 0 \\ \left(1 + \left(\dfrac{\alpha_{an}}{\rho_w g} P_{an}\right)^n\right)^{\frac{1}{n}-1} & \text{if } \dfrac{1}{\beta_{an}} P_w < P_n < 0 \\ S_{wa} & \text{if } P_n < \dfrac{1}{\beta_{an}} P_w < 0, \end{cases} \qquad (1.6)$$

where $\alpha > 0$ and $n > 1$ are van Genuchten soil parameters. Furthermore, $\alpha_{nw} = \alpha \beta_{nw}$ and $\alpha_{an} = \alpha \beta_{an}$, where β_{nw} and β_{an} are the ratios of the NAPL-water and the air-NAPL to the air-water surface tensions, with $\dfrac{1}{\beta_{nw}} + \dfrac{1}{\beta_{an}} = 1$. The latter of relations (1.5) specifies the water saturation in parts of the domain where NAPL is absent. Relative permeabilities satisfy [38]

$$k_{rw} = S_w^{\frac{1}{2}} \left(1 - \left(1 - S_w^{\frac{n}{n-1}}\right)^{1-\frac{1}{n}}\right)^2 \qquad (1.7)$$

$$k_{rn} = (S_t - S_{wa})^{\frac{1}{2}} \left(\left(1 - S_{wa}^{\frac{n}{n-1}}\right)^{1-\frac{1}{n}} - \left(1 - S_t^{\frac{n}{n-1}}\right)^{1-\frac{1}{n}}\right)^2 . \qquad (1.8)$$

We employ the simplified model for entrapment [36], accounting only for non-wetting phase entrapment by water, that may predict a positive trapped saturation only at locations where NAPL has been present, according to

$$S_{nt} = \begin{cases} \dfrac{1 - S_w^{min}}{1 + F_L (1 - S_w^{min})} - \dfrac{1 - S_{wa}}{1 + F_L (1 - S_{wa})} & \text{if } S_{wa} > S_w^{min} \\ 0 & \text{if } S_{wa} = S_w^{min}, \end{cases} \qquad (1.9)$$

whereas the minimum water saturation S_w^{min} is given by

$$S_w^{min}(R, Z, T) = \min_{T' \leq T} S_w(R, Z, T'). \qquad (1.10)$$

Land's factor [37], F_L is given by

$$F_L = \frac{1}{S_{nr}^{max}} - 1, \qquad (1.11)$$

where S_{nr}^{max} is the maximum residual NAPL saturation. Observe that relation (1.9) predicts only trapped NAPL if at some earlier time the water saturation has been smaller, which is usually the case if NAPL recedes. Hence, the relation for S_{nt} is implicitly dependent on time and brings hysteresis in equations (1.1), (1.2) and (1.3). An example of the hysteretic relation between capillary pressure and saturation is shown in Figure 1.4 of Section 1.9.

For two-phase flow we have always $S_t = 1$ instead of relations (1.6). Hence, relation (1.5) reduces to

$$S_{wa} = \begin{cases} 1 & \text{if } P_n < P_w \\ \left(1 + \left(\dfrac{\alpha}{\rho_w\, g}\, P_{nw}\right)^n\right)^{\frac{1}{n} - 1} & \text{if } P_n > P_w. \end{cases} \quad (1.12)$$

and relations (1.7) and (1.8) to

$$k_{rw} = S_w^{\frac{1}{2}} \left(1 - \left(1 - S_w^{\frac{n}{n-1}}\right)^{1 - \frac{1}{n}}\right)^2 \quad (1.13)$$

$$k_{rn} = (1 - S_{wa})^{\frac{1}{2}} \left(1 - S_{wa}^{\frac{n}{n-1}}\right)^{2\left(1 - \frac{1}{n}\right)}. \quad (1.14)$$

Soil heterogeneity is included by spatial dependence of the parameter α and the absolute permeability K_{abs}. Defining for some location in the soil reference values $\bar{\alpha}$ and $\bar{K}_{abs}$ and defining a spatially variable function $\gamma(R)$, the spatially variable α and K_{abs} satisfy the relations

$$\alpha = \gamma(R)\, \bar{\alpha} \quad \text{and} \quad K_{abs} = \gamma^2(R)\, \bar{K}_{abs}. \quad (1.15)$$

This dependence on spatial heterogeneity is in agreement with the scaling theory of similar media, which relates both capillary pressure and absolute permeability to the soil pore size [40, 44].

We choose to combine equations (1.1), (1.2) and (1.3) into the so called Richards equations

$$\phi\, \frac{\partial S_j}{\partial T} - \frac{1}{R^{N-1}}\, \frac{\partial}{\partial R}\left(R^{N-1}\, K_j\, \frac{\partial P_j}{\partial R}\right) - \frac{\partial}{\partial Z}\left(K_j\, \frac{\partial P_j}{\partial Z}\right) - \rho_j\, g\, \frac{\partial K_j}{\partial Z} = 0, \quad (1.16)$$

for $j = w, n$, where we have introduced the phase mobility $K_j = \dfrac{K_{abs}\, k_{rj}}{\mu_j}$ for convenience. Equations (1.16) together with the constitutive relations must be solved for the variables S_j and P_j due to appropriate boundary and initial conditions. These equations are implemented in our numerical model.

1.5 Numerical method

Equations (1.16) for a two-dimensional planar or axisymmetric domain together with the hysteretic and spatially dependent constitutive relations have been implemented in a numerical code. The flow domain is discretized by linear triangular finite elements and time discretization is fully implicit. The

numerical model is based on the mixed form of the Richards equation, i.e. the formulation of equations (1.16), which involves both saturation and pressure, instead of either a pressure based or a saturation based form. This mixed formulation admits the so called modified Picard method [13, 35], which solves the resulting nonlinear system of algebraic equations by a simple Picard iteration. The solution method is supposed to take advantage of the mass conservation property of the saturation based formulation, but avoids the problems that arise from degeneracy of the equations if one of the phases is absent and the discontinuities of the saturation if the soil is heterogeneous. Furthermore, the model is able to treat the usual boundary conditions, such as imposing pressures, saturations and flow velocities. In Chapter 5 the implementation of the variational multi-phase seepage face conditions in the numerical code is described.

Numerical simulations were performed for the described contamination and remediation problems, which are mainly used to verify the analytical approximations. The simulations indicate how well the assumptions for the approximations are met and for which range of the physical parameters the analytical solutions are acceptable. Unfortunately, in all cases sufficiently accurate simulations require large computation times, varying from a few hours to a few days.

To get an impression of the cases that are investigated, we present in Figures 1.1 and 1.2 examples of numerical results for the various contamination and remediation cases. In every situation we consider only $R \geq 0$ for symmetry reasons. Figure 1.1.a shows LNAPL saturations during redistribution including entrapment. The NAPL spreads out to the right and the relatively large NAPL saturations close to the Z-axis are caused by entrapment. Figures 1.1.b and 1.1.c show the LNAPL lens during extraction at the Z-axis. In Figure 1.1.b the domain is unbounded, i.e. NAPL can freely spread out to the right, whereas in Figure 1.1.c the domain has an impermeable boundary at the right. Figure 1.2 presents air saturations during steady state air sparging, i.e. when the amount of injected air is equal to the amount of air that leaves the domain at the top. Figure 1.2.a shows sparging in a homogeneous soil and Figure 1.2.b in a layered soil. In the latter case air tends to spread in horizontal direction just below the low permeable top layer. In both cases the dense pattern of horizontal contour lines above $Z = 0$ denotes the original unsaturated zone.

1.6   Reduced equations

Although equations (1.16) can be treated numerically, accurate simulations are very time consuming. Therefore, for the specific contamination and re-
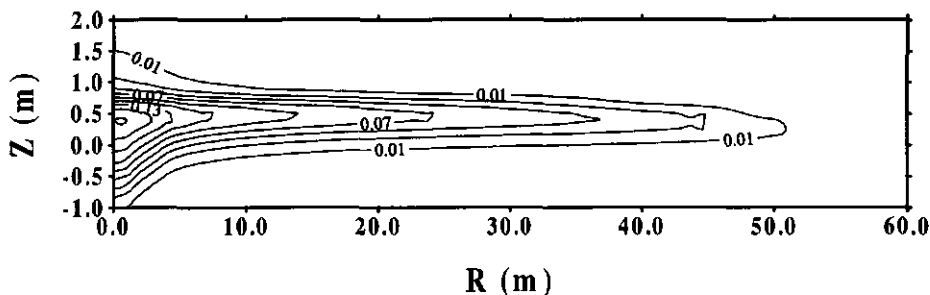
(a)
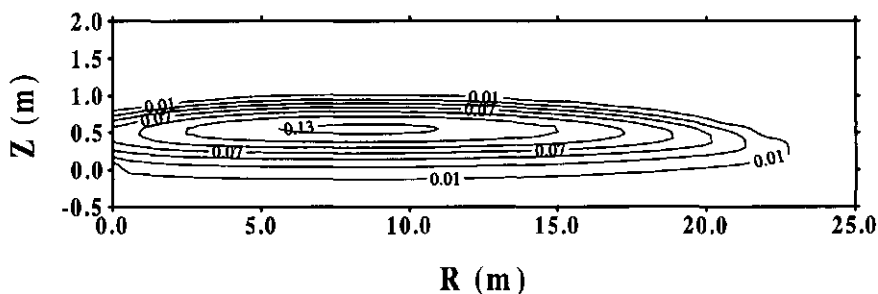
(b)
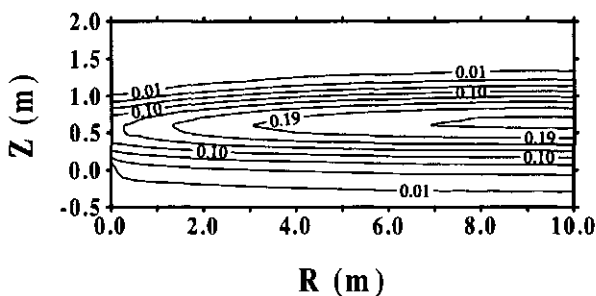
(c)

Figure 1.1: Contour plots of NAPL saturations that are obtained by the numerical model, for (a) redistribution of a LNAPL lens including NAPL entrapment, (b) withdrawal at the Z-axis of LNAPL from an unbounded domain and (c) withdrawal from a bounded domain. In all situations the level $Z = 0$ m denotes the water table.
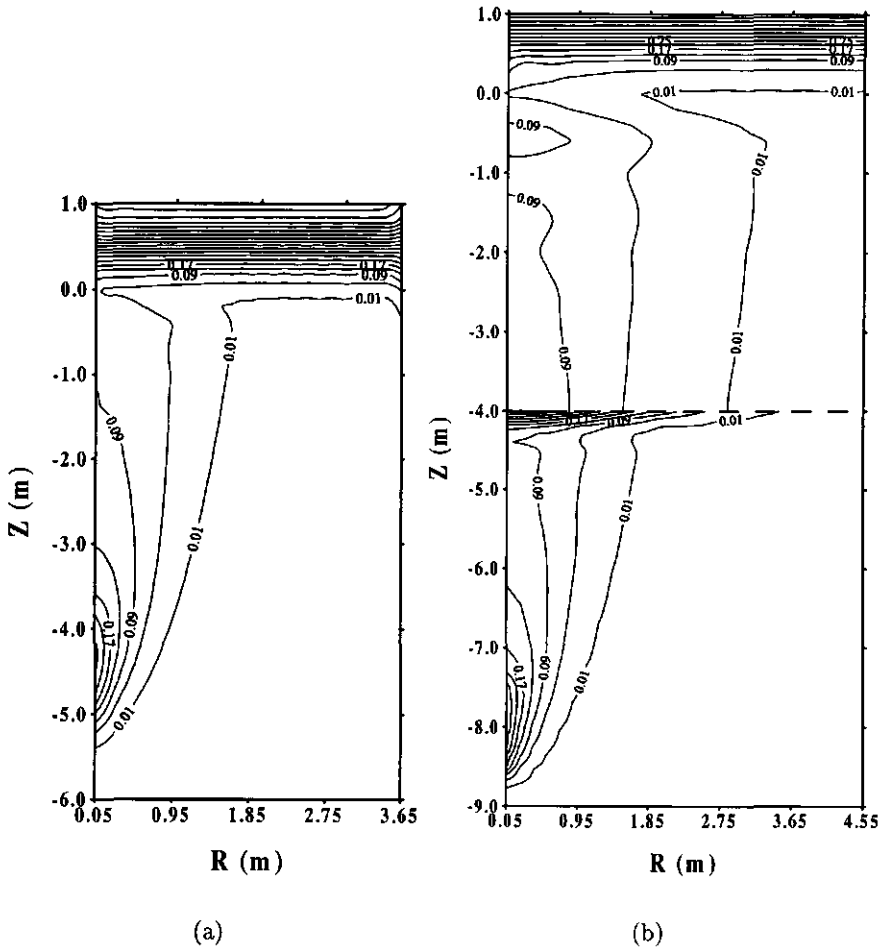
Figure 1.2: Contour plots of air saturations that are obtained by the numerical model for (a) air sparging in a homogeneous soil with a source filter at the Z-axis between $Z = -5.0$ and $Z = -4.0$ m, (b) air sparging in a layered soil with a heterogeneity at $Z = -4.0$ m and a source filter between $Z = -8.5$ and $Z = -7.5$ m. Both domains are axisymmetric and the level $Z = 0$ m denotes the water table.

mediation cases we show how these equations can be reduced by eliminating
equations or terms that are of minor importance, and by decreasing the dimen-
sionality of the problem, such that the resulting subproblems can be further
analyzed and solved. The solutions of the reduced problems usually provide
a better understanding of the specific situations than numerical results and
they provide relatively simple relations between input and output parameters.
Furthermore, they can be used to test the accuracy of numerical codes.

In all considered situations the equation for the water phase in (1.16) can
be neglected, as described in the Section 1.2, by assuming that the water
pressure is distributed hydrostatically, i.e. the pressure varies linearly with
height and is also constant in horizontal direction,

$$P_w = -\rho_w \, g \, Z, \tag{1.17}$$

where we have chosen $Z = 0$ as the level where $P_w = 0$. Using the definition
of capillary pressure $P_{nw} = P_n - P_w$, behavior of the non-wetting phase is
described by

$$\phi \, \frac{\partial S_n}{\partial T} - \frac{1}{R^{N-1}} \frac{\partial}{\partial R} \left(R^{N-1} \, K_n \, \frac{\partial P_{nw}}{\partial R} \right) - \frac{\partial}{\partial Z} \left(K_n \, \frac{\partial P_{nw}}{\partial Z} \right) + \Delta \rho \, g \, \frac{\partial K_n}{\partial Z} = 0, \tag{1.18}$$

where $\Delta \rho = \rho_w - \rho_n$. The four terms of equation (1.18) represent accumu-
lation, capillarity in horizontal direction, capillarity in vertical direction and
gravity effects respectively.

In case of LNAPL movement on a horizontal water table (Figure 1.1) we
assume that the horizontal extension of the lens is much larger than the vertical
extension. As a result, the vertical flow velocities are negligible and capillarity
in vertical direction and gravity effects balance. Hence, the third and fourth
term of equation (1.18) cancel. This situation is referred to as vertical flow
equilibrium [10, 65] for which NAPL pressures are hydrostatically distributed,
yielding

$$P_{nw} = \Delta \rho \, g \, (Z - Z_{nw}), \tag{1.19}$$

where $Z = Z_{nw}(R)$ denotes the level where $P_{nw} = 0$. To eliminate the Z-
dimension the remaining two terms are vertically integrated, e.g. see [10, 31,
49], which leads with (1.19) to

$$F(\frac{\partial W_f}{\partial T}) + \Delta \rho \, g \, \frac{1}{R^{N-1}} \frac{\partial}{\partial R} \left(R^{N-1} \, \bar{K} \, \frac{\partial Z_{nw}}{\partial R} \right) = 0, \tag{1.20}$$

where $W_f = \phi \int S_{nf} \, dZ$ is the free NAPL volume per unit horizontal area
and $\bar{K} = \int K_n \, dZ$ is the vertically averaged conductivity. The piecewise linear
function F represents approximately the hysteretic effect of entrapment and is

derived from the nonlinear relation (1.9) for trapped NAPL. By the constitutive relations and relation (1.19) Z_{nw} can be related to W_f and equation (1.20) is transformed into

$$F(\frac{\partial W_f}{\partial T}) + \Delta \rho g \frac{1}{R^{N-1}} \frac{\partial}{\partial R} \left(R^{N-1} \bar{K}(W_f) \frac{d Z_{nw}}{d W_f}(W_f) \frac{\partial W_f}{\partial R} \right) = 0, \quad (1.21)$$

an equation for $W_f(R, T)$.

For air sparging in a homogeneous medium (Figure 1.2.a) we neglect the accumulation term of equation (1.18) by considering the steady state. Furthermore, because the density difference $\Delta \rho$ is very large, we assume that in vertical direction gravity effects are dominant. This means that the first and the third term of equation (1.18) are negligible, yielding an equation for $K_n(R, Z)$,

$$\frac{1}{R^{N-1}} \frac{\partial}{\partial R} \left(R^{N-1} K_n \frac{d P_{nw}}{d K_n}(K_n) \frac{\partial K_n}{\partial R} \right) - \Delta \rho g \frac{\partial K_n}{\partial Z} = 0, \qquad (1.22)$$

where the constitutive relations provide P_{nw} as a function of K_n.

During air sparging in a soil with a horizontal low permeable layer on top of a high permeable layer the horizontal spreading of air is governed by the air flow in a region just below the low permeable layer. Only across the interface that separates the two layers, say at level $Z = Z^*$, a small vertical flow velocity exists. Therefore, we assume that within the region below the interface the vertical flow velocities are negligible, see Figure 1.2.b. As for the LNAPL flow we have again vertical flow equilibrium with hydrostatically distributed air pressures, which is now given by

$$P_{nw} = P^* + \Delta \rho g (Z - Z^*), \qquad (1.23)$$

in terms of $P^*(R)$, the capillary pressure at the interface. Within this flow region the first, the third and the fourth term of equation (1.18) are negligible. Vertical integration of equation (1.18) yields an equation for $P^*(R)$,

$$\frac{1}{R^{N-1}} \frac{\partial}{\partial R} \left(R^{N-1} \bar{K}(P^*) \frac{\partial P^*}{\partial R} \right) - \gamma^2 (\Delta \rho g)^2 K(\gamma P^*) = 0, \qquad (1.24)$$

where $\tilde{K} = \int_0^{P^*} K(p) \, dp$ and $K(P_{nw}) = K_n(S_w(P_{nw}))$. The term $\gamma^2 (\Delta \rho g)^2 K(\gamma P^*)$ incorporates the small vertical flow velocity across the interface, where $\gamma < 1$ is the degree of heterogeneity between the layers.

Defining the nonnegative functions $D_1(W_f) = -\bar{K}(W_f) \frac{d Z_{nw}}{d W_f}(W_f)$ in equation (1.21), $D_2(K_n) = K_n \frac{d P_{nw}}{d K_n}(K_n)$ in equation (1.22) and $D_3(P^*) =$

$\tilde{K}(P^*)$ in equation (1.24) shows that the three equations can be classified as nonlinear diffusion equations. More specifically, equations (1.21) and (1.22) are both nonstationary diffusion equations if we interpret the Z-coordinate in (1.22) as time, and equation (1.24) is a stationary diffusion-reaction equation, where the second term represents a nonlinear reaction. The three diffusion coefficients satisfy $D_i(0) = 0$, such that the equations may degenerate. This means for the respective problems that in the horizontal domain a bounded region exists where the main variables W_f, K_n and P^* are nonzero and that is enclosed by a free boundary. In other words, the NAPL lens and the cone of injected air always have finite extensions.

1.7 Similarity solutions

Equation (1.24) depends only on one variable (R) and we have to treat it in this form. Equations (1.21) and (1.22) still depend on two variables and can be further reduced.

In the physical problems that have led to equations (1.21) and (1.22) the variables W_f and K_n attain values that are relatively small. For K_n the maximum attainable value is estimated in Section 4.4.1. As a result, the diffusion coefficients D_1 and D_2 are reasonably well approximated by power law functions of the form $D(u) = C u^m$ for $u \geq 0$, with coefficients $C, m > 0$.

After appropriate rescaling, where u denotes the scaled W_f and K_n respectively, equations (1.21) and (1.22) are reformulated in the dimensionless form

$$f\left(\frac{\partial u}{\partial t}\right) = \frac{1}{r^{N-1}} \frac{\partial}{\partial r} \left(r^{N-1} u^m \frac{\partial u}{\partial r}\right), \tag{1.25}$$

where for argument y the function f represents the entrapment as

$$f(y) = \begin{cases} p\,y & \text{if } y > 0 \\ y & \text{if } y \leq 0, \end{cases} \tag{1.26}$$

with $p \geq 1$. For $p = 1$ the left-hand-side side of equation (1.25) becomes the simple time derivative. For $p > 1$ an increase of u with time proceeds different from a decrease, which reflects hysteresis. Equation (1.25) is the (modified) porous medium equation, which mathematical properties have been investigated extensively, e.g. see [2, 52], also with the modified left-hand-side [29].

Air sparging takes place only in an axisymmetric domain, i.e. $N = 2$, without entrapment, i.e. $p = 1$. For LNAPL redistribution we consider both $N = 1$ and $N = 2$, and include entrapment, i.e. $p \geq 1$. In both domains a free boundary, say $r = a(t)$, occurs, which denotes the maximum horizontal

extension of LNAPL and air respectively. The boundary conditions for these problems are

$$\frac{\partial u}{\partial r}(0, t) = 0 \quad \text{and} \quad u(a(t), t) = 0, \tag{1.27}$$

i.e. a no-flow condition and a condition specifying that u vanishes at the free boundary.

For LNAPL removal we consider $N = 1$ and $p \geq 1$ in either an unbounded domain involving a free boundary or in a domain that is bounded to the right, say at $r = l$, see Figures 1.1.b and 1.1.c respectively. On the bounded domain u is everywhere decreasing with time, which means that in this case even for $p > 1$ equation (1.25) is not hysteretic. The removal through the well at $r = 0$ is treated by the condition [7]

$$u(0, t) = 0. \tag{1.28}$$

In the unbounded domain we have again $u = 0$ at the free boundary (1.27) and in the bounded domain a no-flow condition is imposed at $r = l$.

For equation (1.25) a class of similarity solutions exists, i.e.

$$v(r, t) = (t - t_0)^{-\mu} h(\eta) \quad \text{with} \quad \eta = r (t - t_0)^{-\nu}, \tag{1.29}$$

with similarity profile h and parameters μ, ν and t_0. If a free boundary occurs, it is represented by $r = A (t - t_0)^{-\nu}$ with $0 < A < \infty$, thus introducing the additional parameter A. In the bounded domain we set $A \equiv l$ and require $\eta = r$, i.e. $\nu = 0$. Hence, the similarity solution reduces to $v(r, t) = (t - t_0)^{-\mu} h(r)$, which is a simple separation of variables.

Furthermore, substitution of (1.29) in (1.25) yields an ordinary differential equation for $h(\eta)$ for $0 < \eta < A$ and the relation

$$2\nu + m\mu - 1 = 0. \tag{1.30}$$

This implies for the bounded domain that $\mu = \dfrac{1}{m}$ and a solution for h in terms of beta-functions is obtained, which was found by Boussinesq [9] for $m = 2$. For the problems on the unbounded domain we must find a second relation between μ and ν, say for $k = \dfrac{\mu}{\nu}$. It is fairly easy to show that $k = N$ for the redistribution without entrapment and for the sparging problem, i.e. for conditions (1.27) and $p = 1$. Furthermore, the corresponding profile h is an explicit function of η called the Barenblatt-Pattle point source solution [5, 50]. For the LNAPL removal without entrapment, we find $k = N + 1$ and the corresponding profile is the explicit dipole solution [8]. Both solutions for h contain the yet unknown parameter A.

For $p > 1$ we find the value of k by solving the differential equation for $h(\eta)$ numerically. Since the equation is invariant under a scaling with A, the computation yields a transformed solution $\tilde{h}(\xi)$ for $0 < \xi < 1$, which is independent of A. Hence, for both the redistribution and the removal problems the value of k which depends on the value of p, is obtained and the respective profiles $\tilde{h}$ are determined. For the redistribution we have always $k > N$ and for the removal $k > N + 1$.

1.8 Applicability of the similarity solutions

The similarity solutions v (1.29) still contain the unknown parameters A and t_0. These parameters must be determined from the initial conditions of equation (1.25). Unfortunately, the initial conditions in general do not have the similarity shape of v. However, it is proven that for increasing times the shape of u corresponding to arbitrary initial conditions converges reasonably fast to the shape of v [2]. Therefore, we compare u and v at some time after the start of the process and determine the values of A and t_0, such that for all later times good agreement between u and v is guaranteed. To achieve a good comparison we formulate global characteristics of the similarity solution corresponding to data that can also be obtained in practical situations. For example, A could be obtained by comparison of the position of the free boundaries of u and v, but measuring this position is difficult and suffers much from local deviations.

One of the global characteristics is the mass of the solution, i.e. for u of equation (1.25) the $N - 1$st moment of $\int r^{N-1} u\,dr$. Spatially integrating equation (1.25) for $p = 1$ and applying the boundary conditions (1.27) shows mass conservation, i.e. the mass of u is independent of time. Similarly, if for the unbounded domain with $p = 1$ condition (1.28) is imposed, integration shows that the Nth moment $\int r^{N} u\,dr$ is independent of time. Evaluating the equivalent moments of v (1.29) reveals that these are also independent of time, because $\mu = N\nu$ and $\mu = (N+1)\nu$ respectively, which is equivalent to the earlier obtained values $k = N$ and $k = N + 1$ for the respective cases. However, it turns out that these moments for v are special cases of the general moment $M_{k-1} = \int r^{k-1} v\,dr$ which for all $p \geq 1$ is independent of time. As a result, identification of M_{k-1} with its equivalent for u yields an estimation of the value of A independent of t_0.

Furthermore, except for the mass conservative cases of LNAPL redistribution without entrapment and air sparging the mass depends on time and can be used to obtain an approximate value for the time scale t_0. For the removal problem the mass is directly related to the outflow rate, which is easily measured in practice. Only for the mass conservative cases other characteristics must be used to find t_0. For example, for air sparging in a homogeneous soil
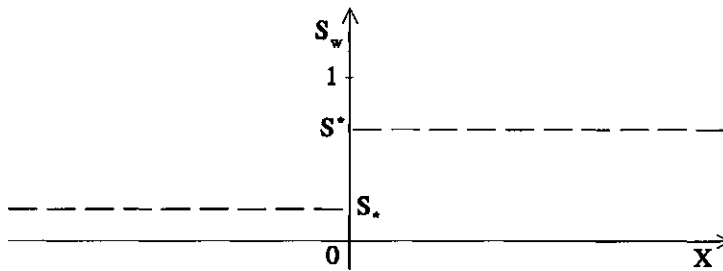
Figure 1.3: Initial water saturations for the one-dimensional redistribution problem.

where the Z-coordinate was interpreted as time, the vertical position of the center-point of the sparging filter is taken for t_0.

Although equation (1.24) for air sparging in a layered soil has a different nature than equation (1.25), computation of its solution can also be completed only by a mass balance argument.

1.9 Horizontal redistribution of NAPL and water involving NAPL entrapment

The effect of NAPL entrapment by water and the use of similarity solutions is illustrated by the following relatively simple problem of horizontal redistribution of NAPL and water. This process can be analyzed analogous to a study of horizontal redistribution of water in a long homogeneous soil column including hysteresis of the capillary pressure function [53]. In this study only flow of water was taken into account, according to Richards assumption for air. The resulting one-dimensional single-phase flow problem started from uniform but different water saturations in the two halves of the column, say $S_w = S_*$ for $X < 0$ and $S_w = S^*$ for $X > 0$ respectively, as shown in Figure 1.3. In [53] a similarity solution was derived for the water saturations during the redistribution. Here we show that this similarity solution is also applicable to the essentially two-phase problem of horizontal redistribution of NAPL and water, even when entrapment of NAPL by water, according to the hysteretic constitutive relations of Section 1.4, is taken into account.

Since the redistribution process involves flow of two phases, i.e. water (w) and NAPL (n), in one horizontal dimension, we obtain from equations (1.2) and (1.3) for the flow velocities

$$U_j = -\frac{K_{abs}\, k_{rj}}{\mu_j} \frac{\partial P_j}{\partial X}, \quad j = w, n. \tag{1.31}$$

However, because no overall flow through the column exists, it follows by a simple mass balance argument that $U_w = -U_n$. Hence, only one of the velocities needs to be found. According to the so called fractional flow approach [9, 14] we subtract equations (1.31) and obtain for the water velocity

$$U_w = -\frac{K_{abs}\,\lambda}{\mu_w}\frac{\partial P_{nw}}{\partial X}, \qquad (1.32)$$

where $P_{nw} = P_n - P_w$ denotes the capillary pressure and

$$\lambda = \frac{k_{rn}\,k_{rw}}{k_{rn} + M\,k_{rw}}, \qquad (1.33)$$

the mobility function with the mobility ratio $M = \dfrac{\mu_n}{\mu_w}$. Since for two-phase flow $S_w + S_n = 1$, we consider only the mass balance equation for water (1.1) in one dimension

$$\phi\frac{\partial S_w}{\partial T} + \frac{\partial U_w}{\partial X} = 0 \quad \text{for } T > 0,\ -\infty < X < \infty. \qquad (1.34)$$

To formulate equation (1.34) with (1.32) as a problem for S_w only, we specify the functions $P_{nw}(S_{wa})$, $k_{rw}(S_w)$ and $k_{rn}(S_{wa})$ by relations (1.12), (1.14) and (1.13), where $S_{wa} = S_w + S_{nt}$ and S_{nt} is given by relation (1.9). Furthermore, we impose initially

$$S_w(X,0) = \begin{cases} S_* & \text{if } X < 0 \\ S^* & \text{if } X > 0, \end{cases} \qquad (1.35)$$

as in Figure 1.3, where the constant S_* and S^* satisfy $0 \le S_* < S^* \le 1$, and we assume that initially no NAPL is trapped.

We introduce the dimensionless variables

$$x = \alpha\,X, \quad t = \frac{K_{abs}\,\rho_w\,g}{\phi\,\mu_w}, \quad u_w = \frac{\mu_w}{K_{abs}\,\rho_w\,g}U_w, \quad p_{nw} = \frac{\alpha}{\rho_w\,g}P_{nw}, \qquad (1.36)$$

where α is defined by equation (1.12). Hence, we obtain

$$\frac{\partial S_w}{\partial t} + \frac{\partial u_w}{\partial x} = 0 \quad \text{for } t > 0,\ -\infty < x < \infty \qquad (1.37)$$

and

$$u_w = -\lambda\frac{\partial p_{nw}}{\partial x}, \qquad (1.38)$$

with

$$S_w(x,0) = \begin{cases} S_* & \text{if } x < 0 \\ S^* & \text{if } x > 0, \end{cases} \qquad (1.39)$$

Furthermore, the dimensionless relation for the capillary pressure according to (1.12) is given by

$$p_{nw}(S_{wa}) = \left(S_{wa}^{\frac{n}{1-n}} - 1 \right)^{\frac{1}{n}} \tag{1.40}$$

Since $S_* < S^*$, for $X < 0$ the water saturation increases as a function of time and NAPL entrapment can occur only in this half of the domain, i.e. according to (1.9)

$$S_{nt} = \begin{cases} \dfrac{1 - S_*}{1 + F_L(1 - S_*)} - \dfrac{1 - S_{wa}}{1 + F_L(1 - S_{wa})} & \text{if } x < 0 \\ 0 & \text{if } x > 0. \end{cases} \tag{1.41}$$

Hence, S_w and S_{wa} are related by

$$S_w = S_{wa} - \frac{1 - S_*}{1 + F_L(1 - S_*)} + \frac{1 - S_{wa}}{1 + F_L(1 - S_{wa})} \quad \text{if } x < 0, \tag{1.42}$$

whereas S_w and S_{wa} coincide if $x > 0$. Typical examples of the resulting capillary pressure and mobility functions, p_{nw} and λ are shown in Figure 1.4 as hysteretic functions of S_w.

By substitution of (1.38) in (1.37) we obtain the nonlinear diffusion equation

$$\frac{\partial S_w}{\partial t} = \frac{\partial}{\partial x} \left(D(S_w) \frac{\partial S_w}{\partial x} \right) \quad \text{for } -\infty < x < \infty \ \ t > 0 \tag{1.43}$$

with the diffusion function

$$D(S_w) = -\lambda \frac{d\, p_{nw}}{d\, S_w}(S_w), \tag{1.44}$$

which has different definitions for $x < 0$ and $x > 0$, according to (1.42).

For all $t > 0$, we require continuity of water velocity u_w and capillary pressure p_{nw} at $x = 0$ [53, 59], whereas by continuity of $p_{nw}(S_{wa})$ (1.40) the latter implies continuity of the apparent water saturation S_{wa} at $x = 0$, i.e.

$$S_{wa}(S_l) = S_r, \tag{1.45}$$

with $S_l(t) = \lim_{x \uparrow 0} S_w(x, t)$ and $S_r(t) = \lim_{x \downarrow 0} S_w(x, t)$. Imposing initial conditions (1.39) to equation (1.43) yields a well-posed problem for S_w.

We solve (1.43) by means of the similarity transformation [53, 60] analogous to (1.29)

$$S_w(x, t) = h(\eta) \quad \text{with } \eta = x\, t^{-\frac{1}{2}}, \tag{1.46}$$
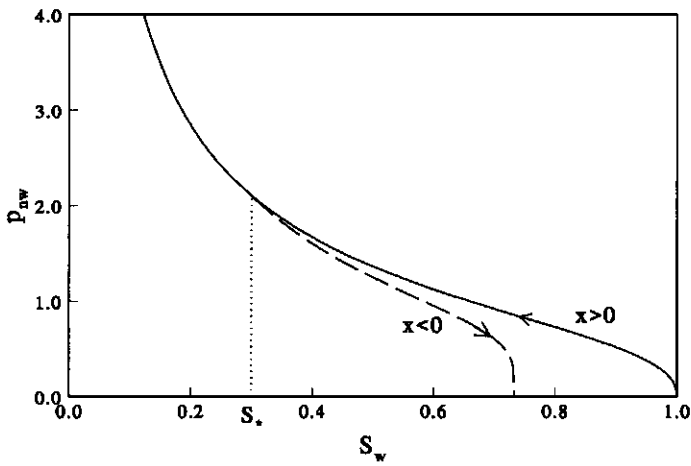
(a)
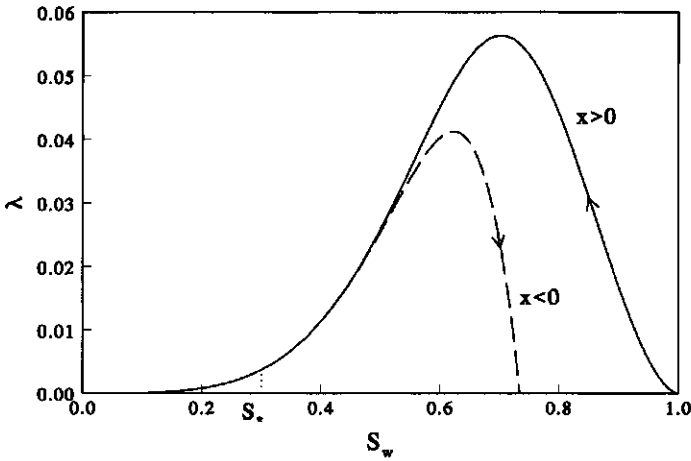
(b)

Figure 1.4: Dimensionless hysteretic capillary pressure (a) and mobility (b) functions of water saturation, with parameters $n = 2.5$, $M = 2.0$, $S_{nr}^{max} = 0.3$, i.e. $F_L = 2.33$, and $S_* = 0.3$. The graphs follow different paths for increasing and decreasing water saturations.
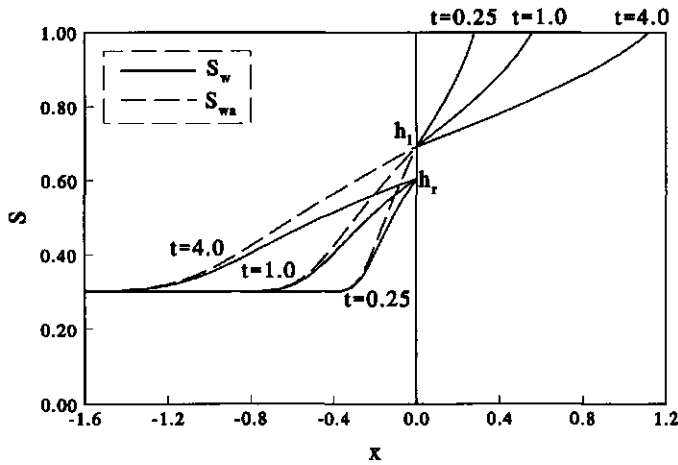
Figure 1.5: Similarity solutions for the water and apparent water saturations at three different times for parameter values $m = 0.6$, $M = 2.0$, $S_{nr}^{max} = 0.3$, i.e. $F_L = 2.33$, $S_* = 0.3$ and $S^* = 1.0$.

where we have taken $t_0 = 0$ in view of the initial conditions at $t = 0$ (1.39). For $h(\eta)$ the ordinary differential equation

$$\frac{1}{2}\eta h' + (D(h)h')' = 0 \quad \text{for} \ -\infty < \eta < \infty \tag{1.47}$$

is obtained. The initial condition (1.39) requires the boundary conditions

$$h(-\infty) = S_* \ \text{ and } \ h(\infty) = S^*. \tag{1.48}$$

At $\eta = 0$ we have continuity of $h_a(h)$ and of $D(h)h'$, where $h_a(h) = S_{wa}(h)$. For $\eta < 0$, h_a is defined by the inverse of relation (1.42), which can be obtained explicitly, and $h_a \equiv h$ for $\eta > 0$. At $\eta = 0$ we define $h_l = \lim_{\eta \uparrow 0} h(\eta)$ and $h_r = \lim_{\eta \downarrow 0} h(\eta)$ analogous to the definition of $S_l(t)$ and $S_r(t)$.

Since h_l and h_r are a priori unknown, numerical solution of equation (1.47) on the two halves $\eta < 0$ and $\eta > 0$ respectively is a nontrivial exercise, which is described in [60] for a redistribution problem where hysteresis occurs due to different material properties at both sides of $\eta = 0$.

In case of degenerate diffusion, i.e. for the present diffusion function (1.44) if $S_* = 0$ or $S^* = 1$ [58] where $D = 0$, we find the finite numbers $\eta_* < 0$ or $\eta^* > 0$, satisfying $h(\eta_*) = S_*$ or $h(\eta^*) = S^*$, with $h(\eta) \equiv S_*$ for $\eta \leq \eta_*$ or $h(\eta) \equiv S^*$ for $\eta \geq \eta^*$, respectively.

For the hysteretic relations of Figure 1.4 we show in Figure 1.5 in dimen-

sionless coordinates for three different times the similarity solution of equation (1.43) for the water saturation $S_w(x,t) = h(\eta)$ and for the apparent water saturation S_{wa}. At $x = 0$ we identify $S_l \equiv h_l$ and $S_r \equiv h_r$. The solution for the trapped NAPL saturation S_{nt} is found as the difference $S_{wa} - S_w$ and for the free NAPL saturation as $1 - S_{wa}$. Observe that for $x > 0$ the curve of S_w attains the value $S^* = 1$ at a finite distance $x = \eta^* t^{-\frac{1}{2}}$ because of the degenerate diffusion.

The study of this geometrically simple problem shows how behavior of one phase may completely determine the entire flow process. Furthermore, although the complicated phenomenon of hysteresis is incorporated, a similarity transformation and an almost explicit solution can be obtained. The similarity solution helps testing numerical models, especially around $x = 0$ and at the location of the free boundary, where discontinuities of the solution or its derivative occur. Finally, the similarity solution facilitates investigation of the effect of varying parameters, such as the spreading velocities of the profile with and without entrapment.

Notation

A	position of free boundary in similarity profile
a	position of free boundary for similarity solution
D_i, D	various diffusion coefficients
$F(f)$	(scaled) trapping function
F_L	Land's factor
g	gravity $[\mathrm{m\,s^{-2}}]$
$h(\tilde{h})$	(scaled) similarity profile
h_a	similarity solution for S_{wa} in Section 1.9
h_l, h_r	values of similarity solution at $\eta = 0$ in Section 1.9
K_{abs}	absolute permeability $[\mathrm{m^2}]$
K_j	phase j conductivity $[\mathrm{m\,s^{-1}}]$
$\bar{K}$, $\tilde{K}$	various averaged NAPL conductivities
k	trapping parameter in similarity profile
k_{rj}	phase j relative permeability
l	dimensionless length of bounded domain
M	mobility ratio
M_{k-1}	dimensionless time-independent moment of free NAPL saturation per unit lateral area
m	power in coefficient of porous medium equation
N	number of horizontal dimensions
n	van Genuchten parameter

P_j	phase j pressure [Pa]
$P_{j,k}$ $(p_{j,k})$	(dimensionless) phases j, k capillary pressure [Pa]
P^*	capillary pressure at interface between soil layers [Pa]
p	trapping constant in function f
$R(r)$	(dimensionless) horizontal coordinate [m]
S_j	phase j saturation
S_l, S_r	saturations at $x = 0$ in Section 1.9
S_{nf}	free non-wetting phase saturation
S_{nt}	trapped non-wetting phase saturation
S_{nr}^{max}	maximum residual non-wetting phase saturation
S_t	total fluid saturation
S_{wa}	apparent water saturation
S_w^{min}	minimum water saturation
S^*, S_*	initial saturations in Section 1.9
$T(t)$	(dimensionless) time [h]
t_0	starting time of similarity solution
$U_j(u_j)$	(dimensionless) phase j horizontal flow velocity [m s^{-1}]
u	variable in porous medium equation
v	similarity solution
V_j	phase j vertical flow velocity [m s^{-1}]
W_f	free NAPL volume per unit lateral area [m]
$X(x)$	(dimensionless) horizontal coordinate [m]
Z	vertical coordinate [m]
Z_{nw}	elevation where P_{nw} is zero [m]
Z^*	vertical position of interface between soil layers [m]
α	van Genuchten parameter [m^{-1}]
β_{an}, β_{nw}	ratios of air-NAPL and NAPL-water to air-water surface tensions
γ	degree of heterogeneity
$\eta(\xi)$	scaled similarity variable
η^*, η_*	positions of free boundaries in Section 1.9
λ	mobility function
μ, ν	powers in similarity solution
μ_j	phase j viscosity [Pa s]
ρ_j	phase j density [kg m^{-3}]
ϕ	porosity

Chapter 2

A similarity solution for oil lens redistribution including capillary forces and oil entrapment

2.1 Introduction

Spills of hydrocarbons have caused contamination of numerous aquifers. Non-aqueous phase liquids that are less dense than water, such as gasoline, (henceforth called oil for brevity) may accumulate as a lens at the phreatic water surface and spread laterally. Spreading of such a lens is due to gravity and both air-oil and oil-water capillary forces. The redistribution often proceeds at near-hydrostatic pressures. At locations within the lens where the water saturation increases, part of the oil becomes trapped as discrete drops enclosed by water. The entrapment affects the redistribution process and causes considerable problems for remediation of contaminated aquifers. Therefore, it is important to predict the lateral extension of oil lenses and the amount and location of trapped oil.

For prediction of oil redistribution, constitutive saturation-capillary pressure and relative permeability-saturation relations are necessary. These relations become complicated when the hysteric entrapment mechanism is included. Parker and Lenhard [38, 48] proposed an extended closed-form model for these constitutive relations. In many situations reduced versions of this model provide reasonable approximations of the flow equations.

A common way to reduce the flow equations is to assume that vertical pressure distributions are hydrostatic, i.e. variables depend only on the difference between the vertical position and a reference elevation, e.g. the level separating the water and the water-oil regions. Using this assumption the vertical dimension of the multi-phase flow problem can be eliminated by vertical integration of variables [9, 49] and only the oil flow equation needs to be considered. Two vertical equilibrium approximations are often used [31]. The simplest is the gravity-segregated flow model with sharp interfaces, without [17, 25, 26] or including [31, 45] trapping effects. This model applies generally during the

early stages of spreading when the oil lens is relatively thick or in relatively coarse porous media, where capillary forces can be neglected. However, a major disadvantage is that the constant oil saturation must be known a priori. More involved is the capillarity-gravity-segregated flow model, where vertical capillary and gravitational forces balance [10, 11].

Kaluarachchi and Parker [36] numerically studied oil redistribution in two dimensions using the three-phase hysteretic constitutive relations [38, 48], where hysteresis was restricted to entrapment of oil by water. Huyakorn e.a. and Wu e.a. [31, 63] numerically investigated three-dimensional spreading of an oil lens using vertical integration. However, their investigation was restricted to the part of the oil lens where only water and oil were present and neglected the three-phase part.

Miller and Van Duijn gave explicit similarity solutions for redistribution without oil entrapment of a two-dimensional axisymmetric oil lens for the gravity-segregated flow model [45]. They included also oil entrapment by water and showed that in this case no explicit solution exists, but that a similarity solution remains, which predicts the lateral area where trapped oil is present. The latter solution was found by Kochina, see [7], who investigated a sharp-interface model for spreading of a water mound during which residual water is left behind.

Recently Bear e.a. [10] presented analytical solutions for spreading of a LNAPL lens on the water table using a capillarity-gravity-segregated flow model.

As accurate numerical computations for oil lens redistribution, which require flow domains of small height (a few meters) and large width (several tens to hundreds of meters), are still far from trivial, approximate analytical solutions can be very helpful. Our scope is to find an analytical solution that provides a reasonable approximation of the full flow model for redistribution of a designated oil volume in a two-dimensional planar or axisymmetric homogeneous domain including both the effect of capillary forces and the effect of oil entrapment. We use the vertical equilibrium assumption of capillarity-gravity-segregated flow to reduce the vertically integrated form of the multi-phase flow constitutive relations [10, 38, 48] and present the criteria for the validity of this assumption. Hysteresis is incorporated by a nonlinear model for oil entrapment in water [36], but we show that under the present conditions the expression for the vertically integrated trapped oil saturation can be reduced. The resulting differential equation admits an analytical solution for the free oil volume per unit lateral area as a function of time and the lateral space coordinate.

To show that the analytical solution provides a good approximation of the oil lens redistribution, we have carried out several illustrative numerical

simulations, which are based on the nonreduced flow model and the nonlinear model for oil entrapment, and compare the results with the analytical solution.

2.2 Model

We use for both water (w) and oil (o) the mass balance equations

$$\phi \frac{\partial S_j}{\partial T} + \frac{1}{R^{N-1}} \frac{\partial}{\partial R}(R^{N-1} U_j) + \frac{\partial}{\partial Z} V_j = 0, \quad j = w, o \qquad (2.1)$$

and Darcy's Law

$$U_j = -\frac{K\,k_{rj}}{\mu_j} \frac{\partial P_j}{\partial R} \qquad (2.2)$$

$$V_j = -\frac{K\,k_{rj}}{\mu_j} \left(\frac{\partial P_j}{\partial Z} + \rho_j\, g \right), \quad j = w, o, \qquad (2.3)$$

where $N = 1, 2$ specifies the lateral dimensionality. T is time and R and Z are the horizontal and vertical coordinates respectively. S_j is effective phase saturation, U_j and V_j are phase horizontal and vertical flow velocities respectively, P_j is phase pressure, ρ_j phase density, k_{rj} phase relative permeability, μ_j phase viscosity, ϕ porosity, K absolute permeability and g gravitation. We assume that the soil is homogeneous and isotropic, that both fluids are incompressible and that air is present with saturation S_a and constant pressure ($P_a = 0$). We define according to [48] total fluid saturation S_t, trapped oil saturation S_{ot}, free oil saturation S_{of}, apparent water saturation S_{wa}, oil-water capillary pressure P_{ow} and air-oil capillary pressure P_{ao}, which satisfy the constitutive relations

$$
\begin{aligned}
S_w + S_o &= S_t \\
S_t + S_a &= 1 \\
S_w + S_{ot} &= S_{wa} \\
S_{of} + S_{ot} &= S_o \\
P_{ow} &= P_o - P_w \\
P_{ao} &= -P_o.
\end{aligned}
$$

For the retention functions we use

$$
S_{wa} = \begin{cases}
1 & \text{if } P_w > 0 \text{ and } P_o < P_w \\[2mm]
\left(1 + \left(\dfrac{\alpha_{ow}}{\rho_w\, g} P_{ow}\right)^n\right)^{\frac{1}{n}-1} & \text{if } \begin{cases} 0 < P_w < P_o \text{ or} \\[1mm] P_w < 0 \text{ and } P_o > \dfrac{1}{\beta_{ao}} P_w \end{cases} \\[4mm]
\left(1 + \left(\dfrac{-\alpha}{\rho_w\, g} P_w\right)^n\right)^{\frac{1}{n}-1} & \text{if } P_o < \dfrac{1}{\beta_{ao}} P_w < 0
\end{cases} \qquad (2.4)
$$

$$
S_t \;=\; \begin{cases}
1 & \text{if } P_o > 0 \text{ or } P_w > 0 \\[2mm]
\left(1 + \left(\dfrac{\alpha_{ao}}{\rho_w\, g}\, P_{ao}\right)^n\right)^{\frac{1}{n}-1} & \text{if } \dfrac{1}{\beta_{ao}} P_w < P_o < 0 \\[4mm]
S_{wa} & \text{if } P_o < \dfrac{1}{\beta_{ao}} P_w < 0,
\end{cases}
\tag{2.5}
$$

where $\alpha > 0$ and $n > 1$ are van Genuchten soil parameters. Furthermore, $\alpha_{ow} = \alpha\,\beta_{ow}$ and $\alpha_{ao} = \alpha\,\beta_{ao}$, where β_{ow} and β_{ao} are the ratios of the oil-water and the air-oil to the air-water surface tensions, with $\dfrac{1}{\beta_{ow}} + \dfrac{1}{\beta_{ao}} = 1$. Relative permeabilities satisfy [38]

$$
k_{rw} \;=\; S_w^{\frac{1}{2}} \left(1 - \left(1 - S_w^{\frac{n}{n-1}}\right)^{1-\frac{1}{n}}\right)^2
\tag{2.6}
$$

$$
k_{ro} \;=\; (S_t - S_{wa})^{\frac{1}{2}} \left(\left(1 - S_{wa}^{\frac{n}{n-1}}\right)^{1-\frac{1}{n}} - \left(1 - S_t^{\frac{n}{n-1}}\right)^{1-\frac{1}{n}}\right)^2.
\tag{2.7}
$$

We employ the simplified model for oil entrapment [36], that may predict a positive trapped oil saturation only at locations where oil has been present, according to

$$
S_{ot} = \begin{cases}
\dfrac{1 - S_w^{min}}{1 + F_L\,(1 - S_w^{min})} - \dfrac{1 - S_{wa}}{1 + F_L\,(1 - S_{wa})} & \text{if } S_{wa} > S_w^{min} \\[4mm]
0 & \text{if } S_{wa} = S_w^{min},
\end{cases}
\tag{2.8}
$$

whereas the minimum water saturation S_w^{min} is given by

$$
S_w^{min}(R, Z, T) = \min_{T' \leq T} S_w(R, Z, T').
\tag{2.9}
$$

Land's factor [37], F_L is given by

$$
F_L = \frac{1}{S_{or}^{max}} - 1,
\tag{2.10}
$$

where S_{or}^{max} is the maximum residual oil saturation.

To describe the redistribution of an oil lens we solve equations (2.1), (2.2) and (2.3) for time $T > 0$ in the domain $R > 0$, $-\infty < Z < \infty$. Defining the Z-axis as the axis of symmetry we impose the no-flow boundary conditions

$$
\left.\begin{array}{rcl}
U_w &=& 0 \\
U_o &=& 0
\end{array}\right\} \quad \text{for } R = 0,\ -\infty < Z < \infty.
\tag{2.11}
$$
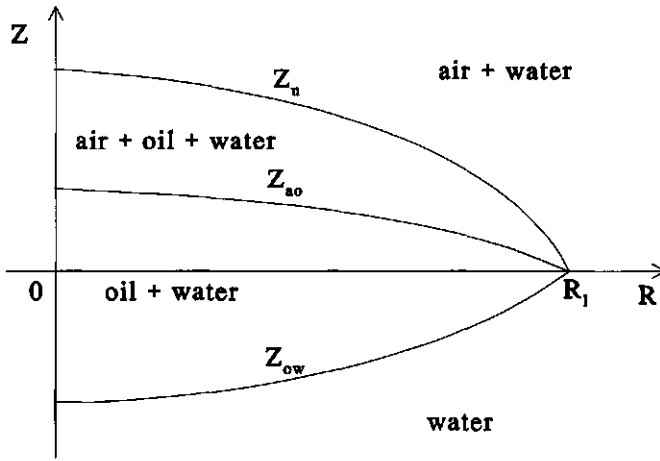
Figure 2.1: Geometry of oil lens.

The free oil is confined to two layers [49] as shown in Figure 2.1. Between the levels $Z = Z_u$ and $Z = Z_{ao}$ water, oil and air are present, whereas between the levels $Z = Z_{ao}$ and $Z = Z_{ow}$ water and oil are present. Z_u, Z_{ao} and Z_{ow} coincide at the water table outside the oil lens $Z = 0$ for $R = R_l$. Hence, $Z_{ow}(R,T)$, $Z_{ao}(R,T)$, $Z_u(R,T)$ and $R_l(T)$ are defined by

$$
\begin{aligned}
S_t &= 1, & S_{of} &= 0 & &\text{if } Z < Z_{ow} \\
S_t &= 1, & S_{of} &> 0 & &\text{if } Z_{ow} < Z < Z_{ao} \\
S_t &< 1, & S_{of} &> 0 & &\text{if } Z_{ao} < Z < Z_u \\
S_t &< 1, & S_{of} &= 0 & &\text{if } Z > Z_u,
\end{aligned}
$$

for $0 < R < R_l$ and $Z_{ow} = Z_{ao} = Z_u = 0$ for $R \geq R_l$. In terms of capillary pressures these levels are given by

$$P_{ow}(Z_{ow}) = 0, \quad P_{ao}(Z_{ao}) = 0, \quad \frac{\beta_{ao}}{\beta_{ow}} P_{ao}(Z_u) = P_{ow}(Z_u). \tag{2.12}$$

Assuming that oil has infiltrated in the domain before $T = 0$, we prescribe an initial oil saturation

$$S_o(R, Z, 0) = \begin{cases} S_i(R,Z) & \text{for } Z_{ow} < Z < Z_u \\ 0 & \text{elsewhere,} \end{cases} \tag{2.13}$$

such that an oil volume

$$V_1 = (2\pi)^{N-1} \phi \int_{-\infty}^{\infty} \int_0^{\infty} R^{N-1} S_i(R,Z) \, dR \, dZ \tag{2.14}$$

is present in the flow domain, where we have also assumed that at $T = 0$ no oil is trapped.

2.3   An approximate analytical solution

2.3.1   Vertical flow equilibrium

For our analysis we assume that the oil lens is at vertical equilibrium and that water and oil flow are segregated. At vertical equilibrium vertical flow velocities are negligible as the result of a balance of vertical capillary and gravitational forces. The corresponding flow pattern is generally referred to as capillarity-gravity segregated and has been analyzed extensively for two-phase flow, see e.g. [31, 65].

For the present three-phase flow process we consider the vertical oil flow velocity V_o that follows from (2.3), in terms of the fractional flow function, see e.g. [9],

$$f_o = \frac{k_{ro}/\mu_o}{k_{ro}/\mu_o + k_{rw}/\mu_w},\qquad(2.15)$$

the vertical total flow velocity $V_t = V_w + V_o$ and the capillary oil-water pressure. This yields

$$V_o = f_o V_t - \frac{K k_{rw}}{\mu_w} f_o \left(\frac{\partial P_{ow}}{\partial Z} - \Delta\rho g\right) \quad \text{for } Z_{ow} < Z < Z_u,\qquad(2.16)$$

where $\Delta\rho = \rho_w - \rho_o$. In the three-phase layer we consider alternatively the vertical oil flow velocity in terms of the capillary air-oil pressure, yielding

$$V_o = \frac{K k_{ro}}{\mu_o} \left(\frac{\partial P_{ao}}{\partial Z} - \rho_o g\right) \quad \text{for } Z_{ao} < Z < Z_u.\qquad(2.17)$$

Consequently, these flow velocities are negligible if the vertical capillary pressure distributions are approximately hydrostatic, i.e.

$$P_{ow} = \Delta\rho g (Z - Z_{ow}), \quad \text{for } Z_{ow} < Z < Z_u\qquad(2.18)$$

$$P_{ao} = \rho_o g (Z - Z_{ao}), \quad \text{for } Z_{ao} < Z < Z_u,\qquad(2.19)$$

where we have used the first and second expressions of definition (2.12). These distributions occur if the lateral extension of the layer where free oil is present, say R_l, is much larger than its thickness [10, 65], i.e.

$$\frac{Z_u - Z_{ow}}{R_l} \ll 1.\qquad(2.20)$$

With the pressure distributions (2.18) and (2.19) we obtain the fractional flow formulations for the lateral oil flow velocities U_o from (2.2), i.e.

$$U_o = f_o U_t + \frac{K k_{rw}}{\mu_w} f_o \Delta\rho g \frac{\partial Z_{ow}}{\partial R} \quad \text{for } Z_{ow} < Z < Z_u\qquad(2.21)$$

$$U_o = -\frac{K k_{ro}}{\mu_o} \rho_o g \frac{\partial Z_{ao}}{\partial R} \quad \text{for } Z_{ao} < Z < Z_u,\qquad(2.22)$$

where $U_t = U_w + U_o$.

Furthermore, we assume that everywhere inside the oil lens, the water mobilities k_{rw}/μ_w are much larger than the oil mobilities k_{ro}/μ_o. Hence, we use the definition of f_o (2.15) to approximate

$$f_o \sim 0 \quad \text{and} \quad \frac{k_{rw}}{\mu_w} f_o \sim \frac{k_{ro}}{\mu_o} \qquad (2.23)$$

in equation (2.21). Because of the large water mobilities we obtain that the water pressure distribution is approximately hydrostatic with $P_w = 0$ for $Z = 0$ at every lateral position, which implies that water and oil flow are segregated.

In view of relations (2.6) and (2.7) the oil mobilities are relatively small if the free oil saturations are small. The latter are everywhere less than $1 - S_{wa}$, whereas inside the oil lens S_{wa} as well as S_t is minimum at $Z = Z_u$. According to relations (2.4) and (2.5) the capillary pressures $P_{ow}(Z_u)$ and $P_{ao}(Z_u)$ must be sufficiently small. Hence, we require that

$$\frac{\alpha_{ow}}{\rho_w \, g} P_{ow}(Z_u) = \frac{\alpha_{ao}}{\rho_w \, g} P_{ao}(Z_u) < 1 \qquad (2.24)$$

or, when we use the pressure distributions (2.18) and (2.19),

$$\alpha_{ow} \, (Z_u - Z_{ow}) \frac{\Delta \rho}{\rho_w} = \alpha_{ao} \, (Z_u - Z_{ao}) \frac{\rho_o}{\rho_w} < 1. \qquad (2.25)$$

Observe that these constraints for the layer thicknesses that are made for the assumption of segregated flow, are rather strict. Alternatively, we may assume that the thickness of the oil lens is much smaller than the depth of the (water) saturated zone of the aquifer. Then, averaging over the depth of the aquifer, the water mobilities are much larger than the oil mobilities, which also justifies a segregated flow approach [10]. In most situations, except for very shallow aquifers, the latter constraint is met earlier.

As the water pressures satisfy $P_w = -\rho_w \, g \, Z$, the separating levels are related according to

$$Z_{ow} = -\frac{\rho_o}{\Delta \rho} Z_{ao}, \quad Z_u = \frac{\beta_{ow}}{1 - D} Z_{ao}, \quad \text{with} \quad D = \frac{\beta_{ow} \, \Delta \rho}{\beta_{ao} \, \rho_o}, \qquad (2.26)$$

where we have used the third expression of definition (2.12). Expressing the layer thicknesses as

$$Z_u - Z_{ow} = \frac{\rho_w}{\Delta \rho} \frac{1}{1 - D} Z_{ao} \quad \text{and} \quad Z_u - Z_{ao} = \frac{\rho_w}{\Delta \rho} \frac{D}{1 - D} Z_{ao} \qquad (2.27)$$

the condition (2.25) coincides to

$$\frac{\alpha_{ow}}{1 - D} Z_{ao} < 1. \qquad (2.28)$$

Furthermore, the expression (2.21) for the oil flow velocity coincides with expression (2.22) depending on Z_{ao} only, which is valid in the entire oil lens.

Combination of equation (2.22) with the oil mass balance equation (2.1) yields one differential equation that describes the entire flow process, i.e.

$$\phi \frac{\partial S_o}{\partial T} - \frac{K \rho_o g}{\mu_o} \frac{1}{R^{N-1}} \frac{\partial}{\partial R} \left(R^{N-1} k_{ro} \frac{\partial Z_{ao}}{\partial R} \right) = 0, \qquad (2.29)$$

where we neglected the vertical flow velocity. Observe that condition (2.28) implies that free oil is confined to a lens of finite thickness [10, 11, 39], if

$$D < 1. \qquad (2.30)$$

We introduce the characteristic lengths and time

$$Z_c = \frac{1 - D}{\alpha_{ow}}, \qquad R_c = \left(\frac{V_1}{(2\pi)^{N-1} Z_c} \right)^{\frac{1}{N}}, \qquad T_c = \frac{R_c \mu_o}{K \rho_o g}, \qquad (2.31)$$

where the definition of Z_c is based on condition (2.28). Hence, we define the dimensionless variables

$$z = \frac{Z}{Z_c}, \qquad r = \frac{R}{R_c}, \qquad t = \frac{T}{T_c}. \qquad (2.32)$$

Similarly, we make Z_{ow}, Z_{ao}, Z_u and R_l dimensionless by scaling with Z_c and R_c. This yields the differential equation

$$\phi \frac{\partial S_o}{\partial t} - \frac{Z_c}{R_c} \frac{1}{r^{N-1}} \frac{\partial}{\partial r} \left(r^{N-1} k_{ro} \frac{\partial z_{ao}}{\partial r} \right) = 0, \qquad (2.33)$$

which provides positive values of $S_{of} = S_o - S_{ot}$ for $0 < r < r_l$, $z_{ow} < z < z_u$ and $t > 0$.

2.3.2   Vertical integration

Because vertical pressure distributions are hydrostatic, we further reduce equation (2.33) by vertical integration, which requires evaluation of

$$w_f = \phi \int_{z_{ow}}^{z_u} S_{of} \, dz = \phi \int_{z_{ow}}^{z_u} (S_t - S_{wa}) \, dz \qquad (2.34)$$

$$\bar{k} = \int_{z_{ow}}^{z_u} k_{ro}(S_{wa}, S_t) \, dz = \int_{z_{ow}}^{z_u} k_{ro}(S_{wa}, S_t) \, dz, \qquad (2.35)$$

where $w_f(r, t)$ represents the free oil volume per unit lateral area and $\bar{k}(r, t)$ the vertically integrated relative permeability [31, 49, 63]. To rewrite equation (2.33) in terms of the variable w_f only, we approximate both $\bar{k}$ and z_{ao}
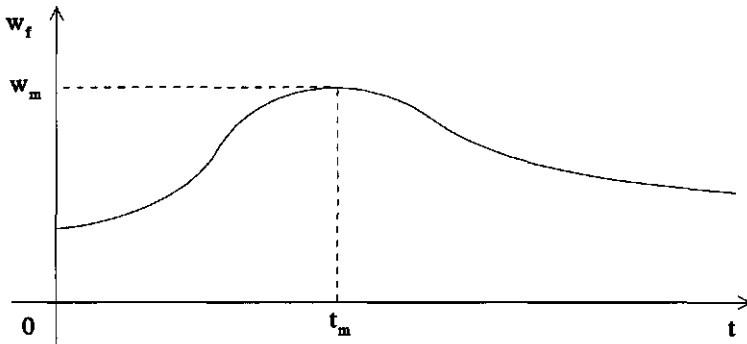
Figure 2.2: Vertically integrated free oil saturation w_f as a function of time during redistribution.

by power law functions of w_f in Appendix 2A. Therefore, we approximate the retention functions (2.4) and (2.5) by power law functions, which is reasonable if condition (2.28) is satisfied. We obtain

$$z_{ao} = \lambda_1 \, w_f^{\frac{1}{n+1}} \quad \text{and} \quad \bar{k} = \lambda_2 \, w_f^{\frac{5n-2}{2\,(n+1)}}, \tag{2.36}$$

where λ_1 and λ_2 are given by (2.75) and (2.76).

Additionally, we define $w_o(r,t)$ as the total oil volume per unit lateral area, $w_t(r,t)$ as the trapped oil volume, whereas $w_t = w_o - w_f$, and $w_m(r,t)$ as the maximum oil volume, i.e.

$$w_m(r,t) = \max_{t' \le t} \, w_f(r,t'). \tag{2.37}$$

The hydrostatic pressure assumption implies that for every lateral position the integrated apparent water saturation attains its minimum at the time w_f attains its maximum. Furthermore, it is obvious that the redistribution proceeds as indicated by Figure 2.2, i.e. for every lateral position there exists one time $t_m \ge 0$, for which w_f attains its maximum.

In view of our numerical results we approximate the integrated form of the trapping mechanism (2.8) by a linear model, which predicts

$$w_t = \begin{cases} c_t \cdot (w_m - w_f) & \text{if } \dfrac{\partial \, w_f}{\partial \, t} < 0 \\[2mm] 0 & \text{if } \dfrac{\partial \, w_f}{\partial \, t} \ge 0 \end{cases} \tag{2.38}$$

at every lateral position where w_f is positive. The positive trapping constant c_t must be fitted. In Appendix 2B we vertically integrate an a priori linear trapping model under the assumptions that are used for the derivation

of (2.36). The trapping constant that results from this model is used to show that c_t is always smaller than $\dfrac{\rho_o}{\rho_w}$.

Writing the vertically integrated time derivative of equation (2.33) as

$$\frac{\partial w_o}{\partial t} = \begin{cases} \dfrac{\partial w_f}{\partial t} & \text{if } \dfrac{\partial w_f}{\partial t} \geq 0 \\[2ex] \dfrac{\partial w_f}{\partial t}\,(1 - c_t) & \text{if } \dfrac{\partial w_f}{\partial t} < 0, \end{cases} \tag{2.39}$$

we arrive at the nonlinear diffusion equation

$$F\left(\frac{\partial w_f}{\partial t}\right) = \gamma\,\frac{1}{r^{N-1}}\,\frac{\partial}{\partial r}\left(r^{N-1}\,w_f^q\,\frac{\partial w_f}{\partial r}\right) \quad \text{for } t > 0,\ 0 < r < r_l, \tag{2.40}$$

where

$$p = \frac{1}{1 - c_t}, \qquad p \geq 1 \tag{2.41}$$

$$\gamma = \frac{Z_c\,p\,\lambda_1\,\lambda_2}{R_c\,(n+1)} \tag{2.42}$$

$$q = \frac{3n - 2}{2\,(n+1)}, \qquad \frac{1}{4} < q < \frac{3}{2} \tag{2.43}$$

and F is defined for some function y by

$$F(y) = \begin{cases} p\,y & \text{if } y \geq 0 \\ y & \text{if } y < 0. \end{cases} \tag{2.44}$$

Because the 'diffusion' coefficient w_f^q of equation (2.40) vanishes when w_f reaches zero, the free boundary r_l, which separates the regions where $w_f > 0$ and $w_f = 0$, is at finite distance from the z-axis.

We impose the boundary and initial conditions corresponding to (2.11) and (2.13),

$$\frac{\partial w_f}{\partial r}\,(0, t) = 0 \quad \text{and} \quad w_f(r, 0) = w_i(r), \tag{2.45}$$

where $w_i = \phi \int S_i\,dz$ is the initial oil volume per unit lateral area. According to condition (2.14) w_i satisfies

$$\int_0^{r_l} r^{N-1}\,w_i\,(r)\,dr = 1. \tag{2.46}$$

2.3.3 The similarity solution

Equation (2.40) is the modified porous medium equation, that admits a similarity solution of the form [7, 29]

$$
w_{fa}(r, \bar{t}) = \begin{cases} \bar{t}^{-\mu} h(r\, \nu^{\frac{1}{2}}\, \bar{t}^{-\nu}) & \text{for } 0 \leq r < r_A \\ 0 & \text{for } r \geq r_A, \end{cases} \tag{2.47}
$$

where we have introduced $\bar{t} = \gamma \cdot (t - t_0)$ and t_0 represents the time at which the solution becomes singular. $r_A = A\,\nu^{-\frac{1}{2}}\,\bar{t}^{\nu}$, $A \in (0, \infty)$, represents the free boundary beyond which $w_{fa} = 0$. The function F in equation (2.40) gives rise to a second free boundary $r_B = B\,\nu^{-\frac{1}{2}}\,\bar{t}^{\nu}$, $B \in (0, A)$, which separates the regions with and without trapping.

Substitution of (2.47) into equation (2.40) shows that the similarity profile $h(\eta)$, with variable $\eta = r\,\nu^{\frac{1}{2}}\,\bar{t}^{-\nu}$, satisfies the nonlinear ordinary differential equation

$$
\eta^{1-N}\,(\eta^{N-1}\,h^q\,h')' = F(-\eta\,h' - k\,h) \quad \text{for } 0 < \eta < A \tag{2.48}
$$

(primes $'$ denote differentiation with respect to η), and that the positive constants μ and ν satisfy

$$
2\nu + q\mu - 1 = 0. \tag{2.49}
$$

Therefore, we have introduced the ratio $k = \dfrac{\mu}{\nu}$, which reflects the influence of trapping on the similarity profile. We obtain the boundary conditions

$$
h'(0) = 0, \quad h(A) = 0, \tag{2.50}
$$

whereas at $\eta = A$ an extra condition is valid [10, 19], i.e.

$$
h^{q-1} h'(A) = -p\,A. \tag{2.51}
$$

To simultaneously compute the similarity profile and the correct value of k, we scale h according to

$$
\tilde{h}(\xi) = A^{-\frac{2}{q}}\,h(A\,\xi), \quad \xi = \frac{\eta}{A}, \tag{2.52}
$$

see [45]. Hence, $\tilde{h}$ is the solution of equation (2.48) for $0 < \xi < 1$, for which the solution procedure is described in Appendix 2C. We obtain the trapping parameter k as a function of p, which is shown in Figure 2.3 for different q-values. Observe that for $p = 1$, k equals N and is independent of q.

The similarity solution $w_{fa}(r, \bar{t})$ does not generally satisfy the initial condition of (2.45) and its volume condition (2.46). However, if we can obtain
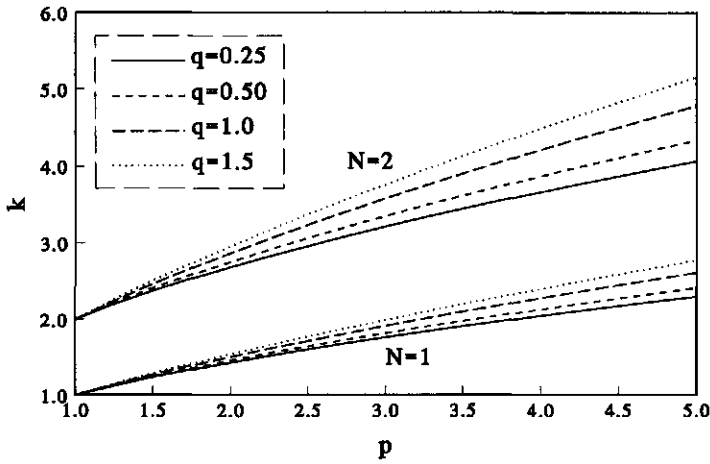
Figure 2.3: Parameter k as a function of p for several values of q (see (2.43)) and the lateral dimension N.

the appropriate values of A and t_0, the similarity solution provides a good approximation of the solution of equation (2.40) with its boundary and initial conditions after a sufficiently large time. Therefore, we define the 'moment' $m = \int r^{k-1} w_f \, dr$, which yields for the similarity solution in terms of $\tilde{h}(\xi)$ the time-independent expression

$$m_a = \nu^{-\frac{1}{2} k} A^{k+\frac{2}{q}} \int_0^1 \xi^{k-1} \tilde{h}(\xi) \, d\xi. \tag{2.53}$$

By comparison to the corresponding 'moment' of the general solution, we obtain the appropriate value of A independent of t_0. In case of entrapment, $p > 1$, the volume of free oil in the entire domain $v_f = \int r^{N-1} w_f \, dr$ is time-dependent and is given for the similarity solution by

$$v_{fa}(\bar{t}) = \bar{t}^{N\nu-\mu} \nu^{-\frac{1}{2} N} A^{N+\frac{2}{q}} \int_0^1 \xi^{N-1} \tilde{h}(\xi) \, d\xi. \tag{2.54}$$

In Appendix 2C we present explicit forms for the integral of relation (2.54). Comparison to the free oil volume of the general solution at a given time yields the value of t_0. Observe that in case of no entrapment, $p = 1$, the 'moment' (2.53) and the free oil volume (2.54) are equal. To obtain the value of t_0 we use another time-dependent characteristic, e.g. the value of w_f at the z-axis.

Determination of the trapped oil volume (2.38) from w_{fa} involves the maximum oil volume per unit lateral area. For small r the free oil volume decreases for all $\bar{t} > 0$, where the maximum oil volume is identical to the initial oil volume
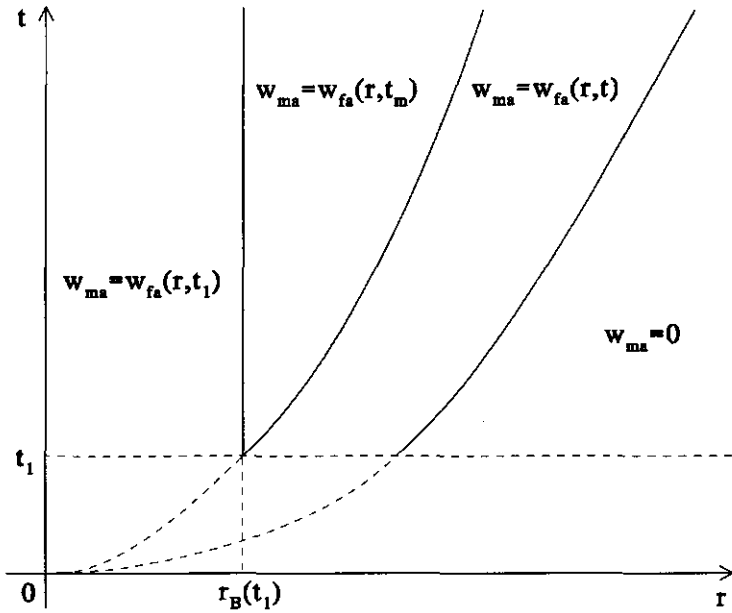
Figure 2.4: Different values of w_{ma} shown in the $r - \bar{t}$ plane.

per unit lateral area. Hence, taking the initial condition of (2.45), which generally does not have the similarity structure, as the maximum volume per unit lateral area yields a poor approximation of the trapped oil volume at later times. However, due to the linear nature of the trapping model (2.38) we may take w_{fa} at any positive time, say $\bar{t}_1$, as a new initial condition, from which w_{ta}, the oil volume per unit lateral area that becomes trapped for $\bar{t} > \bar{t}_1$, can be obtained. By definition $\dfrac{\partial w_{fa}}{\partial \bar{t}}$ changes sign for $r = r_B(\bar{t})$ and for $0 < r < r_B(\bar{t}_1)$ the maximum has been attained at $\bar{t} = \bar{t}_1$. For $\bar{t} > \bar{t}_1$ and $r > r_B(\bar{t}_1)$, we derive the maximum oil volume w_{ma} from the evolution of w_{fa}, which yields for every lateral position $r_B(\bar{t}_1) < r < r_B(\bar{t})$ the 'maximum' time $\bar{t}_m$, at which the free boundary r_B has passed. From the definition of r_B we find $\bar{t}_m = \left(\dfrac{r \nu^{\frac{1}{2}}}{B} \right)^{\frac{1}{\nu}}$. Consequently, we obtain for w_{ma} as shown in Figure 2.4

$$
w_{ma}(r,\bar{t}) = \begin{cases} w_{fa}(r,\bar{t}_1) & \text{if } 0 \leq r < r_B(\bar{t}_1) \\[2mm] w_{fa}\left(r, \left(\dfrac{r \nu^{\frac{1}{2}}}{B} \right)^{\frac{1}{\nu}} \right) & \text{if } r_B(\bar{t}_1) \leq r < r_B(\bar{t}) \\[2mm] w_{fa}(r,\bar{t}) & \text{if } r_B(\bar{t}) \leq r < r_A(\bar{t}) \\[1mm] 0 & \text{if } r \geq r_A(\bar{t}) \end{cases} \tag{2.55}
$$

and $w_{ta} = c_t \cdot (w_{ma} - w_{fa})$, which is assumed to be valid for $\bar{t} \geq \bar{t}_1$.

2.4 Applicability of the similarity solution to numerical simulations

2.4.1 Numerical results

To show the validity of the similarity solution we compare it with the numerical solutions of the model described in Section 2.2. In the numerical model, see also Section 4.3, equations (2.1), (2.2) and (2.3) are combined into the mixed form of the Richards equation [13, 36] for both water and oil. Computations were done in non-transformed physical variables. The flow domain was discretized by linear triangular finite elements of constant size in case of one lateral dimension and of increasing width for increasing R in case of two lateral dimensions. Time discretization was fully implicit. The resulting algebraic equations were solved by the modified Picard method [13], that gave good mass balances. Convergence was obtained for the Picard iterations by adjusting the time steps. The initial time step was 0.10 hours and the maximum allowable time step 50 hours. A typical computation time was 3 h on a HP 9000 735/125 workstation.

Some soil and fluid parameters were not varied:

$$
\begin{array}{llll}
K_{abs} & = 7.09 \cdot 10^{-12} \text{ m}^2, & \phi & = 0.400, \\
\mu_w & = 1.00 \cdot 10^{-3} \text{ Pa s}, & \rho_w & = 1.00 \cdot 10^3 \quad \text{kg m}^{-3}, \\
\mu_o & = 5.00 \cdot 10^{-4} \text{ Pa s}, & \rho_o & = 7.00 \cdot 10^2 \quad \text{kg m}^{-3}, \\
g & = 9.80 \qquad \text{m s}^{-2}.
\end{array}
$$

With respect to the reference case (case 1) we varied the parameters N, m, α_{ow}, β_{ow}, V_1 and S_{or}^{max} as summarized in Table 2.1. Additionally, the end of the computations T_e and the characteristic lengths and times are listed. Observe that in all computations condition (2.30) was satisfied.

We used a rectangular domain of height 3 m, discretized by 19 nodes. The lateral extension of the domain was chosen such that oil, which was initially only present at the leftmost part of the domain (a region close to the Z-axis), did not reach the right boundary during the simulations. The domain width (e.g. 75 m for the reference case) was divided into 1 m wide elements in case of one lateral dimension. At $T = 0$ h we imposed water and oil hydraulic heads, which for example in the reference case resulted in oil volumes of 0.3795 m^3 between $R = 0$ and $R = 1$ m, 0.2973 m^3 between $R = 1$ and $R = 2$ m, 0.2152 m^3 between $R = 2$ and $R = 3$ m, and 0.1076 m^3 between $R = 3$ and $R = 4$ m, and no oil elsewhere. We imposed no-flow conditions at every boundary, except at the right one, where the water pressure distribution

Table 2.1: Parameters and characteristic lengths and times that were used in the computations. Case 2 involved identical parameters but a different initial condition as case 1.

case	N	n	α_{ow}	β_{ow}	V_1	S_{or}^{max}	T_e	Z_c	R_c	T_c	t_{ve}
			m^{-1}		m^3		$10^3\,\mathrm{h}$	m	m	h	10^3
1	1	3.0	2.25	2.25	1.00	0.20	100	0.206	4.85	13.8	0.7
2*	1	3.0	2.25	2.25	1.00	0.20	100	0.206	4.85	13.8	0.8
3	1	3.0	2.25	2.25	1.00	0.00	100	0.206	4.85	13.8	1.4
4	1	3.0	2.25	2.25	1.00	0.10	100	0.206	4.85	13.8	1.0
5	1	3.0	2.25	2.25	1.00	0.40	100	0.206	4.85	13.8	0.4
6	1	3.0	2.25	2.25	1.00	0.60	120	0.206	4.85	13.8	0.3
7	1	2.0	2.25	2.25	1.00	0.20	68.0	0.206	4.85	13.8	0.7
8	1	4.0	2.25	2.25	1.00	0.20	120	0.206	4.85	13.8	1.4
9	1	5.0	2.25	2.25	1.00	0.20	120	0.206	4.85	13.8	2.6
10	1	3.0	4.50	2.25	1.00	0.20	150	0.103	9.69	27.7	2.9
11	1	3.0	9.00	2.25	1.00	0.20	180	0.0516	19.4	55.4	> 3.2
12	1	3.0	1.80	1.80	1.00	0.20	120	0.365	2.74	7.82	< 0.3
13	1	3.0	2.25	2.25	0.500	0.20	100	0.206	2.42	6.92	0.4
14	1	3.0	2.25	2.25	2.00	0.20	150	0.206	9.69	27.7	1.3
15	2	3.0	2.25	2.25	30.5	0.20	120	0.206	4.85	13.8	0.3
16	2	3.0	2.25	2.25	7.61	0.20	100	0.206	2.42	6.92	< 0.3

was kept hydrostatic with atmospheric pressure ($P_w = 0$) at 1 m above the bottom of the domain. To investigate the effect of an initially wider spread oil distribution, we imposed for case 2 0.1908 m^3 oil between $R = 0$ and $R = 3$ m, 0.1369 m^3 between $R = 3$ and $R = 4$ m, 0.0830 m^3 between $R = 4$ and $R = 7$ m, and 0.0415 m^3 between $R = 7$ and $R = 8$ m.

The total oil mass balance errors were small, varying from of 0.4 to 1.6 percent for computations in one lateral dimension and varying from 2.0 to 3.0 percent in two lateral dimensions. Test simulations showed that the errors decreased with smaller lateral grid distances, but did not uniformly decrease with smaller vertical grid distances. The largest part of the mass balance errors occurred shortly after the start of the simulations. During the rest of the simulation only at a few times convergence required significant decrease of time steps, which resulted in additional small mass balance errors. We observed that these times varied with a changing Z-grid.

Results are presented in dimensionless variables. The numerically obtained saturations were vertically integrated for comparison with the similarity solution. This leads to the free W_{fn}, trapped W_{tn} and maximum W_{mn} oil volumes per unit lateral area, where the subscript n identifies the numerical solution. The dimensionless w_{fn}, w_{tn} and w_{mn} follow after division by the characteristic
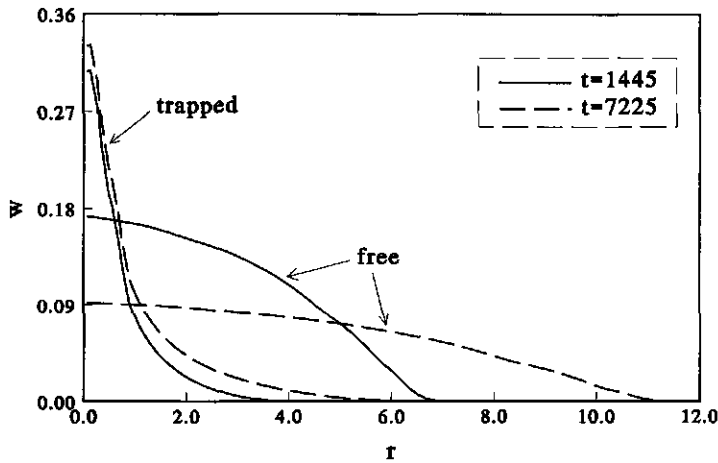
Figure 2.5: Free and trapped oil volumes per unit lateral area for case 1 at two times.

vertical length Z_c (2.31). In Figure 2.5 we show the vertically integrated oil saturations for the reference case at $t = 1445$ and $t = 7225$. Observe that before $t = 1445$ near the z-axis w_{fn} decreased rapidly from 1.84 to 0.172 leaving behind much trapped oil, whereas during all later times w_{fn} decreased slowly.

To show the effect of varying parameters on the amount of trapped oil, we computed for all cases $v_{tn} = \int r^{N-1} w_{tn} \, dr$ at $t = 3252$. In Figure 2.6 we present v_{tn} as a function of

$$\tilde{S}_{or}^{max} = \frac{S_{or}^{max}}{S_{or,r}^{max}}, \quad \tilde{n} = \frac{n}{n_r}, \quad \tilde{\alpha}_{ow} = \frac{\alpha_{ow}}{\alpha_{ow,r}}, \quad \tilde{V}_1 = \frac{V_1}{V_{1,r}}, \tag{2.56}$$

which represent the varied parameters of Table 2.1, that are normalized with respect to the parameters of the reference case (subscript r). For case 2 (different initial condition) we obtained $v_{tn} = 0.245$, for case 12 (values of α_{ow} and α_{ao} interchanged) we obtained $v_{tn} = 0.353$ and for cases 15 and 16 (two lateral dimensions) we obtained $v_{tn} = 0.403$ and $v_{tn} = 0.427$ respectively. Observe that the initial condition and volume have some effect on v_{tn}, but that v_{tn} is almost independent of α_{ow}. For small n the horizontal spreading was very fast, which resulted in a large v_{tn}. In two lateral dimensions the decrease of w_{fn} near the z-axis was faster, which leaded to larger values of v_{tn}.

We assessed when the lenses were at vertical flow equilibrium in view of condition (2.28). Hence, we list in Table 2.1 the times t_{ve} at which at the center of the lens (roughly) $z_{ao} = 1$, where $z_{ao}(0, t_{ve})$ is computed from relation (2.36). These times were small compared to the simulated times, except for the cases with small capillary forces (large n and α_{ow}).
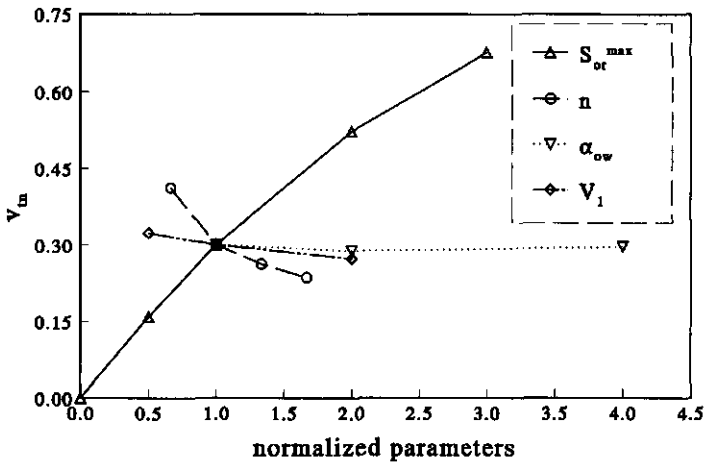
Figure 2.6: Volumes of trapped oil versus the normalized parameters. The S_{or}^{max}-curve reflects values of the parameters for cases 3-6, the n-curve for cases 7-9, the α_{ow}-curve for cases 10-11 and the V_1-curve for cases 13-14.

2.4.2 Agreement between the numerical solution and the similarity solution

To reveal the similarity behavior of the numerical solution at larger times and the corresponding trapping constant c_t we computed the 'moment' $m_n = \int r^{k-1} w_{fn} \, dr$ (2.53), rather than the ratio $w_{tn}/(w_{mn} - w_{fn})$, see (2.38), because the latter is too sensitive to local computation errors. We found that for every simulation a value of k exists for which after some time m_n becomes approximately time-independent. Except for case 11 (large α_{ow}) this happened in the first quarter of the simulated time. In Figure 2.7 we present for several cases of Table 2.1 m_n as a function of time. The corresponding values of k are given in Table 2.2. Notice that case 2 (different initial condition) leads to exactly the same value of k as case 1. We observed that m_n accurately recorded the reported mass balance errors. In some cases several significantly different values of k could be found that matched constant values of m_n on different time intervals. For example for case 5 we found that $k = 1.45$ perfectly matched a constant m_n for $900 < t < 3800$, but that $k = 1.56$ matched a constant m_n for $3800 < t < 7200$, where around $t = 3800$ convergence problems resulted in a mass balance error. In Appendix 2D we discuss how k can be estimated in practical situations and indicate that the solution is not very sensitive to changes in k.

With the obtained values of k we computed the scaled similarity profiles $\tilde{h}(\xi)$ and the appropriate values of p as described in Appendix 2C. With p we
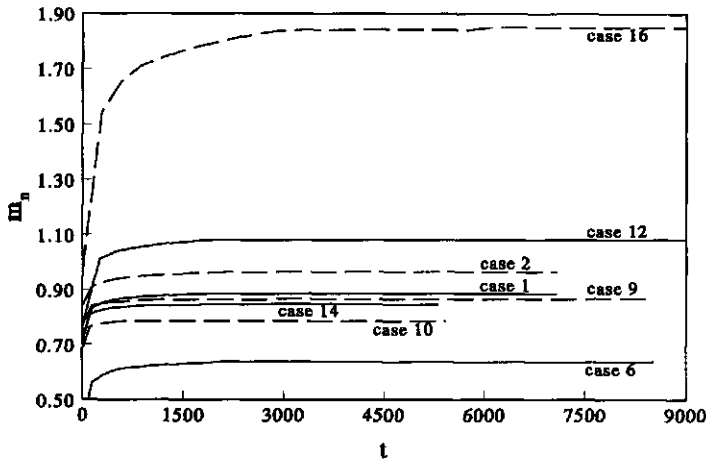
Figure 2.7: Evolution of the 'moment' of the numerical solution for several computations.

Table 2.2: Parameter values for the similarity solution and deviations of the numerical solution from the similarity solution.

case	k	c_t	γ	A	t_0	v_{ta}	e_t
1	1.24	0.316	0.0236	1.15	-437	0.0661	0.0795
2	1.24	0.316	0.0236	1.18	-501	0.0703	0.0712
3	1.00	0.0	0.0161	1.30	-517	-	-
4	1.12	0.185	0.0198	1.22	-782	0.0386	0.106
5	1.45	0.476	0.0308	1.02	-286	0.0816	0.143
6	1.73	0.611	0.0414	0.926	-167	0.0856	0.0340
7	1.32	0.395	0.0461	1.30	-286	0.0810	0.0601
8	1.18	0.245	0.0178	1.08	-544	0.0500	0.227
9	1.17	0.236	0.0164	1.04	-733	0.0467	0.146
10	1.17	0.245	0.00538	1.13	-478	0.0483	0.136
11	1.15	0.220	0.00129	1.11	-445	0.0407	0.161
12	1.32	0.385	0.159	1.18	-150	0.0836	0.113
13	1.32	0.385	0.0524	1.16	-652	0.0796	0.0490
14	1.21	0.286	0.0113	1.15	-512	0.0578	0.121
15	2.55	0.385	0.0262	1.15	-12	0.106	0.143
16	2.79	0.483	0.0623	1.18	216	0.126	0.0527
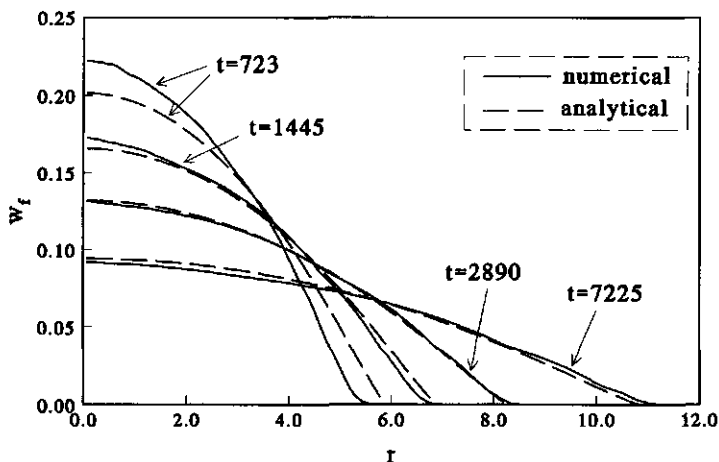
Figure 2.8: Numerical and analytical free oil volumes per unit lateral area for case 1 after fitting constants at $t = 1879$.

computed the values of c_t and γ, which are listed in Table 2.2. The variation of c_t is in accordance with the variations of v_{tn} of Figure 2.7, although c_t does decrease with increasing values of α_{ow}. To obtain the values of A and t_0, we set the numerical 'moment' and free oil volume m_n and v_{fn}, equal to their analytical equivalents m_a (2.53) and v_{fa} (2.54) at $t = t_e/4$. For case 3 (no entrapment) we obtained t_0 from comparison of $w_{fn}(0,t)$ and $w_{fa}(0,\bar{t}) = \bar{t}^{-\mu} h(0)$. The results are listed in Table 2.2 as well. Observe from the values of t_0 that the matched similarity profile for case 2 started earlier than for case 1, which reflects the wider spread initial condition of case 2.

The values of k, A and t_0 determine $w_{fa}(r,\bar{t})$. In Figure 2.8 we present w_{fn} and w_{fa} for case 1 at several times. Observe that for times larger than $t = 723$ the agreement is good. Taking $t_1 = t_e/4$ in relation (2.55) for the maximum oil volume, we computed at $t = t_e$ for case 1 w_{ma} and w_{ta} as shown in Figure 2.9. Here, $w_{ta}(r,t_e)$ represents the oil volume per unit lateral area that has become trapped after $t = t_e/4$. For comparison we showed also its numerical equivalent, i.e. the reduced $\bar{w}_{tn}(r,t_e) = w_{tn}(r,t_e) - w_{tn}(r,t_e/4)$. For all cases we quantified the difference between the analytical and the numerical solutions by the deviation

$$e_t = \frac{\bar{v}_{tn}(t_e) - v_{ta}(t_e)}{\bar{v}_{tn}(t_e)}, \qquad (2.57)$$

where $\bar{v}_{tn} = \int r^{N-1} \bar{w}_{tn} \, dr$ and $v_{ta} = \int r^{N-1} w_{ta} \, dr$. Observe that the latter is directly computed from relation (2.54) as

$$v_{ta}(t_e) = v_{fa}(t_e/4) - v_{fa}(t_e) = v_{fa}(t_e/4)(1 - 4^{N\nu-\mu}), \qquad (2.58)$$
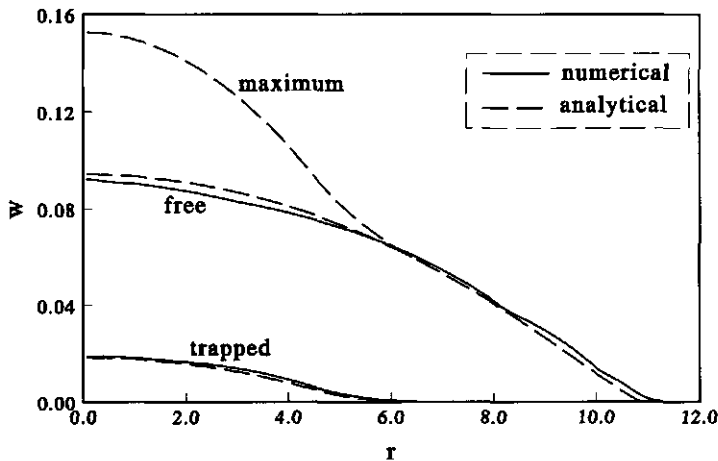
Figure 2.9: Numerical and analytical free and trapped oil volumes per unit lateral area for case 1 at $t = 7225$, where the maximum oil volume followed from the profile at $t = 1879$.

where $v_{fa}(t_e/4) = v_{fn}(t_e/4)$. We listed the values of e_t in Table 2.2. In most cases the agreement is good. Observe that for increasing S_{or}^{max} (cases 4, 1, 5, 6) the deviation decreases, except for case 5, which suffered from a numerical error as reported before. For increasing n (cases 7, 1, 8, 9) the deviation increased, except for case 8, which suffered from a similar numerical error. The deviations increased for decreasing capillarity (larger n and α_{ow}) and for increasing initial oil volumes, which is reasonable if we consider the increasing times at which the vertical equilibrium condition was met, see Table 2.1.

2.5   Conclusions

We investigated redistribution of a lens of organic contaminant with prescribed volume along the water table, with emphasis on the effect of entrapment of oil by water, in a two-dimensional planar or axisymmetric domain. For this three-phase flow process we presented the conditions for the vertical flow equilibrium assumption, for which gravity and capillary forces balance, in terms of of capillary forces, fluid densities and layer thickness. This assumption allowed vertical integration of the variables for oil, resulting into explicit approximate relations for the free oil volume per unit lateral area and the vertically averaged oil relative permeability in terms of the vertical position of the interface between zones with either two or three phases. The vertically integrated form of the nonlinear relation for the trapped oil saturation was approximated by a linear relation between the trapped oil volume per unit lateral area and the

difference of the maximum and the free oil volume per unit lateral area. The constant of linearity is not known a priori, but we showed that it is bounded from above by the oil-water density ratio.

The resulting single differential equation admitted a similarity solution for the free oil volume per unit lateral area as a function of time and the lateral space-coordinate, from which also the amount and location of trapped oil was obtained. The analytical solution is not explicit, but we showed a simple method to compute it from an ordinary differential equation.

Several numerical simulations, which were based on the nonreduced flow model with varying physical parameters, were carried out to test the validity of the similarity solution. We assessed when the lenses were at vertical equilibrium, which happened in an early stage of the simulations, except for situations with small capillary forces. In spite of numerical difficulties, we revealed the similarity behavior of the numerical solution and the corresponding constant of linearity in the approximate trapping model, using a time-independent 'moment' for the free oil distribution in the domain. As the similarity solution is initially not applicable, we fitted two parameters concerning the time scale and the mass of the solution shortly after the start of the simulations. From that time on the similarity solution provided a good approximation of the computed horizontal extension of the lens and the fraction of oil that became trapped.

Appendix 2A

Vertically integrated variables

The vertically integrated free oil saturation (2.34) is

$$w_f = \phi \int_{z_{ow}}^{z_u} (1 - S_{wa}) \, dz - \phi \int_{z_{ao}}^{z_u} (1 - S_t) \, dz \tag{2.59}$$

We use the first two terms of the Taylor series expansion for small values of $\left(\dfrac{\alpha_{ow} P_{ow}}{\rho_w g} \right)^n$ and $\left(\dfrac{\alpha_{ao} P_{ao}}{\rho_w g} \right)^n$ in relations (2.4) and (2.5) and use relations (2.18) and (2.19) to approximate

$$
\begin{aligned}
1 - S_{wa} &\sim \left(1 - \frac{1}{n} \right) \left(\frac{\alpha_{ow} P_{ow}}{\rho_w g} \right)^n = \\
&= \left(1 - \frac{1}{n} \right) \left((1 - D) \frac{\Delta \rho}{\rho_w} \right)^n (z - z_{ow})^n \\
1 - S_t &\sim \left(1 - \frac{1}{n} \right) \left(\frac{\alpha_{ao} P_{ao}}{\rho_w g} \right)^n =
\end{aligned}
\tag{2.60}
$$

$$= \left(1 - \frac{1}{n}\right) \left((1 - D) \frac{\alpha_{ao}\, \rho_o}{\alpha_{ow}\, \rho_w}\right)^n (z - z_{ao})^n, \qquad (2.61)$$

where we introduced dimensionless z, z_{ow} and z_{ao} according to (2.31). Using also layer thicknesses (2.27) we integrate (2.60) and (2.61) to approximate (2.59) as

$$w_f \sim \delta_1 \, z_{ao}^{n+1} \qquad (2.62)$$

where

$$\delta_1 = \phi \frac{n-1}{n(n+1)} \frac{\rho_w}{\Delta\,\rho}. \qquad (2.63)$$

The vertically integrated relative permeability (2.35) is

$$\bar{k} = \int_{z_{ow}}^{z_{ao}} (1 - S_{wa})^{\frac{1}{2}} \left(1 - S_{wa}^{\frac{n}{n-1}}\right)^{2 - \frac{2}{n}} dz +$$

$$+ \int_{z_{ao}}^{z_u} (S_t - S_{wa})^{\frac{1}{2}} \left(\left(1 - S_{wa}^{\frac{n}{n-1}}\right)^{1 - \frac{1}{n}} - \left(1 - S_t^{\frac{n}{n-1}}\right)^{1 - \frac{1}{n}}\right)^2 dz. \ (2.64)$$

We use again the Taylor series expansion to approximate

$$1 - S_{wa}^{\frac{n}{n-1}} \sim \left(\frac{\alpha_{ow}\, P_{ow}}{\rho_w\, g}\right)^n = \left((1 - D) \frac{\Delta\,\rho}{\rho_w}\right)^n (z - z_{ow})^n \qquad (2.65)$$

$$1 - S_t^{\frac{n}{n-1}} \sim \left(\frac{\alpha_{ao}\, P_{ao}}{\rho_w\, g}\right)^n = \left((1 - D) \frac{\alpha_{ao}\, \rho_o}{\alpha_{ow}\, \rho_w}\right)^n (z - z_{ao})^n. \quad (2.66)$$

Only the first integral of equation (2.64), denoted by $\bar{k}_1$, can be approximated analytically. With

$$z_{ao} - z_{ow} = \frac{\rho_w}{\Delta\,\rho} \, z_{ao}, \qquad (2.67)$$

derived from (2.27) we obtain

$$\bar{k}_1 = \delta_2 \, z_{ao}^{\frac{5n}{2} - 1}, \qquad (2.68)$$

where

$$\delta_2 = \frac{2}{5n - 2} \left(\frac{n-1}{n}\right)^{\frac{1}{2}} \frac{\rho_w}{\Delta\,\rho} (1 - D)^{\frac{5n}{2} - 2}. \qquad (2.69)$$

The second integral of equation (2.64), denoted by $\bar{k}_2$, is

$$\bar{k}_2 = I_k \, \delta_3 \, z_{ao}^{\frac{5n}{2} - 1}, \qquad (2.70)$$

where

$$\delta_3 = \left(\frac{n-1}{n}\right)^{\frac{1}{2}} \frac{\rho_w}{\Delta\,\rho} \frac{D}{1 - D} \qquad (2.71)$$

and the integral

$$I_k(n, D) = \int_0^1 \left((D\,y + 1 - D)^n - y^n \right)^{\frac{1}{2}} \left((D\,y + 1 - D)^{n-1} - y^{n-1} \right)^2 dy, \tag{2.72}$$

that does not depend on z_{ao} and must be approximated numerically.

As a result we obtain

$$z_{ao} = \lambda_1 \, w_f^{\frac{1}{n+1}} \tag{2.73}$$

$$\bar{k} = \lambda_2 \, w_f^{\frac{5n-2}{2(n+1)}}, \tag{2.74}$$

where

$$\lambda_1 = \delta_1^{\frac{-1}{n+1}} = \phi^{\frac{-1}{n+1}} \left(\frac{n(n+1)}{n-1} \right)^{\frac{1}{n+1}} \left(\frac{\Delta\rho}{\rho_w} \right)^{\frac{1}{n+1}} \tag{2.75}$$

$$\lambda_2 = (\delta_2 + I_k \, \delta_3) \, \delta_1^{\frac{2-5n}{2(n+1)}} =$$
$$= \phi^{\frac{2-5n}{2(n+1)}} \left(\frac{n-1}{n} \right)^{\frac{3-4n}{2(n+1)}} (n+1)^{\frac{5n-2}{2(n+1)}} \left(\frac{\Delta\rho}{\rho_w} \right)^{\frac{3n-4}{2(n+1)}} *$$
$$* \left(\frac{2}{5n-2} (1-D)^{\frac{5n}{2}-2} + \frac{D}{1-D} I_k \right). \tag{2.76}$$

Appendix 2B

An a priori linear trapping model

To obtain the upper bound for the trapping constant c_t in (2.38), we propose a priori a linear trapping model instead of the nonlinear model (2.8), i.e.

$$S_{ot}^{lin} = \begin{cases} \theta\,(S_{wa} - S_w^{min}) & \text{if } S_{wa} > S_w^{min} \\ 0 & \text{if } S_{wa} = S_w^{min}, \end{cases} \tag{2.77}$$

with constant $\theta \in [0,1]$, at locations where oil has been present. Assuming as in Appendix 2A that the oil lens thickness is small, we can vertically integrate (2.77), yielding

$$w_t^{lin} = \begin{cases} c_t^{lin}\,(w_m - w_f) & \text{if } \dfrac{\partial w_f}{\partial t} < 0 \\ 0 & \text{if } \dfrac{\partial w_f}{\partial t} \geq 0, \end{cases} \tag{2.78}$$

which we compare with (2.38).

To evaluate w_t^{lin} we introduce the additional elevations z_{ow}^{min}, z_{ao}^{max} and z_u^{max}, which determine the maximum oil and minimum water saturations. The trapped oil volume per unit lateral area is defined by

$$w_t = \phi \int_{z_{ow}^{min}}^{z_u^{max}} S_{ot} \, dz, \tag{2.79}$$

which yields for the linear model

$$
\begin{aligned}
w_t^{lin} &= \theta \phi \int_{z_{ow}^{min}}^{z_u^{max}} (S_{wa} - S_w^{min}) \, dz = \theta \left(\phi \int_{z_{ow}^{min}}^{z_u^{max}} (1 - S_w^{min}) \, dz + \right. \\
&- \left. \phi \int_{z_{ow}}^{z_u} (1 - S_{wa}) \, dz - \phi \int_{z_u}^{z_u^{max}} (1 - S_{wa}) \, dz \right).
\end{aligned}
\tag{2.80}
$$

Using (2.60) and (2.61) we obtain

$$\phi \int_{z_{ow}^{min}}^{z_u^{max}} (1 - S_w^{min}) \, dz - \phi \int_{z_{ow}}^{z_u} (1 - S_{wa}) \, dz \sim \frac{\delta_1}{1 - D} \left((z_{ao}^{max})^{n+1} - z_{ao}^{n+1} \right). \tag{2.81}$$

For $z_u < z < z_u^{max}$ S_{wa} is given by the third expression of (2.4), therefore we approximate

$$
\begin{aligned}
\phi \int_{z_u}^{z_u^{max}} (1 - S_{wa}) \, dz &\sim \phi \left(1 - \frac{1}{n}\right) \left(\frac{\alpha (1 - D)}{\alpha_{ow}} \right)^n \int_{z_u}^{z_u^{max}} z^n \, dz = \\
&= \phi \frac{n - 1}{n(n + 1)} \frac{\beta_{ow}}{1 - D} \left((z_{ao}^{max})^{n+1} - z_{ao}^{n+1} \right). \tag{2.82}
\end{aligned}
$$

Hence, we combine (2.81) and (2.82) to obtain

$$w_t^{lin} = \delta_1 \, \theta \, \frac{\rho_o}{\rho_w} \left((z_{ao}^{max})^{n+1} - z_{ao}^{n+1} \right), \tag{2.83}$$

which yields with the expression for w_f (2.62)

$$w_t^{lin} = \theta \, \frac{\rho_o}{\rho_w} (w_m - w_f) \tag{2.84}$$

and $c_t^{lin} = \theta \, \frac{\rho_o}{\rho_w}$.

We observe that according to the nonlinear model (2.8) everywhere in the domain $S_{ot} \geq 0$ and $S_{ot} \leq S_{wa} - S_w^{min} = S_{ot}^{lin}|_{\theta=1}$ for all $F_L \geq 0$. Hence, vertical integration yields

$$w_t \leq w_t^{lin}|_{\theta=1} = \frac{\rho_o}{\rho_w} (w_m - w_f) \tag{2.85}$$

and we obtain $c_t \leq \frac{\rho_o}{\rho_w}$.

Appendix 2C

Evaluation of the ordinary differential equation

For the scaled variable $\tilde{h}(\xi)$ we solve the nonlinear differential equation

$$\xi^{1-N} (\xi^{N-1} \tilde{h}^q \tilde{h}')' = F(-\xi \tilde{h}' - k \tilde{h}) \quad \text{for } 0 < \xi < 1 \qquad (2.86)$$

with boundary conditions

$$\tilde{h}'(0) = 0, \quad \tilde{h}(1) = 0. \qquad (2.87)$$

In the no-trapping case $p = 1$, k equals N and the solution is explicitly given by

$$\tilde{h}(\xi) = \left(\frac{q}{2} (1 - \xi^2) \right)^{\frac{1}{q}}, \qquad (2.88)$$

which is called the Barenblatt-Pattle point source solution [5, 50], that was applied to oil lens spreading in [10].

In case $p > 1$, k is a strictly increasing function of p [29], see Figure 2.3, and $\tilde{h}$ is not explicitly known. The extra boundary condition (2.51) has transformed into

$$\tilde{h}^{q-1} \tilde{h}'(1) = -p. \qquad (2.89)$$

We transform equation (2.86) into a system of two first order ordinary differential equations, with

$$y_1 = \frac{\tilde{h}^q}{q} \quad \text{and} \quad y_2 = \tilde{h}^{q-1} \tilde{h}' \qquad (2.90)$$

(primes $'$ denote differentiation with respect to ξ). Hence, we solve

$$\begin{cases} y_1' &= y_2 \\ y_2' &= -\dfrac{N-1}{\xi} y_2 - \dfrac{y_2^2}{q\, y_1} + F\left(-\xi \dfrac{y_2}{q\, y_1} - k \right) \end{cases} \qquad (2.91)$$

for $\xi \in (0, 1)$, with boundary conditions

$$y_2(0) = 0, \quad y_1(1) = 0 \quad \text{and} \quad y_2(1) = -p.$$

System (2.91) is solved by shooting backward from $\xi = 1$ using a fourth order Runge-Kutta scheme. As $y_2(0)$ is a monotone function of k we can use a simple iteration to vary k until the solution satisfies $y_2(0) = 0$. Inversely, if we know the value of k, we can use a similar iteration to obtain $\tilde{h}$ and the value of p.

We evaluate the integral of relation (2.54). For $p = 1$, we use expression (2.88) to obtain

$$\int_0^1 \xi^{N-1}\,\tilde{h}(\xi)\,d\xi = \begin{cases} \dfrac{\sqrt{\pi}\,\Gamma(1+\frac{1}{q})}{2\,\Gamma(\frac{3}{2}+\frac{1}{q})}\left(\dfrac{q}{2}\right)^{\frac{1}{q}} & \text{for } N = 1 \\[3ex] \dfrac{1}{q+2}\left(\dfrac{q}{2}\right)^{1+\frac{1}{q}} & \text{for } N = 2, \end{cases} \tag{2.92}$$

where Γ denotes the gamma-function. For $p > 1$, we set $\tilde{B} = \dfrac{B}{A}$ and integrate equation (2.48) from 0 to $\tilde{B}$ and from $\tilde{B}$ to 1 subsequently. Because F vanishes at $\xi = \tilde{B}$, we find

$$-\tilde{B}\,\tilde{h}'(B) - k\,\tilde{h}(\tilde{B}) = 0. \tag{2.93}$$

We obtain

$$\int_0^1 \xi^{N-1}\,\tilde{h}(\xi)\,d\xi = \left(1 - \frac{1}{p}\right)\frac{k}{k-N}\,\tilde{B}^{N-2}\,\tilde{h}^{q+1}(\tilde{B}). \tag{2.94}$$

Appendix 2D

Parameter estimation for the similarity solution

Prediction of the behavior of an oil lens requires estimation of the parameters c_t, A and t_0. To achieve this, measurements of free oil per unit lateral area w_f at two times (t_1, t_2) are necessary. We use $w_1 = w_f(0, t_1)$, $w_2 = w_f(0, t_2)$ and the free oil volume in the domain $v_1 = v_f(t_1)$, $v_2 = v_f(t_2)$. Defining $w = w_1/w_2$ and $v = v_1/v_2$ we identify according to the similarity solution (2.47) and (2.54)

$$w = \bar{t}^{-\mu} \quad \text{and} \quad v = \bar{t}^{\frac{N}{2}-\mu\left(\frac{qN}{2}+1\right)}, \tag{2.95}$$

which yields the estimated value of μ and as a result the values of ν and k. With k we compute the scaled similarity solution $\tilde{h}$ and the values of p and c_t. Furthermore, we obtain the values of A and t_0 from the moment $m(t_2) = \int r^{k-1}\,w_f(r, t_2)\,dr$ and v_2 by comparison with the analytically obtained moment (2.53) and volume (2.54).

The sensitivity of the results to measured data is illustrated using numerical data of case 1 in Table 2.1. In Table 2.3 we show data for four different times (t_a, t_b, t_c and t_d respectively). Using t_a and t_b we computed $w_{fa}(r, t_d)$, which is referred to in Figure 2.10 as fit 1. This fit yielded $k = 1.193$, $c_t = 0.2657$, $A = 1.153$ and $t_0 = -367.9$, with $w_{fa}(0, t_d) = 0.09712$ and $v_{fa}(t_d) = 0.6838$. Using t_b and t_c we computed $w_{fa}(r, t_d)$, which is referred to as fit 2. This fit yielded $k = 1.215$, $c_t = 0.2887$, $A = 1.149$ and $t_0 = -618.7$,

Table 2.3: Data of case 1 for illustration of measurement sensitivity.

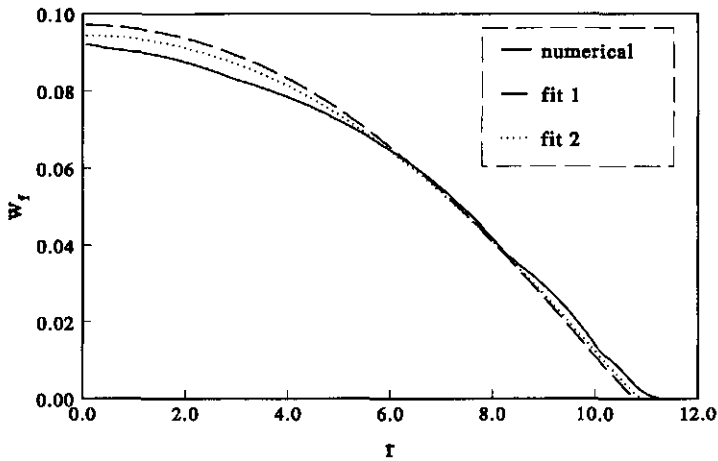| t	$w_f(0,t)$	$v(t)$
722.5	0.2220	0.7790
1445	0.1725	0.7478
2890	0.1314	0.7127
7225	0.09205	0.6575

Figure 2.10: Computed free oil volume per unit lateral area compared with predictions from data at $t = 722.5$ and $t = 1445$ (fit 1) and from data at $t = 1445$ and $t = 2890$ (fit 2).

with $w_{fa}(0, t_d) = 0.09446$ and $v_{fa}(t_d) = 0.6730$. These fits indicate that a significant difference of the estimated values of c_t does not lead to large deviations of the predicted results.

Notation

A	position of oil free boundary in similarity profile
B	position of trapped oil free boundary in similarity profile
c_t	trapping constant
D	parameter determining finiteness of lens thickness
e_t	deviation between analytical and numerical solution
F	trapping function
F_L	Land's factor
f_o	oil fractional flow function
g	gravity [$\mathrm{m\,s^{-2}}$]
$h\,(\tilde{h})$	(scaled) similarity profile
K	absolute permeability [$\mathrm{m^2}$]
k	trapping parameter in similarity profile
k_{rj}	phase j relative permeability
$\bar{k}$	vertically integrated oil relative permeability
m	dimensionless moment of free oil saturation per unit lateral area
N	number of lateral dimensions
n	van Genuchten parameter
p	trapping constant in function F
P_j	phase j pressure [Pa]
P_{jk}	phases j, k capillary pressure [Pa]
q	power in coefficient of diffusion equation
$R\,(r)$	(dimensionless) horizontal coordinate [m]
R_c	characteristic horizontal length [m]
$R_l\,(r_l)$	(dimensionless) horizontal position of lens outer boundary [m]
r_A	position of oil free boundary for similarity solution
r_B	position of trapped oil free boundary for similarity solution
S_i	initial oil saturation
S_j	phase j saturation
S_{of}	free oil saturation
S_{ot}	trapped oil saturation
S_{or}^{max}	maximum residual oil saturation
S_t	total fluid saturation
S_{wa}	apparent water saturation
S_w^{min}	minimum water saturation

$T\left(t\right)$ (dimensionless) time [h]

T_c characteristic time [h]

$T_e\left(t_e\right)$ (dimensionless) maximum computed time [h]

t_0 starting time of similarity solution

$\bar{t}$ time in similarity solution

U_j phase j horizontal flow velocity $[\text{m s}^{-1}]$

U_t total horizontal flow velocity $[\text{m s}^{-1}]$

V_j phase j vertical flow velocity $[\text{m s}^{-1}]$

V_t total vertical flow velocity $[\text{m s}^{-1}]$

V_1 initial oil volume $[\text{m}^3]$

v_f dimensionless free oil volume

v_t dimensionless trapped oil volume

$W_f\left(w_f\right)$ (dimensionless) free oil volume per unit lateral area [m]

w_i dimensionless initial oil volume per unit lateral area

$W_m\left(w_m\right)$ (dimensionless) maximum oil volume per unit lateral area [m]

$W_t\left(w_t\right)$ (dimensionless) trapped oil volume per unit lateral area [m]

$Z\left(z\right)$ (dimensionless) vertical coordinate [m]

Z_c characteristic vertical length [m]

$Z_{ao}\left(z_{ao}\right)$ (dimensionless) elevation beyond which air is present [m]

$Z_{ow}\left(z_{ow}\right)$ (dimensionless) elevation beyond which oil is present [m]

$Z_u\left(z_u\right)$ (dimensionless) elevation beyond which no oil is present [m]

α van Genuchten parameter $[\text{m}^{-1}]$

β_{ao}, β_{ow} ratios of air-oil and oil-water to air-water surface tensions

γ dimensionless parameter in nonlinear diffusion equation

$\eta\left(\xi\right)$ (scaled) similarity variable

λ_1, λ_2 constants in power law approximations of z_{ao} and $\bar{k}$

μ, ν powers in similarity solution

μ_j phase j viscosity $[\text{Pa s}]$

ρ_j phase j density $[\text{kg m}^{-3}]$

ϕ porosity

Chapter 3

Analysis of oil lens removal by extraction through a seepage face

3.1 Introduction

Spills of hydrocarbons have caused contamination of numerous aquifers. Non-aqeous phase liquids, such as gasoline, that are less dense than water (henceforth called oil for brevity), may accumulate as a lens at the phreatic water surface. To remediate the contaminated aquifers, the bulk of oil in the lens is usually first removed by pump and treat methods, after which the remaining (trapped) oil is removed by other techniques, such as air sparging or bioremediation.

Pumping is commonly done through vertically drilled extraction filters or in horizontal ditches in case of shallow lenses. If the extraction well or ditch is partially filled with fluid, two fluid phases may seep out of the soil above the well fluid level, similar to water seepage in the dam problem [9, 18]. Multiphase seepage is a complicated process, since the non-wetting phase may seep out at virtually zero saturations [3, 64].

During pumping often a drawdown of the water table is created to facilitate oil flow towards the extraction well. Such a local lowering of the water table may smear out the oil and increase both the oil-invaded region and the amount of trapped oil. For this reason the drawdown of the water table is preferably kept small. If the slope of the water table is small, the lens may be at vertical flow equilibrium, except close to the pumping well or ditch. At vertical equilibrium pressure distributions are hydrostatic and therefore the vertical dimension of the multi-phase flow problem can be eliminated by vertical integration of variables. In that situation only the oil flow equation needs to be considered, see [10, 45, 49] and Section 2.3.1.

Corapcioglu e.a. [16] modeled an axisymmetric two-pump recovery system, in which the lower well was assumed to create a drawdown of the water table and the upper well was assumed to extract free oil at a constant rate. They

53

used a sharp-interface approach and assumed that the well was located within the oil lens at any time, which may only be realistic during the early stages of pumping when the oil layer is relatively thick. After linearizing equations analytical solutions were obtained.

Huyakorn e.a. and Wu e.a. [31, 63] numerically investigated withdrawal of an oil lens in a three-dimensional domain assuming vertical flow equilibrium. In [31] withdrawal wells were assumed to operate under prescribed volumetric extraction rates, where the separate water and oil extraction rates were determined by the phase mobilities. In [63] the well bore pressure and the productivity index for a local grid block were computed as in the oil reservoir engineering literature, see e.g. [21], to determine the separate water and oil extraction rates. Both studies were restricted to the part of the oil lens where only water and oil were present, thus neglecting the three-phase zone.

Wu e.a. [64] discussed numerical implementation of seepage boundary conditions, also for three-phase flow. Although at seepage boundaries the well pressure is known, they imposed sink terms for water and oil similar to the well conditions of [63] with a large artificial productivity index.

In this study we present a model for the behavior of an oil lens on the water table in a two-dimensional domain for two lens geometries, where withdrawal occurs through a well with constant fluid level. To treat the corresponding multi-phase seepage face conditions, we impose the so called Signorini conditions. Numerically, we compared implementation of these conditions as sink terms according to [64] to a more direct implementation. For the situation in which the well fluid level is equal to the phreatic water surface in the soil, we perform several numerical computations and give an indication of their accuracy, especially near the seepage boundary.

As numerical models still require large computation times and are not always able to handle the boundary conditions accurately, approximate analytical solutions can be very helpful. We use the vertical equilibrium assumption of capillarity-gravity-segregated flow to reduce the multi-phase flow problem to a single equation for oil flow. In the vertically integrated problem for the layer thickness we approximate the well boundary condition by taking lens thickness equal to zero. Similar problems for water outflow from an aquifer, with sharp interfaces, were studied by Boussinesq [9] and by Barenblatt [7] who derived analytical solutions. We use the generalizations of these analytical solutions that account for capillary forces, to describe oil lens extraction with possible incorporation of oil entrapment by water. In Appendix 3B we show that a similar analytical solution can be obtained for oil removal in a semi-infinite three-dimensional domain.

The analytical solutions are compared with the numerical results. We

indicate in which cases the analytical solutions with the approximate well condition appropriately approximate the solutions of the non-reduced flow model.

3.2   Model

We model withdrawal of an oil lens in a two-dimensional domain $0 < X < L$, $-\infty < Z < \infty$, with $L > 0$, and a well at $X = 0$. Two important situations that are different with respect to the horizontal extension of the domain, are considered. The first concerns a horizontally bounded domain as shown in Figure 3.1.a, i.e. $L < \infty$, which reflects either the left half of a symmetric domain with a second well at $X = 2L$ or a situation with a vertical impervious boundary at $X = L$. The second concerns a domain, that is unbounded to the right, as shown in Figure 3.1.b, i.e. $L = \infty$, where the oil lens is bounded by $X = X_l$ and can spread out in horizontal direction. We use for both water (w) and oil (o) the mass balance equations

$$\phi \frac{\partial S_j}{\partial T} + \frac{\partial U_j}{\partial X} + \frac{\partial V_j}{\partial Z} = 0, \quad j = w, o \tag{3.1}$$

and Darcy's Law

$$U_j = -\frac{K k_{rj}}{\mu_j} \frac{\partial P_j}{\partial X} \tag{3.2}$$

$$V_j = -\frac{K k_{rj}}{\mu_j} \left(\frac{\partial P_j}{\partial Z} + \rho_j g \right), \quad j = w, o, \tag{3.3}$$

where T is time, X and Z are the horizontal and vertical coordinates respectively, S_j is effective phase saturation, U_j and V_j are phase horizontal and vertical flow velocities respectively, P_j is phase pressure, ρ_j phase density, k_{rj} phase relative permeability, μ_j phase viscosity, ϕ porosity, K absolute permeability and g gravitation. We assume that the soil is homogeneous and isotropic, that both fluids are incompressible and that air is present with saturation S_a and constant pressure ($P_a = 0$). According to [48] we define the total fluid saturation S_t, trapped oil saturation S_{ot}, free oil saturation S_{of}, apparent water saturation S_{wa}, oil-water capillary pressure P_{ow} and air-oil capillary pressure P_{ao}, which satisfy the constitutive relations

$$\begin{aligned} S_w + S_o &= S_t \\ S_t + S_a &= 1 \\ S_w + S_{ot} &= S_{wa} \\ S_{of} + S_{ot} &= S_o \end{aligned}$$
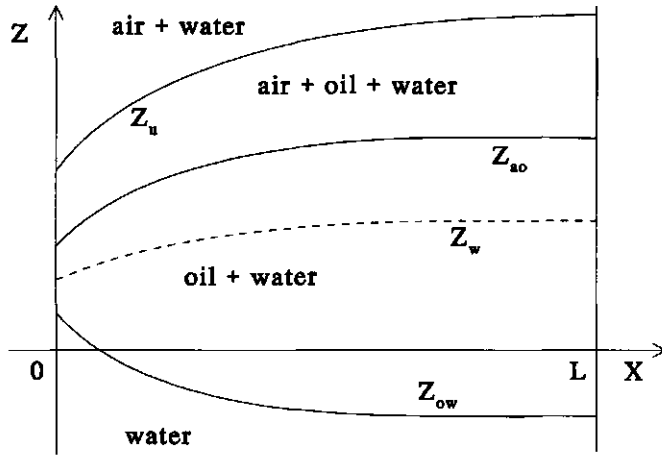
(a)
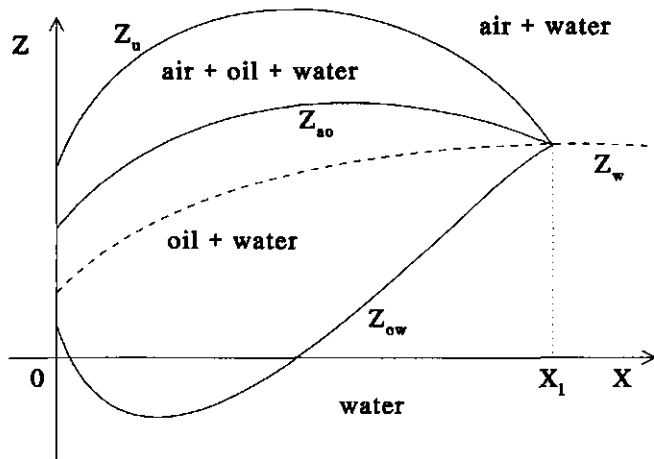
(b)

Figure 3.1: Geometry of an oil lens in a domain that is bounded to the right (a) and that is unbounded to the right (b).

$$P_{ow} = P_o - P_w$$
$$P_{ao} = -P_o.$$

For the retention functions we use

$$
S_{wa} = \begin{cases}
1 & \text{if } P_w > 0 \text{ and } P_o < P_w \\
\left(1 + \left(\dfrac{\alpha_{ow}}{\rho_w\, g} P_{ow}\right)^n\right)^{\frac{1}{n}-1} & \text{if } \begin{cases} 0 < P_w < P_o \text{ or} \\ P_w < 0 \text{ and } P_o > \dfrac{1}{\beta_{ao}} P_w \end{cases} \\
\left(1 + \left(\dfrac{-\alpha}{\rho_w\, g} P_w\right)^n\right)^{\frac{1}{n}-1} & \text{if } P_o < \dfrac{1}{\beta_{ao}} P_w < 0
\end{cases}
\tag{3.4}
$$

$$
S_t = \begin{cases}
1 & \text{if } P_o > 0 \text{ or } P_w > 0 \\
\left(1 + \left(\dfrac{\alpha_{ao}}{\rho_w\, g} P_{ao}\right)^n\right)^{\frac{1}{n}-1} & \text{if } \dfrac{1}{\beta_{ao}} P_w < P_o < 0 \\
S_{wa} & \text{if } P_o < \dfrac{1}{\beta_{ao}} P_w < 0,
\end{cases}
\tag{3.5}
$$

where $\alpha > 0$ and $n > 1$ are soil parameters. Furthermore, $\alpha_{ow} = \alpha \beta_{ow}$ and $\alpha_{ao} = \alpha \beta_{ao}$, where β_{ow} and β_{ao} are the ratios of the oil-water and the air-oil to the air-water surface tensions, with $\dfrac{1}{\beta_{ow}} + \dfrac{1}{\beta_{ao}} = 1$. Relative permeabilities satisfy [38]

$$
k_{rw} = S_w^{\frac{1}{2}} \left(1 - \left(1 - S_w^{\frac{n}{n-1}}\right)^{1-\frac{1}{n}}\right)^2
\tag{3.6}
$$

$$
k_{ro} = (S_t - S_{wa})^{\frac{1}{2}} \left(\left(1 - S_{wa}^{\frac{n}{n-1}}\right)^{1-\frac{1}{n}} - \left(1 - S_t^{\frac{n}{n-1}}\right)^{1-\frac{1}{n}}\right)^2.
\tag{3.7}
$$

Motivated by the results of Chapter 2 we model oil entrapment by a linear relation, i.e.

$$
S_{ot} = \begin{cases}
\theta \left(S_{wa} - S_w^{min}\right) & \text{if } S_{wa} > S_w^{min} \\
0 & \text{if } S_{wa} = S_w^{min},
\end{cases}
\tag{3.8}
$$

where the minimum water saturation S_w^{min} is given by

$$
S_w^{min}(X, Z, T) = \min_{T' \le T} S_w(X, Z, T').
\tag{3.9}
$$

The constant $\theta \in [0, 1]$ is the maximum trapped oil saturation, which is obtained when $S_w^{min} = 0$ and $S_{wa} = 1$.

Equations (3.1), (3.2) and (3.3) are solved for time $T > 0$ in the domain of Figure 3.1. The free oil is confined to two layers [49]. Between the levels

$Z = Z_u$ and $Z = Z_{ao}$ water, (free) oil and air are present, whereas between the levels $Z = Z_{ao}$ and $Z = Z_{ow}$ only water and (free) oil are present. At the level $Z = Z_w$ we have $P_w = 0$, which corresponds outside the oil lens to the phreatic surface. For $L = \infty$ the levels Z_u, Z_{ao} and Z_{ow} coincide for $X = X_l$ at $Z = Z_w$. Hence, $Z_{ow}(X,T)$, $Z_{ao}(X,T)$, $Z_u(X,T)$ are defined by

$$
\begin{aligned}
S_t &= 1, & S_{of} &= 0 & &\text{if } Z < Z_{ow} \\
S_t &= 1, & S_{of} &> 0 & &\text{if } Z_{ow} < Z < Z_{ao} \\
S_t &< 1, & S_{of} &> 0 & &\text{if } Z_{ao} < Z < Z_u \\
S_t &< 1, & S_{of} &= 0 & &\text{if } Z > Z_u,
\end{aligned}
$$

In terms of capillary pressures these levels are given by

$$
P_{ow}\left(Z_{ow}\right) = 0, \quad P_{ao}\left(Z_{ao}\right) = 0, \quad \frac{\beta_{ao}}{\beta_{ow}}\, P_{ao}\left(Z_u\right) = P_{ow}\left(Z_u\right). \tag{3.10}
$$

In the well at the left side of the boundary $X = 0$ the fluid level is fixed at $Z = 0$. We impose well conditions, which may include seepage of oil at the entire boundary $X = 0$ and seepage of water for $Z > 0$. At seepage boundaries a certain phase can only flow out, in which case its pressure is equal to the pressure outside the porous medium [14, 18]. Hence, similar to water seepage in the dam problem [9, 18], we impose the Signorini conditions [4, 24] for multi-phase seepage

$$
\begin{aligned}
P_w &\le P_{out}, & U_w &\le 0, & \left(P_w - P_{out}\right) U_w &= 0 & &\text{for } X = 0,\ Z > 0 \\
P_o &\le P_{out}, & U_o &\le 0, & \left(P_o - P_{out}\right) U_o &= 0 & &\text{for } X = 0,\ -\infty < Z < \infty,
\end{aligned}
\tag{3.11}
$$

and also

$$
P_w = P_{out} \qquad \text{for } X = 0,\ Z \le 0, \tag{3.12}
$$

where

$$
P_{out}\left(Z\right) = \begin{cases} 0 & \text{for } Z > 0 \\ -\rho_w\, g\, Z & \text{for } Z \le 0. \end{cases} \tag{3.13}
$$

For $L < \infty$ we impose additionally no-flow conditions at $X = L$, i.e. $U_j = 0$ for $j = w, o$.

At $T = 0$ we take initial pressure distributions

$$
\left.
\begin{aligned}
P_w\left(X, Z, 0\right) &= P_{w,i}\left(X, Z\right) \\
P_o\left(X, Z, 0\right) &= P_{o,i}\left(X, Z\right)
\end{aligned}
\right\} \quad \text{for } 0 < X < L,\ -\infty < Z < \infty, \tag{3.14}
$$

such that oil has nonzero saturation $S_{o,i}$ in a lens with the finite horizontal extension $X_l \le L$, which has prescribed volume

$$
\mathcal{V}_0 = \phi \int_{-\infty}^{\infty} \int_0^{\infty} S_{o,i}\, dX\, dZ = \phi \int_{Z_{ow}}^{Z_u} \int_0^{X_l} \left(S_t(P_{o,i}) - S_{wa}(P_{w,i}, P_{o,i})\right)\, dX\, dZ. \tag{3.15}
$$

If $L < \infty$ we identify $X_l \equiv L$. At $T = 0$ no oil is trapped.

We define characteristic horizontal length-scales according to

$$X_c = \begin{cases} L & \text{for } L < \infty \\ \alpha_{ow} \, \mathcal{V}_0 & \text{for } L = \infty \end{cases} \tag{3.16}$$

and a characteristic vertical length-scale, velocity, pressure and time according to

$$Z_c = \frac{1}{\alpha_{ow}}, \quad U_c = \frac{K \rho_o g}{\mu_o}, \quad P_c = \frac{\rho_o g}{\alpha_{ow}}, \quad T_c = \frac{X_c}{U_c} \tag{3.17}$$

This leads to the dimensionless variables

$$u_j = \frac{U_j}{U_c}, \; v_j = \frac{V_j}{U_c}, \; p_j = \frac{P_j}{P_c}, \; x = \frac{X}{X_c}, \; z = \frac{Z}{Z_c}, \; t = \frac{T}{T_c}, \; j = w, o. \tag{3.18}$$

Similarly, P_{out}, $P_{w,i}$, $P_{o,i}$, X_l, Z_w, Z_{ow}, Z_{ao} and Z_u become dimensionless by scaling with P_c, X_c and Z_c.

Combining equations (3.1), (3.2) and (3.3) into two Richards equations the resulting problem is ($j = w, o$)

$$\phi \frac{\partial S_j}{\partial t} - \frac{\mu_o}{\mu_j} \left(\frac{Z_c}{X_c} \frac{\partial}{\partial x} \left(k_{rj} \frac{\partial p_j}{\partial x} \right) + \frac{X_c}{Z_c} \frac{\partial}{\partial z} \left(k_{rj} \left(\frac{\partial p_j}{\partial z} + \frac{\rho_j}{\rho_o} \right) \right) \right) = 0 \tag{3.19}$$

for $x > 0$, $-\infty < z < \infty$, $t > 0$. The boundary conditions become

$$p_j \leq 0, \quad u_j \leq 0, \quad p_j \, u_j = 0 \qquad\qquad \text{for } x = 0, \; z > 0$$

$$\left. \begin{aligned} p_w &= -\frac{\rho_w}{\rho_o} z \\ p_o &\leq -\frac{\rho_w}{\rho_o} z, \; u_o \leq 0, \; \left(p_o + \frac{\rho_w}{\rho_o} z \right) u_o = 0 \end{aligned} \right\} \quad \text{for } x = 0, \; z \leq 0 \tag{3.20}$$

and additionally for the bounded domain $u_j = 0$ for $x = 1$, $-\infty < z < \infty$. The initial conditions are

$$\left. \begin{aligned} p_w (x, z, 0) &= p_{w,i}(x, z) \\ p_o (x, z, 0) &= p_{o,i}(x, z) \end{aligned} \right\} \quad \text{for } x > 0, \; -\infty < z < \infty, \tag{3.21}$$

with

$$\phi \int_{z_{ow}}^{z_u} \int_0^{x_l} (S_t(p_{o,i}) - S_{wa}(p_{w,i}, p_{o,i})) \, dx \, dz = v_0, \tag{3.22}$$

where $v_0 = \frac{\mathcal{V}_0}{X_c \, Z_c}$.

3.3   Numerical results

3.3.1   Numerical model

We simulated the withdrawal of an oil lens with our numerical model, see also Sections 2.4.1 and 4.3, which we adapted for the seepage face boundary conditions. In this model equations (3.1), (3.2) and (3.3) are combined into the mixed form of the Richards equation [13, 36] for both water and oil. Computations were done in non-transformed physical variables. The flow domain was discretized by linear triangular finite elements. Time discretization was fully implicit. The resulting algebraic equations were solved by the modified Picard method [13], that gave good mass balances. Convergence was obtained for the Picard iterations by adjusting the time steps. The initial time step was 0.10 hours and the maximum allowable time step 50 hours.

Some soil and fluid parameters were not varied:

$$
\begin{aligned}
K_{abs} &= 7.09 \cdot 10^{-12}\ \mathrm{m}^2, & \phi &= 0.400, \\
\mu_w &= 1.00 \cdot 10^{-3}\ \mathrm{Pa\,s}, & \rho_w &= 1.00 \cdot 10^3 & \mathrm{kg\,m}^{-3}, \\
\mu_o &= 5.00 \cdot 10^{-4}\ \mathrm{Pa\,s}, & g &= 9.80 & \mathrm{m\,s}^{-2}.
\end{aligned}
$$

We varied the parameters L, $\mathcal{V}_0$, n, α, β_{ow}, ρ_o and θ as summarized in Table 3.1. Additionally, the maximum computed times T_e and the characteristic lengths and times are listed.

3.3.2   Treatment of seepage face conditions

Condition (3.11) requires that at nodes of the seepage boundary either a velocity (no-flow) or a pressure is prescribed. We compare two approaches to dealing with this condition numerically.

In an attempt to model all types of boundary conditions by source / sink terms, it has been proposed [64] to treat this variational condition by imposing at every phase j seepage node the sink term (in physical dimensions)

$$
U_j = -\chi \frac{K\,k_{rj}}{\mu_j}\ \max\left(0, P_j - P_{out}\right), \tag{3.23}
$$

where χ is a large number. In this condition the pressure gradient of the horizontal flow velocity (3.2) is replaced by the product $\chi \cdot (P_j - P_{out})$ and consequently a large value of χ represents a fine mesh in the X-direction. The underlying concept is that the flow velocity U_j remains non-zero, even at nodes where the oil relative permeability approaches zero, which happens if both fluids are flowing, or if the pressure difference $P_j - P_{out}$ goes to zero. During every time step condition (3.23) is evaluated implicitly, such that after

Table 3.1: Parameters and characteristic lengths and times that were used in the computations. Case 1 reflects the simulation with different treatments of the seepage face conditions, case 2 the simulation with grid refinements, case 3-10 the simulations on the unbounded domain and case 11-18 the simulations on the bounded domain.

case	L	V_0	n	α	β_{ow}	ρ_o	θ	T_e	Z_c	X_c	T_c
	m	m^3		m^{-1}		$\mathrm{kg\,m}^{-3}$		$10^3\,\mathrm{h}$	m	m	h
1	∞	0.200	3.0	1.00	2.25	700	0.0	1.00	0.444	0.450	1.29
2	10.0	1.00	3.0	1.00	2.25	700	0.0	10.0	0.444	10.0	28.6
3	∞	1.00	3.0	1.00	2.25	700	0.0	50.0	0.444	2.25	6.43
4	∞	1.00	2.0	1.00	2.25	700	0.0	50.0	0.444	2.25	6.43
5	∞	1.00	5.0	1.00	2.25	700	0.0	50.0	0.444	2.25	6.43
6	∞	1.00	3.0	2.00	2.25	700	0.0	50.0	0.222	4.50	12.9
7	∞	1.00	3.0	1.00	1.80	700	0.0	50.0	0.556	1.80	5.14
8	∞	1.00	3.0	1.00	2.25	850	0.0	50.0	0.444	2.25	5.29
9	∞	1.00	3.0	1.00	2.25	700	0.30	50.0	0.444	2.25	6.43
10	∞	1.00	3.0	1.00	2.25	700	0.45	50.0	0.444	2.25	6.43
11	10.0	1.00	3.0	1.00	2.25	700	0.0	60.0	0.444	10.0	28.6
12	10.0	1.00	2.0	1.00	2.25	700	0.0	30.0	0.444	10.0	28.6
13	10.0	1.00	5.0	1.00	2.25	700	0.0	100	0.444	10.0	28.6
14	10.0	1.00	3.0	2.00	2.25	700	0.0	100	0.222	10.0	28.6
15	10.0	1.00	3.0	1.00	1.80	700	0.0	60.0	0.556	10.0	28.6
16	10.0	1.00	3.0	1.00	2.25	850	0.0	60.0	0.444	10.0	23.5
17	10.0	1.00	3.0	1.00	2.25	700	0.30	60.0	0.444	10.0	28.6
18	10.0	1.00	3.0	1.00	2.25	700	0.45	60.0	0.444	10.0	28.6

convergence the correct outflow velocity and pressure P_j are approximated. For a flowing phase the latter becomes almost equal to P_{out}. Unfortunately, if χ is large, the convergence requires large numbers of iterations.

Alternatively, the well-conditions can be treated straightforwardly by imposing at every seepage node

$$\begin{cases} P_j = P_{out} & \text{if } U_j < 0 \\ U_j = 0 & \text{if } P_j < P_{out}. \end{cases} \tag{3.24}$$

Hence, if the pressure is imposed exactly equal to the outside pressure, the flow velocity is computed as usual from equation (3.2) using the pressure gradient over the grid element adjacent to the boundary and the element averaged oil relative permeability. For a sufficiently fine X-discretization, we obtain accurate results with a limited number of iterations. As the stiffness matrix with its modifications for Dirichlet conditions is not changed during a time step, we evaluate condition (3.24) at the end of each time step, where the automatic time stepping guarantees sufficient accuracy.

To compare the effect of the 'iterative' condition (3.23) and the 'direct'
condition (3.24), we simulated flow with the set of parameters of case 1 of
Table 3.1. A domain of 16.5 m wide and 1.5 m high was used, with uniform Z-
discretization (19 nodes). For the X-discretization (41 nodes) element widths
increased from 0.068 m to 0.679 m for increasing X. The top and bottom
boundaries were taken impermeable to both phases and the right boundary
was impermeable to oil. The water level at the well boundary at the left side
($X = 0$), was taken at 0.5 m above the bottom of the domain. At the right
boundary, water pressures were taken hydrostatic with $P_w = 0$ again at 0.5 m
above the bottom, yielding an essentially horizontal water table. At $T = 0$ h
we imposed hydraulic heads ($H_{j,i} = \dfrac{P_{j,i}}{\rho_w\, g} + \dfrac{\rho_j}{\rho_w}\, Z$) for each phase, given by

$$
\begin{aligned}
H_{w,i} &= \quad\;\; 0.0 \text{ m} \quad \text{for } 0.0 < X < 16.5 \text{ m},\; -0.5 < Z < 1.0 \text{ m} \\[4pt]
H_{o,i} &= \left\{
\begin{array}{ll}
0.0 \text{ m} & \text{for } 0.0 < X < 0.1 \text{ m},\; -0.5 < Z < 1.0 \text{ m} \\
0.172 \text{ m} & \text{for } 0.1 < X < 4.0 \text{ m},\; -0.5 < Z < 1.0 \text{ m} \\
0.0 \text{ m} & \text{for } 4.0 < X < 16.5 \text{ m},\; -0.5 < Z < 1.0 \text{ m},
\end{array}
\right.
\end{aligned}
\tag{3.25}
$$

such that 0.200 m^3 oil was present in the domain. This simulation reflects
withdrawal in an unbounded domain ($L = \infty$) in the sense of Figure 3.1.a.
Multi-phase flow during 1000 h was computed, where the well conditions were
treated either by condition (3.23) with $\chi = 100$ m^{-1} and $\chi = 1000$ m^{-1}
respectively, or by condition (3.24). In Figure 3.2 we compare the results in
terms of the vertically integrated (free) oil saturations $w_f = \phi \int S_{of}\, dz$ at three
times and in terms of the oil volume in the domain $v = \phi \int \int S_{of}\, dx\, dz$. As
oil flows out only through the well boundary, the oil volume can be obtained
from the cumulative oil outflow rate: $\int_0^t \int_z u_o(0, \zeta, \tau)\, d\zeta\, d\tau = 1 - v$. Figure 3.2
shows that as χ increases, the 'iterative' solutions appear to converge to the
solution obtained with the 'direct' condition.

Figure 3.2.c shows the oil pressure distribution at the well boundary. At
about $z = 0.35$ the well condition switches from the zero pressure to the no-
flow condition, whereas the oil pressure is hydrostatic for $z > 0.35$. This
level marks the top of the oil seepage face. For $z < 0$ the oil pressure is
equal to the water pressure and hence the oil saturation is zero, but oil flows
out at those nodes where oil is present inside the domain. We observe that
the 'iterative' condition yields a smoothed approximation of the correct oil
pressure p_o at the well boundary. For the larger value of χ the approximation
is slightly better in agreement with the exact condition. However, the number
of (Picard) iterations and time steps needed for convergence becomes very
large: the present simulation with $\chi = 100$ took about 6 h and with $\chi = 1000$
about 45 h, whereas the simulation with the 'direct' condition required only
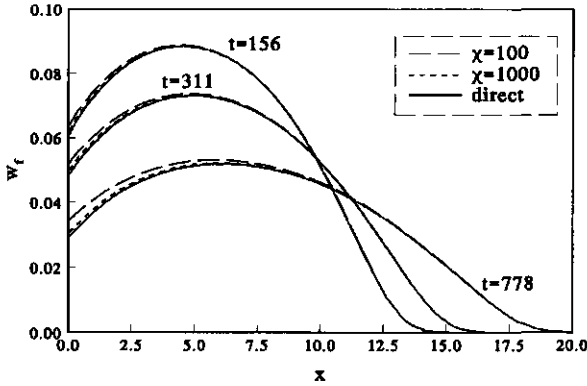
(a)
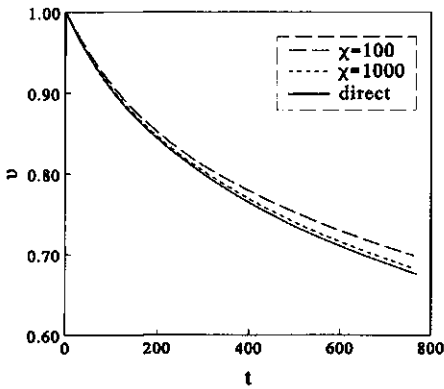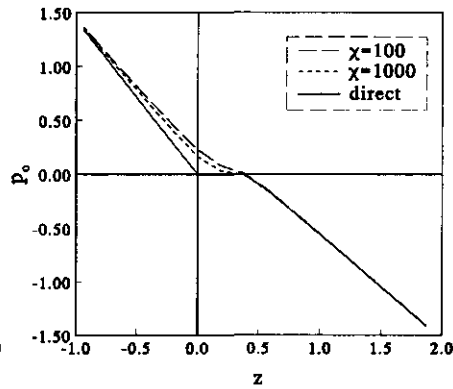
(b)   (c)

Figure 3.2: Comparison of seepage face treatment (case 1) by the 'iterative' condition (with $\chi = 100$, $\chi = 1000$) and the 'direct' condition in terms of (a) vertically integrated oil saturations w_f as a function of x, (b) oil volume in the domain v as a function of t and (c) oil pressure distribution p_o at the well boundary as a function of z at $t = 156$.

20 min. Hence, at least for this type of computations the 'direct' approach is preferable.

3.3.3   Grid refinements

Especially near the part of the well boundary where oil flows out, large pressure gradients occur and the effects of discretization may be substantial. To investigate this, we performed a series of simulations in which we refined both the X-grid and the Z-grid near the well boundary. A domain of 10.0 m wide and 2.5 m high was used. For every simulation the X-grid between 1.0 and 10.0 m had 15 elements, whose widths increased from 0.351 to 0.849 m, and the Z-grid between 0.5 and 2.0 m had 15 elements of uniform height. The X-discretization between 0.0 and 1.0 m and the Z-discretization between -0.5 and 0.5 m were varied as follows:

grid x1 : 3 elements, width increasing from 0.111 to 0.556 m,
grid x2 : 6 elements, width increasing from 0.028 to 0.306 m,
grid x3 : 12 elements, width increasing from 0.007 to 0.160 m,
grid z1 : 5 elements, height 0.20 m,
grid z2 : 10 elements, height 0.10 m,
grid z3 : 20 elements, height 0.05 m.

We considered the combinations (x1,z3), (x2,z3), (x3,z3), (x3,z1) and (x3,z2) and simulated flow with the set of parameters of case 2 of Table 3.1. The top, bottom and right boundaries were taken impermeable to both phases, which reflects withdrawal from an essentially bounded domain, see Figure 3.1.b. The water level at the well boundary was taken at 0.5 m above the bottom of the domain. At $T = 0$ h we imposed for each phase hydraulic heads

$$
\begin{aligned}
H_{w,i} &= 0.0 \text{ m} && \text{for } 0.0 < X < 10.0 \text{ m}, \; -0.5 < Z < 2.0 \text{ m} \\
H_{o,i} &= 0.215 \text{ m} && \text{for } 0.0 < X < 10.0 \text{ m}, \; -0.5 < Z < 2.0 \text{ m}
\end{aligned}
\tag{3.26}
$$

such that 1.0 m^3 oil was present in the domain. Multi-phase flow during 10000 h was simulated.

In Figure 3.3 the solutions corresponding to the refinements are presented in terms of the vertically integrated oil saturations at three times. The solutions corresponding to the x-grid refinement seem to converge, but since the differences between solutions corresponding to the z-grid refinement do not uniformly decrease, the dependence on the z-grid near the well boundary is less straightforward.

The situation near the well boundary is illustrated by Figure 3.4. In Figure 3.4.a oil pressures are given for X between 0.0 and 0.5 m and Z between -0.5 and 0.5 m in dimensionless variables at $T = 10000$ h. Observe that
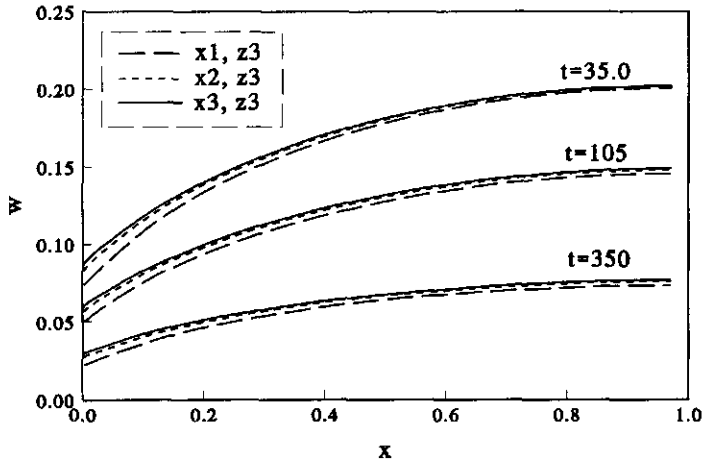
(a)
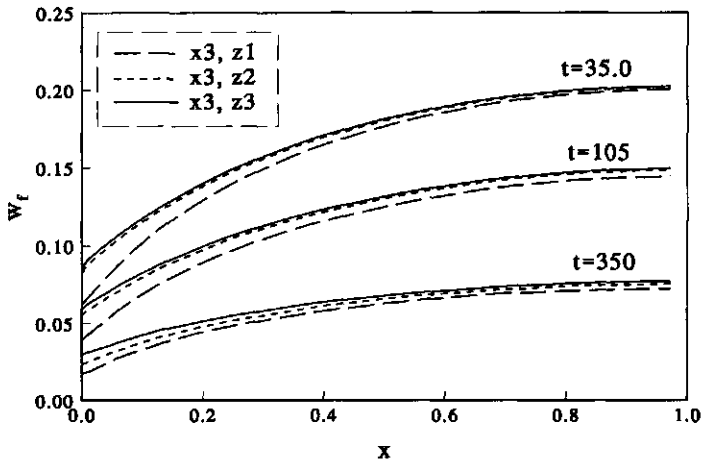
(b)

Figure 3.3: Vertically integrated oil saturations w_f (case 2) as a function of x for refinement of the x-grid near the well boundary (a) and for refinement of the z-grid near the well boundary (b).

(a)   (b)
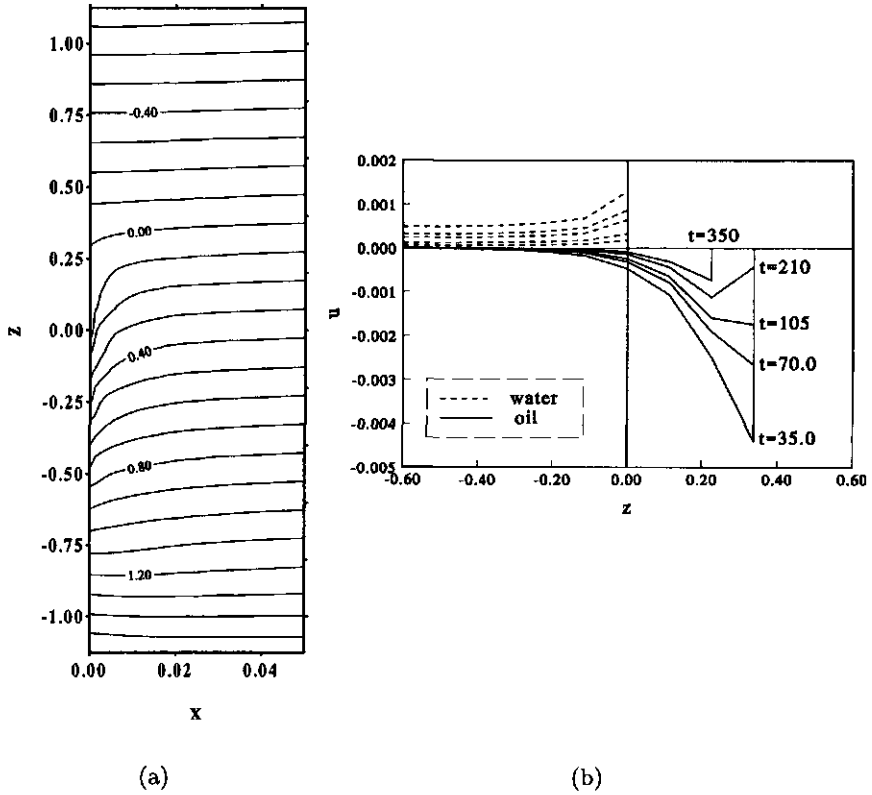
Figure 3.4: Oil pressure contour lines in the neighborhood of the well boundary at $t = 350$ (a) and water and oil flow velocities at the well boundary at several times (b) for the grid refinement (x3,z3) (case 2).

roughly above $z = 0.30$ oil pressures are negative and nearly hydrostatically distributed and no oil flows out. Below $z = -0.80$ oil pressures are equal to the hydrostatic water pressures, which means that oil is neither present nor does it flow out. Between $z = -0.80$ and $z = 0.30$ oil flows out and large oil pressure gradients occur, which cause numerical difficulties.

Figure 3.4.b shows the horizontal water u_w and oil u_o flow velocities at the well boundary between $z = -0.60$ and $z = 0.60$ at 5 different times. For the present situation with no decline of the water table throughout the domain only water inflow occurred below the well water level. Oil flowed out mainly above this water level with velocities, that were much larger than the water inflow velocities. Between $t = 210$ and $t = 350$ the maximum level where oil

flowed out, i.e. the top of the oil seepage face, decreased from $z = 0.3375$ to $z = 0.225$, which are the positions of two horizontal grid lines. As oil outflow is maximum just below and vanishes abruptly at the top of the seepage face, this may be another source of numerical difficulties.

3.3.4 Sensitivity analysis

With condition (3.24) and grid refinement (x3,z3) near the seepage boundary, we performed a series of simulations in which we varied parameters as shown in Table 3.1, with case 3 as a reference case for the unbounded domain simulations 3 to 10 and case 11 for the bounded domain simulations 11 to 18. For the unbounded domain the X-grid (from 1 to 55 m) consisted of 42 elements, whose widths increased from 0.356 to 2.215 m, and the Z-grid for the entire domain was the same as near the well boundary, with 15 elements of uniform height between 0.5 and 2.0 m, which yielded 1980 nodepoints in total. Initially, we imposed water hydraulic heads $H_{w,i} = 0.0$ m throughout the entire domain and oil hydraulic heads such that 1.0 m^3 oil was present in the domain (e.g. for case 3 $H_{o,i} = 0.215$ m for $0.0 < X < 9.6$ m, $H_{o,i} = 0.107$ m for $9.6 < X < 12$ m and $H_{o,i} = 0.0$ m for $X > 12$ m). These computations took typically 16 h on a HP 9000 735/125 workstation. For the bounded domain the discretization (1008 nodepoints) and initial conditions were taken the same as in case 2. The corresponding computation times were typically about 3 h.

For the unbounded domain cases the profiles of w_f were similar to those shown in Figure 3.2.a, whereas for the bounded domain cases the profiles looked like those of Figure 3.3. The varied parameters n, α, β_{ow} and ρ_o most likely affect the thickness of the oil layers and thus the seepage flow rate.

In Figure 3.5 we present the removal rates, i.e. the evolution of v. We observe that removal happens much slower in the unbounded domain (Figure 3.5.a) than in the bounded domain (Figure 3.5.b). As expected the van Genuchten parameter n largely affects the removal rate, in the sense that large values of n correspond with slow removal (cases 5 and 13). The effects of changing α, β_{ow} and ρ_o (cases 6, 7, 8, 14, 15 and 16) are not very large. The larger value of the parameter α (cases 6 and 14) slightly fastens the removal, which is contrary to the effect that α has on other processes like oil lens redistribution, see e.g. Chapter 2. The coincidence of cases 7 and 8 happened by chance. As expected also the trapping parameter θ is important, especially because a large amount of oil cannot be removed at all.

In Figure 3.6 we present for the unbounded domain cases the first moment in x-direction of the vertically integrated free oil saturations $M_1 = \phi \int x \, w_f \, dx \, dz$. These moments itself have no important physical meaning, but we observe that for most cases they became almost constant after a very
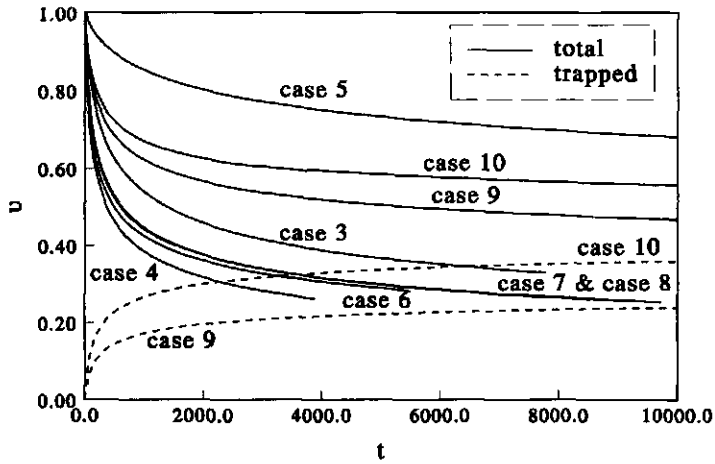
(a)
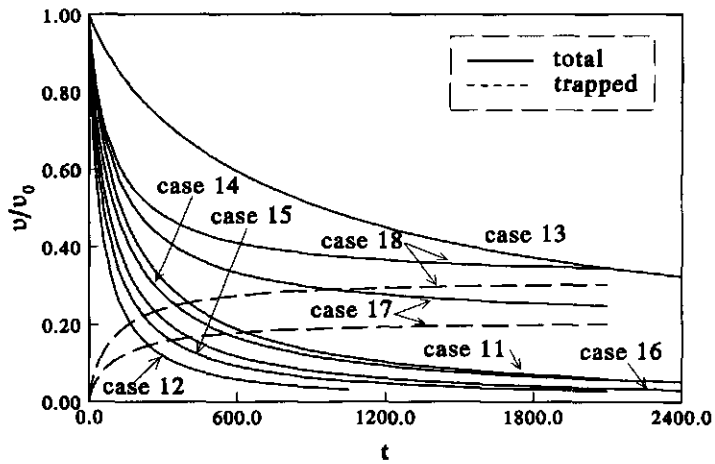
(b)

Figure 3.5: Oil volumes as a function of time (a) for the unbounded domain and (b) for the bounded domain (relative to the initial volume). For cases 9, 10, 17 and 18 also the trapped oil volumes are shown.
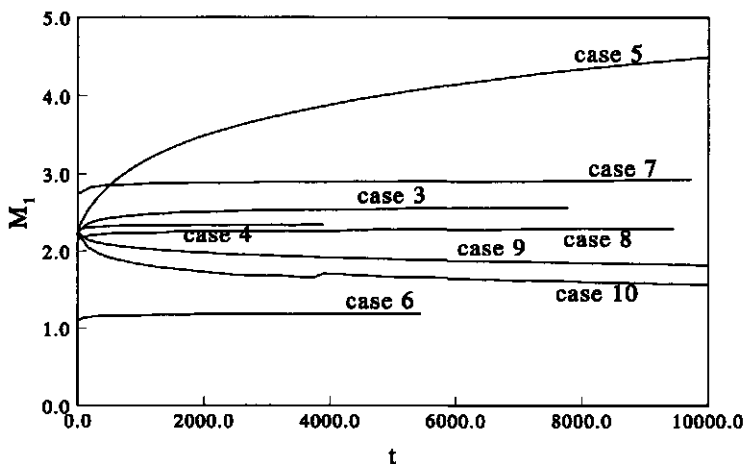
Figure 3.6: First moments of the vertically integrated free oil saturations as a function of time for the unbounded domain.

short time, which we will come back to in Section 3.4.3. Only for a large value of n (case 5) and for the entrapment cases 9 and 10 the moment did not become constant.

3.4 Analytical approximations

3.4.1 Reduced equations

To obtain analytical approximations for the decay of the oil lens at an essentially horizontal water table, we assume that vertical oil velocities can be neglected. According to [9] a necessary condition for this vertical flow equilibrium is that the horizontal extension of the lens is much larger than its vertical extension, say $X_l/(Z_u - Z_{ow}) \gg 1$. Then, the vertical capillary and the gravitational forces balance and capillary pressures are hydrostatically distributed. Furthermore, if additionally the oil saturations, and thus the oil mobilities, are much smaller than the water saturations and mobilities, we may assume that the water pressures are hydrostatically distributed with reference level $p_w = 0$ at $z = 0$, and thus water and oil flow are segregated. The numerical results indicate that the vertical equilibrium assumption is justified shortly after the start of the flow process everywhere in the lens away from the well boundary, see also Chapter 2. The vertical pressure distributions are given by

$$p_w = -\frac{\rho_w}{\rho_o} z \qquad \text{for} - \infty < z < \infty \qquad (3.27)$$

$$p_o = z_{ao} - z \qquad \text{for } z_{ow} < z < z_u. \tag{3.28}$$

According to definition (3.10) we may relate the separating levels in the oil lens by

$$z_{ow} = -\frac{\rho_o}{\Delta \rho} z_{ao}, \quad z_u = \frac{\beta_{ow}}{1 - D} z_{ao} \quad \text{with } D = \frac{\beta_{ow} \Delta \rho}{\beta_{ao} \rho_o} \tag{3.29}$$

and $\Delta \rho = \rho_w - \rho_o$. To ensure that oil is confined to layers of finite thickness, we take $D < 1$ [11, 39]. Neglecting vertical velocities, equation (3.19) for oil

$$\phi \frac{\partial S_o}{\partial t} - \frac{Z_c}{X_c} \frac{\partial}{\partial x} \left(k_{rj} \frac{\partial z_{ao}}{\partial x} \right) = 0 \tag{3.30}$$

describes the entire flow process, see Section 2.3.1.

Because vertical pressure distributions are hydrostatic, we further reduce equation (3.30) by vertical integration, which requires evaluation of

$$w_f = \phi \int_{z_{ow}}^{z_u} S_{of} \, dz = \phi \int_{z_{ow}}^{z_u} (S_t - S_{wa}) \, dz \tag{3.31}$$

$$\bar{k} = \int_{z_{ow}}^{z_u} k_{ro}(S_{wa}, S_t) \, dz = \int_{z_{ow}}^{z_u} k_{ro}(S_{wa}, S_t) \, dz, \tag{3.32}$$

where $w_f(r, t)$ represents the free oil volume per unit lateral area and $\bar{k}(r, t)$ the vertically integrated relative permeability, see Section 2.3.3. To rewrite equation (3.30) in terms of the variable w_f only, we approximate both $\bar{k}$ and z_{ao} by power law functions of w_f as described in Appendix 2A. We obtain

$$z_{ao} = \lambda_1 \, w_f^{\frac{1}{n+1}} \quad \text{and} \quad \bar{k} = \lambda_2 \, w_f^{\frac{5n-2}{2(n+1)}}, \tag{3.33}$$

where λ_1 and λ_2 are given by

$$\lambda_1 = \phi^{\frac{-1}{n+1}} \left(\frac{n(n+1)}{n-1} \right)^{\frac{1}{n+1}} \left(\frac{\Delta \rho}{\rho_w} \right)^{\frac{1}{n+1}} (1 - D)^{\frac{n}{n+1}} \tag{3.34}$$

$$\lambda_2 = \phi^{\frac{2-5n}{2(n+1)}} \left(\frac{n-1}{n} \right)^{\frac{3-4n}{2(n+1)}} (n+1)^{\frac{5n-2}{2(n+1)}} \left(\frac{\Delta \rho}{\rho_w} \right)^{\frac{3n-4}{2(n+1)}} *$$

$$* \left(\frac{2}{5n-2} (1 - D)^{\frac{n(5n-2)}{2(n+1)}} + \frac{D}{(1 - D)^{\frac{5n-2}{2(n+1)}}} I_k \right) \tag{3.35}$$

and I_k is the integral given by (2.72).

Additionally, we define $w_o(r, t)$ as the total oil volume per unit lateral area, $w_t(r, t)$ as the trapped oil volume, with $w_t = w_o - w_f$, and $w_m(r, t)$ as the maximum oil volume, i.e.

$$w_m(r, t) = \max_{t' \leq t} w_f(r, t'). \tag{3.36}$$

The hydrostatic pressure assumption implies that for every lateral position the integrated apparent water saturation attains its minimum at the time w_f attains its maximum. Hence, the vertically integrated trapping mechanism (3.8) is given by

$$
w_t = \begin{cases} c_t \left(w_m - w_f \right) & \text{if } \dfrac{\partial w_f}{\partial t} \leq 0 \\[3mm] 0 & \text{if } \dfrac{\partial w_f}{\partial t} > 0 \end{cases}
\tag{3.37}
$$

at every lateral position where w_f is positive, with $c_t = \dfrac{\rho_o}{\rho_w}\,\theta$, see Appendix 2B. Writing the vertically integrated time derivative of equation (3.30) as

$$
\frac{\partial w_o}{\partial t} = \begin{cases} \dfrac{\partial w_f}{\partial t} & \text{if } \dfrac{\partial w_f}{\partial t} > 0 \\[3mm] \dfrac{\partial w_f}{\partial t}\left(1 - c_t \right) & \text{if } \dfrac{\partial w_f}{\partial t} \leq 0, \end{cases}
\tag{3.38}
$$

we arrive at the nonlinear diffusion equation

$$
F\left(\frac{\partial w_f}{\partial t} \right) = \gamma \frac{\partial}{\partial x} \left(w_f^m \frac{\partial w_f}{\partial x} \right) \quad \text{for } t > 0,\ 0 < x < x_l,
\tag{3.39}
$$

where

$$
p = \frac{1}{1 - c_t}, \qquad p \geq 1
\tag{3.40}
$$

$$
\gamma = \frac{Z_c\, p\, \lambda_1\, \lambda_2}{X_c\, (n + 1)}
\tag{3.41}
$$

$$
m = \frac{3n - 2}{2\,(n + 1)}, \qquad \frac{1}{4} < m < \frac{3}{2}
\tag{3.42}
$$

and F is defined for argument y by

$$
F(y) = \begin{cases} p\,y & \text{if } y > 0 \\ y & \text{if } y \leq 0. \end{cases}
\tag{3.43}
$$

Observe that if entrapment is not included, $p = 1$ and $F(y) = y$ for all y, whereas for the bounded domain w_f is decreasing everywhere and simply yields $F(y) \equiv y$.

Near the well boundary oil pressures are not hydrostatically distributed and equation (3.39) is not valid. Therefore, it is not possible to relate w_f to the level z_{ao} (3.33) and to transform the well condition (3.20) into an appropriate condition for w_f at the well boundary. However, we know that below the well water level oil saturations are zero and we assume that the part

of the seepage boundary above the water level is small. Hence, we impose the Dirichlet condition

$$w_f(0,t) = 0 \tag{3.44}$$

and mention that for (3.44) the outflow rate $q(t) = -\gamma\, w_f^m\, \dfrac{\partial\, w_f}{\partial\, x}(0,t)$ is nonzero provided $\dfrac{\partial\, w_f}{\partial\, x}(0,t) = \infty$.

Furthermore, if $L < \infty$ we impose at the right boundary the no-flow condition

$$\frac{\partial\, w_f}{\partial\, x}(1,t) = 0. \tag{3.45}$$

The initial condition corresponding to (3.14) is

$$w_f(x,0) = w_i(x), \tag{3.46}$$

where $w_i = \phi \int S_i\, dz$ is the initial oil volume per unit lateral area. According to condition (3.15) w_i satisfies

$$\int_0^{x_l} w_i(x)\, dr = v_0. \tag{3.47}$$

For $L = \infty$ we mention two important features of w_f which can be verified easily. The 'diffusion' coefficient w_f^m vanishes for $w_f = 0$, which implies that the free boundary x_l which separates the regions where $w_f > 0$ and $w_f = 0$, is at every time at finite distance from the z-axis. Considering that the speed s_l at which the free boundary moves is equal to the horizontal oil velocity at the free boundary, this speed is given by [7, 10]

$$s_l = \lim_{x \uparrow x_l} w_f^{m-1}\, \frac{\partial\, w_f}{\partial\, x}. \tag{3.48}$$

Furthermore, if $p = 1$ the first moment of w_f satisfies [7]

$$\int_0^{x_l} x\, w_f\, dx = \text{const.} \tag{3.49}$$

3.4.2   Analytical solutions

Equation (3.39) is the (modified) porous medium equation which admits similarity solutions of the form [6, 30]

$$w_{fa}(x,\bar{t}) = \bar{t}^{-\mu}\, h(x\,\bar{t}^{-\nu}), \tag{3.50}$$

with constant μ and ν. We have introduced $\bar{t} = \gamma\,(t - t_0)$ with t_0 representing the time at which the solution becomes singular.

For $L < \infty$, the solution of equation (3.39) is positive on the fixed region $[0, 1]$, which requires $\nu = 0$, and the transformation (3.50) is a simple separation of variables. Substitution of (3.50) with $\nu = 0$ into equation (3.39) yields $\mu = \dfrac{1}{m}$ and the ordinary differential equation

$$(h^m h')' = -\frac{h}{m} \quad \text{for } 0 < \eta < 1 \tag{3.51}$$

for $h(\eta)$, with $\eta \equiv x$. To facilitate the computation of h, we apply the scaling

$$\tilde{h}(\xi) = C^{-\frac{2}{m}} h(C\,\xi), \quad \xi = \frac{\eta}{C}, \tag{3.52}$$

for any positive constant C (2.52). In this case we take $C = 1$, because the length of the domain is equal to 1 and $\tilde{h}$ is the solution of equation (3.51) on the domain $0 < \xi < 1$, where primes $'$ denote differentiation with respect to ξ.

Scaling of the boundary conditions (3.44) and (3.45) yields $\tilde{h}(0) = 0$ and $\tilde{h}'(1) = 0$. To derive the corresponding solution of equation (3.51), which was obtained by Boussinesq [9] for $m = 1$, we substitute $\tilde{y} = -\tilde{h}^m \tilde{h}'$, the transformed oil flux. The resulting equation for $\tilde{y}(\tilde{h})$ has the solution

$$\tilde{y}(\tilde{h}) = -\sqrt{\frac{2}{m\,(m+2)}}\sqrt{\tilde{h}^{m+2}(1) - \tilde{h}^{m+2}}. \tag{3.53}$$

Hence, we obtain implicitly for $\tilde{h}(\xi)$

$$\xi = \sqrt{\frac{m\,\tilde{h}^m(1)}{2\,(m+2)}}\, B_{\left(\frac{\tilde{h}(\xi)}{\tilde{h}(1)}\right)^{m+2}}\left(\frac{m+1}{m+2}, \frac{1}{2}\right), \tag{3.54}$$

where

$$B_\zeta(a, b) = \int_0^\zeta \tau^{a-1}(1 - \tau)^{b-1}\, d\tau, \tag{3.55}$$

is the incomplete B-function. Substitution of $\xi = 1$ into equation (3.54), yields the value of $\tilde{h}(1)$. Inserting $\tilde{h}(1)$ in (3.53) gives the flux $\tilde{y}(\tilde{h})$, in particular at $\xi = 0$.

For $L = \infty$, we write the similarity solution (3.50) for convenience as

$$w_{fa}(x, t) = \begin{cases} \bar{t}^{-\mu}\, h(x\,\nu^{\frac{1}{2}}\,\bar{t}^{-\nu}) & \text{for } 0 < x < A\,\nu^{-\frac{1}{2}}\,\bar{t}^{\nu} \\ 0 & \text{for } x \geq A\,\nu^{-\frac{1}{2}}\,\bar{t}^{\nu}, \end{cases} \tag{3.56}$$

where $A \nu^{-\frac{1}{2}} \bar{t}^{\nu}$, with positive A, represents the free boundary beyond which $w_{fa} = 0$. Substitution of (3.56) into equation (3.39) shows that the similarity profile $h(\eta)$, with variable $\eta = x \nu^{\frac{1}{2}} \bar{t}^{-\nu}$, satisfies the equation

$$(h^m h')' = F(-\eta h' - k h) \quad \text{for } 0 < \eta < A, \tag{3.57}$$

with $k = \dfrac{\mu}{\nu}$, and μ and ν satisfying

$$2\nu + m\mu - 1 = 0. \tag{3.58}$$

Observe that the moment $M_{k-1} = \int x^{k-1} w_f \, dx$ (2.53) for the similarity solution (3.56) is independent of time, i.e.

$$M_{k-1,a} = \nu^{-\frac{1}{2}k} \int_0^A \eta^{k-1} h(\eta) \, d\eta, \tag{3.59}$$

which is a generalization of property (3.49).

After the scaling (3.52) with $C = A$, $\tilde{h}$ is the solution of equation (3.57) for $0 < \xi < 1$. Boundary condition (3.44) yields $\tilde{h}(0) = 0$ and at the free boundary we have $\tilde{h}(1) = 0$.

For $p = 1$ property (3.49) requires $k = 2$, i.e.

$$\mu = 2\nu = \frac{1}{m+1}, \tag{3.60}$$

and equation (3.57) has the explicit Dipole solution [8, 30]

$$\tilde{h}(\xi) = \left(\frac{m(m+1)}{m+2} \left(\xi^{\frac{m}{m+1}} - \xi^2 \right) \right)^{\frac{1}{m}}. \tag{3.61}$$

The transformed oil flux $\tilde{y} = -\tilde{h}^m \tilde{h}'$ at $\xi = 0$ is given by

$$\tilde{y}(\xi = 0) = -\frac{1}{m+1} \left(\frac{m(m+1)}{m+2} \right)^{1+\frac{1}{m}}. \tag{3.62}$$

The first moment of $\tilde{h}$, which is the transformed version of the moment (3.59) for $k = 2$, i.e. $\int \xi \tilde{h} \, d\xi$, is given by

$$\tilde{M}_1 = \frac{m+1}{m+2} \left(\frac{m(m+1)}{m+2} \right)^{\frac{1}{m}} B\left(\frac{m+1}{m+2} + 1, \frac{1}{m} + 1 \right), \tag{3.63}$$

where $B = B_1$ (3.55) is the B-function.

For $p > 1$ the trapping parameter k and the solution of equation (3.57) cannot be found exactly. Hence, we compute numerically the similarity profile and the value of k, see also Appendix 2C, for which the procedure is described in Appendix 3A. We obtain the trapping parameter k as a function of p, which is shown in Figure 3.7 for different m-values.

In Appendix 3B we show that a similarity solution similar to (3.56) can be obtained for oil removal in a semi-infinite three-dimensional domain.
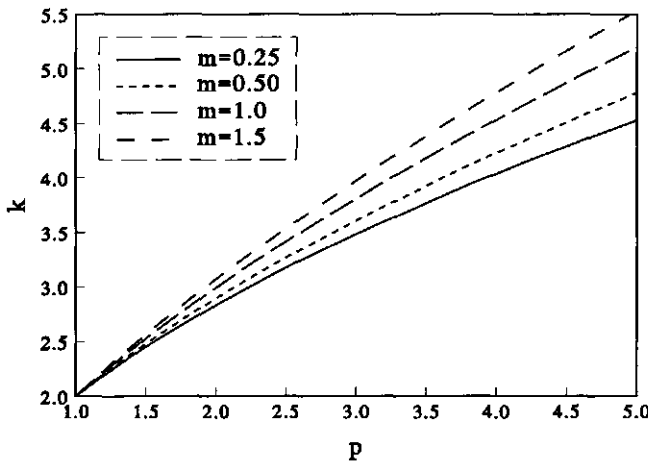
Figure 3.7: Parameter k as a function p for several values of m.

3.4.3 Agreement between numerical and analytical approximations

The similarity solutions $w_{fa}(x,\bar{t})$ only provide reasonable approximations of the withdrawal process, if we find appropriate values of t_0 and also of A for the unbounded domain. As the initial condition (3.46) in general does not have the similarity shape and as vertical equilibrium conditions are only established some time after the start of the flow process, we estimate the unknown values from oil lens (shape) properties after a sufficiently large time, rather than from the initial condition. We compute t_0 and A from the numerical solutions for the free oil volume per unit lateral area w_{fn} of Section 3.4.1, where the subscript n identifies the numerical solution, by comparing w_{fn} with the analytical w_{fa} of Section 3.4.2. In practice, it is relatively easy to determine t_0 and A by measuring the outflow rate and by comparing it with the analytically obtained outflow rate. Measuring once yields the value of t_0 for the bounded domain, whereas measuring at two different times yields the values of both A and t_0 for the unbounded domain.

To obtain the values of A and t_0 from the numerical solution for $L = \infty$ (cases 3-10 of Table 3.1), we use at one time the moment M_{k-1} (3.59) and the oil outflow rate, $q(t) = \int_0^t \int_z u_o(0,\zeta,\tau)\,d\zeta\,d\tau$. Observe from Figure 3.6 that except for case 5 (large n) all cases with zero entrapment ($k = 2$) had an approximately time-independent first moment in agreement with (3.49) after a short time. In case of entrapment (case 9 and 10) we computed $k = 2.29$ and $k = 2.48$ respectively and $M_{k-1,n}$ became time-independent as well. This indicates that, except for a large value of n (case 5), the flow processes

Table 3.2: Parameter values for the similarity solution and deviations of the analytical solution from the numerical solution.

case	γ	A	t_0	Δv	case	γ	t_0	Δv
3	0.0680	1.68	-188	0.0305	11	0.0153	-207	0.0821
4	0.100	1.89	-63.3	-0.00766	12	0.0225	-83.6	0.114
5	0.0621	1.62	-1250	0.359	13	0.0140	-330	0.710
6	0.0170	1.41	-104	-0.0106	14	0.00764	-266	0.0127
7	0.215	1.74	-92.9	0.00794	15	0.0387	-101	0.0744
8	0.108	1.64	-92.1	0.0196	16	0.0244	-137	0.0225
9	0.0860	1.63	6.82	0.0269	17	0.0194	-168	0.105
10	0.0992	1.60	-30.1	0.0573	18	0.0223	-180	0.138

quickly satisfied the vertical equilibrium conditions and that the boundary condition (3.44) was a good approximation of the non-reduced well condition. For the similarity solution we have

$$M_{k-1,a} = \nu^{-\frac{1}{2}k} A^{k+\frac{2}{m}} \tilde{M}_{k-1}, \tag{3.64}$$

where $\tilde{M}_{k-1} = \int \xi^{k-1} \tilde{h} \, d\xi$, the moment in terms of the transformed $\tilde{h}(\xi)$ (3.52), which is given by (3.63) for $k = 2$ and obtained numerically for $k > 2$. By identifying $M_{k-1,n}$ and $M_{k-1,a}$ at $t = 0.1 t_e$, we obtained the values of A, which are listed in Table 3.2.

The outflow rate is given for the similarity solution by

$$q_a(\bar{t}) = -\gamma w_{fa}^m \frac{\partial w_{fa}}{\partial x}(0,\bar{t}) = \gamma \nu^{\frac{1}{2}} \bar{t}^{-(m+1)\mu-\nu} A^{1+\frac{2}{m}} \tilde{y}(\xi = 0), \tag{3.65}$$

with $\bar{t} = \gamma(t - t_0)$. For $p = 1$ $\tilde{y}(\xi = 0)$ is given by (3.62) and for $p > 1$ it is computed numerically. We identify q_a and its numerical equivalent q_n at $t = 0.1 t_e$ and obtain the values of t_0, which are also listed in Table 3.2.
The values of k, A and t_0 determine $w_{fa}(r, \bar{t})$. In Figure 3.8.a we present w_{fn} and w_{fa} for case 3 at several times. Observe that the agreement between the profiles is good, except near $x = 0$.

In Figure 3.8.b we present also the free oil volume v which is a global and practically relevant characteristic. The analytically and numerically obtained volumes show very good agreement at all times. For all cases (3-10) we calculated the relative deviations of v at the maximum computed time t_e

$$\Delta v = \frac{v_n(t_e) - v_a(t_e)}{v_n(t_e)}. \tag{3.66}$$

The values of Δv which are listed in Table 3.2, are less than 6 percent, except for large n.
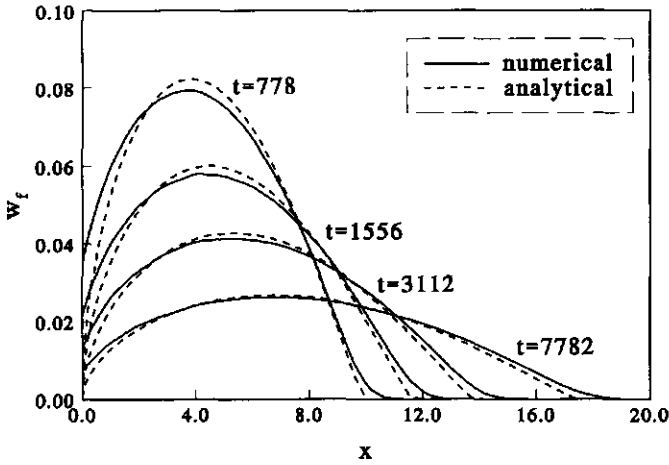
(a)
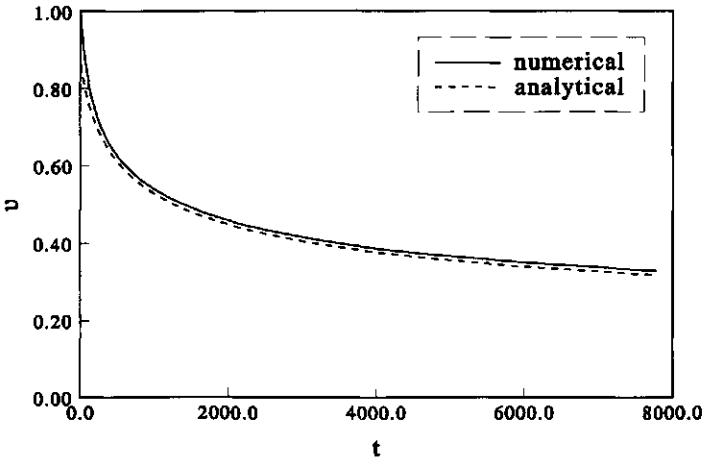
(b)

Figure 3.8: Numerical and analytical free oil volumes per unit lateral area (a) and free oil volumes in the domain (b) for case 3 after fitting parameters at $t = 778$.

When oil entrapment is taken into account (cases 9-10), the trapped oil volume per unit lateral area according to the analytical solution can be found from relation (2.55).

For $L < \infty$ we obtain the value of t_0 by identifying the numerical oil outflow rate $q_n(t)$ at $x = 0$ and the outflow rate corresponding to the similarity solution, i.e.

$$q_a(\bar{t}) = -\gamma \, w_{fa}^m \frac{\partial \, w_{fa}}{\partial \, x}(0, \bar{t}) = \gamma \, \bar{t}^{-\frac{1}{m}-1} \, \tilde{y}(\xi = 0), \qquad (3.67)$$

with $\tilde{y}(\xi = 0)$ given by (3.53), at $t = 0.1 \, t_e$. In Figure 3.9 we present w_{fn} and w_{fa} for case 11 at several times and the free oil volumes v_n and v_a. The profiles show good agreement, except near $x = 0$ and the volumes agree very well at all times. For all cases (11-18) we computed also the deviations Δv (3.66), which are listed in Table 3.2. These deviations are less than 14 percent, except for large n (case 13). The deviations for the bounded domain are slightly larger than for the unbounded domain. This may be caused by numerical errors, as the absolute values of the remaining free oil volumes for the bounded domain became very small, see Figures 3.5.b and 3.9.b.

Although the approximation (3.44) of the well boundary condition, i.e. $w_f(0, t) = 0$, is not in agreement with the numerically obtained free oil volume per unit lateral area $w_{fn}(0, t)$, see Figures 3.8.a and 3.9.a, this approximation leads to almost correct outflow rates and thus to almost correct solutions. At the well boundary most oil is present above the oil seepage face, where no outflow occurs. This means that the largest fraction of $w_{fn}(0, t)$ does not contribute to the outflow rate. For large values of n (cases 5 and 13) as well as for small values of α (not shown here) the analytical approximations are less accurate and removal happens relatively slowly. For these parameter values the capillary pressure functions ($P_{ow}(S_{wa})$, $P_w(S_{wa})$ and $P_{ao}(S_t)$ of relations (3.4,3.5)) decrease rapidly from a relatively large value to zero, when the respective saturations approach one. This behavior corresponds to large entry pressures, which may explain that a larger fraction of $w_{fn}(0, t)$ contributes to the outflow rate and that the approximation (3.44) of the well boundary condition is less adequate.

3.5 Conclusions

We modeled withdrawal of a lens of organic contaminant in a two-dimensional domain, which is either finite or semi-infinite in the horizontal direction. At the well we imposed seepage face conditions for multi-phase flow, i.e. a phase can only flow out, in which case its pressure is equal to the pressure outside the soil.
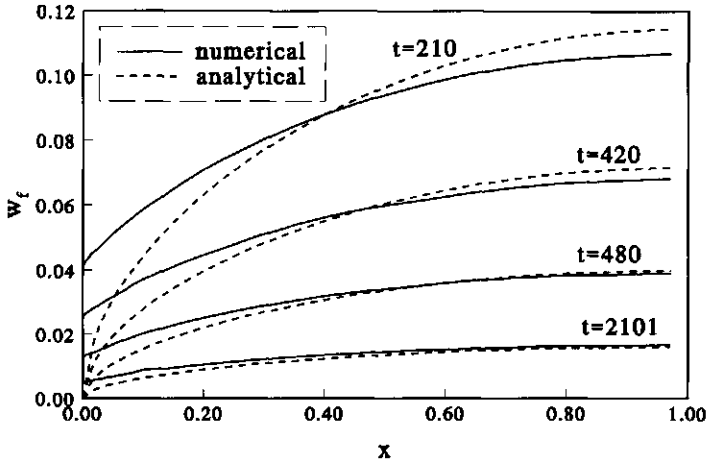
(a)
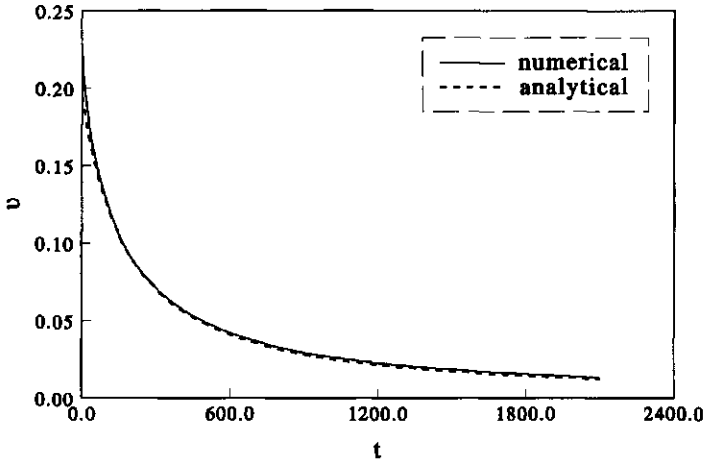
(b)

Figure 3.9: Numerical and analytical free oil volumes per unit lateral area (a) and free oil volumes in the domain (b) for case 11 after fitting parameters at $t = 210$.

Using a numerical multi-phase flow model we simulated the withdrawal process with a constant fluid level in the well that is equal to the phreatic surface in the soil. Implementation of the seepage face conditions as sink terms with a large artificial productivity index, as was proposed earlier, was compared with the direct implementation of the variational condition. For increasing values of the index the sink term solutions converged to the 'direct' solutions, but required much more computation time. Hence, the 'direct' implementation is both more accurate and more efficient. Close to the well boundary steep pressure gradients occurred. Refinement of the X-grid led to convergence of solutions near the seepage face. Oil outflow velocities showed a steep peak in vertical direction just below the top of the oil seepage face, which required very accurate discretization. Simulations for different parameters showed that removal was slower in the semi-infinite domain in which the oil lens continued to spread horizontally. For large values of the parameter n the removal rate was small. Even for the present simulations with no drawdown of the water table much oil became entrapped.

To derive analytical approximations we assumed vertical equilibrium of the oil lens and we integrated the oil flow equation vertically. We approximated the seepage face conditions by taking the oil volume per unit lateral area equal to zero, yielding however a nonzero outflow rate. Both for the bounded and the unbounded domain similarity solutions of the resulting differential equations were available, which were either explicit or easy to compute. For the unbounded domain a time-independent moment of the similarity solution was determined. The approximate independence of time of this moment for the corresponding numerical solution justified the vertical equilibrium assumption and the approximation of the well boundary condition. Comparison of the analytical and numerical moments for short times yielded the value of one of the unknown constants in the analytical solution. The remaining unknown constant was obtained by comparison of the numerically and analytically obtained outflow rates for the bounded and the unbounded domain. After fitting the two constants for a small time, the analytical solution was used to predict for larger times. Except for larger values of n, the agreement between analytical approximations and numerical results was good. In practice, the determination of the two constants in the analytical solution may be done using outflow rates, which are easily accessible, for two different times.

Appendix 3A

Evaluation of the ordinary differential equation

For the scaled variable $\tilde{h}(\xi)$ we solve the nonlinear differential equation

$$(\tilde{h}^m \tilde{h}')' = F(-\xi \tilde{h}' - k\tilde{h}) \quad \text{for } 0 < \xi < 1, \tag{3.68}$$

with boundary conditions

$$\tilde{h}(0) = 0, \quad \tilde{h}(1) = 0. \tag{3.69}$$

Furthermore, in view of condition (3.48) we impose

$$\tilde{h}^{m-1} \tilde{h}'(1) = -p. \tag{3.70}$$

Therefore, on the right half of the domain we transform equation (3.68) into a system of two differential equations with

$$y_{r,1} = \tilde{h}^m \quad \text{and} \quad y_{r,2} = \tilde{h}^{m-1} \tilde{h}'. \tag{3.71}$$

This yields

$$\begin{cases} y'_{r,1} &= m\, y_{r,2} \\ y'_{r,2} &= -\dfrac{y_{r,2}^2}{y_{r,1}} + F\left(-\xi\dfrac{y_{r,2}}{y_{r,1}} - k\right) \end{cases} \quad \text{for } \frac{1}{2} < \xi < 1, \tag{3.72}$$

with boundary conditions $y_{r,1}(1) = 0$ and $y_{r,2} = -p$.

Since near $\xi = 0$ the flux $\tilde{h}^m \tilde{h}'$ is nonzero and bounded, on the left half of the domain we transform equation (3.68) into a system of two differential equations with

$$y_{l,1} = \tilde{h}^{m+1} \quad \text{and} \quad y_{l,2} = \tilde{h}^m \tilde{h}'. \tag{3.73}$$

This yields

$$\begin{cases} y'_{l,1} &= (m+1)\, y_{l,2} \\ y'_{l,2} &= F\left(-\xi\dfrac{y_{l,2}}{y_{l,1}^{\frac{m}{m+1}}} - k\, y_{l,1}^{\frac{1}{m+1}}\right) \end{cases} \quad \text{for } 0 < \xi < \frac{1}{2}, \tag{3.74}$$

with boundary condition $y_{l,1}(0) = 0$.

Imposing continuity of $\tilde{h}$ and $\tilde{h}'$ at $\xi = \dfrac{1}{2}$, the two systems (3.72) and (3.74) are solved sequentially by shooting backward from $\xi = 1$ using a fourth order Runge-Kutta scheme. As $y_{l,1}(0)$ varies monotonically with k we can use a simple iteration to vary k until the solution satisfies $y_{l,1}(0) = 0$.

Appendix 3B

Removal in a three-dimensional domain

Removal of oil through a horizontal ditch in a three-dimensional semi-infinite domain under vertical flow equilibrium conditions is described similar to equation (3.39) by

$$F\left(\frac{\partial w_f}{\partial t}\right) = \gamma \nabla \cdot (w_f^m \nabla w_f) \quad \text{for } t > 0, \ 0 < x_1 < \infty, \ 0 < x_2 < f(x_1, t) \tag{3.75}$$

where the ditch is located at $x_1 = 0$. The curve $x_2 = f(x_1, t)$ defines the free boundary beyond which no oil is present and we assume that f is finite for all values of $x_1 \geq 0$ and $t > 0$. Similar to (3.44) and (3.46) we impose

$$w_f(0, x_2, t) = 0 \tag{3.76}$$

and

$$w_f(x_1, x_2, 0) = w_i(x_1, x_2), \tag{3.77}$$

with

$$\int_0^\infty \int_0^f w_i(x_1, x_2) \, dx_2 \, dx_1 = 1, \tag{3.78}$$

the prescribed initial volume. Furthermore, we impose by symmetry

$$\frac{\partial w_f}{\partial x_2}(x_1, 0, t) = 0. \tag{3.79}$$

In analogy to (3.56) equation (3.75) admits a similarity solution of the form [30]

$$w_{fa}(x_1, x_2, t) = t^{-\mu} h(\vec{\eta}), \quad \vec{\eta} = \begin{pmatrix} \eta_1 \\ \eta_2 \end{pmatrix} = \nu^{\frac{1}{2}} t^{-\nu} \begin{pmatrix} x_1 \\ x_2 \end{pmatrix}, \tag{3.80}$$

with constants μ and ν satisfying (3.58), which is positive for $0 < \eta_1 < a$ and $0 \leq \eta_2 < g(\eta_1)$ with $a = g(0)$. The set $\Gamma = \{0 \leq \eta_1 \leq a, \eta_2 = g(\eta_1)\}$ denotes the free boundary for the similarity solution. Substitution of (3.80) into equation (3.75) yields

$$\nabla \cdot (h^m \nabla h) + \vec{\eta} \cdot \nabla h + k \, h = 0 \quad \text{for } 0 < \eta_1 < a, \ 0 < \eta_2 < g(\eta_1), \tag{3.81}$$

with $k = \dfrac{\mu}{\nu}$. Imposing the transformed versions of conditions (3.76) and (3.78), i.e.

$$h(\vec{\eta})|_{\eta_1 = 0} = 0 \quad \text{and} \quad \frac{\partial h}{\partial \eta_2}(\vec{\eta})|_{\eta_2 = 0} = 0, \tag{3.82}$$

requires $k \geq 3$, whereas $k = 3$ for $p = 1$ (no trapping). Similar to property (3.70) we have

$$(h^{m-1}\nabla h + \vec{\eta}) \cdot \nabla h = 0 \quad \text{for} \quad \vec{\eta} \in \Gamma. \tag{3.83}$$

Since h is also invariant under a scaling similar to (3.52), it is possible to solve for this similarity solution in two dimensions and to obtain an analytical approximation of light oil removal in a three-dimensional situation.

Notation

A	position of oil free boundary in similarity profile
c_t	trapping constant
D	parameter determining finiteness of lens thickness
F	trapping function
g	gravity $[\mathrm{m\,s^{-2}}]$
$H_{j,i}$	phase j initial hydraulic head [m]
$h\,(\tilde{h})$	(scaled) similarity profile
K	absolute permeability $[\mathrm{m^2}]$
k	trapping parameter in similarity profile
k_{rj}	phase j relative permeability
$\bar{k}$	vertically integrated oil relative permeability
$M_1\,(\tilde{M}_1)$	(scaled) dimensionless first moment of free oil saturation per unit lateral area
$M_{k-1}\,(\tilde{M}_{k-1})$	(scaled) dimensionless time-independent moment of free oil saturation per unit lateral area
m	power in coefficient of diffusion equation
N	number of lateral dimensions
n	van Genuchten parameter
p	trapping constant in function F
$P_j\,(p_j)$	(dimensionless) phase j pressure [Pa]
$P_{jk}\,(p_{j,k})$	(dimensionless) phases j, k capillary pressure [Pa]
$P_{j,i}\,(p_{j,i})$	(dimensionless) phase j initial pressure [Pa]
P_{out}	outside pressure at seepage face [Pa]
q	dimensionless oil outflow rate
S_j	phase j saturation
S_{of}	free oil saturation
$S_{o,i}$	initial oil saturation
S_{ot}	trapped oil saturation
S_{or}^{max}	maximum residual oil saturation
S_t	total fluid saturation

S_{wa}	apparent water saturation
S_w^{min}	minimum water saturation
$T(t)$	(dimensionless) time [h]
T_c	characteristic time [h]
$T_e(t_e)$	(dimensionless) maximum computed time [h]
t_0	starting time of similarity solution
$\bar{t}$	time in similarity solution
$U_j(u_j)$	(dimensionless) phase j horizontal flow velocity [$\mathrm{m\,s^{-1}}$]
$V_j(v_j)$	phase j vertical flow velocity [$\mathrm{m\,s^{-1}}$]
$\mathcal{V}_0(v_0)$	(dimensionless) initial oil volume [$\mathrm{m^3}$]
υ	dimensionless oil volume
$\Delta\upsilon$	deviation of analytical from numerical solution
w_f	dimensionless free oil volume per unit lateral area
w_i	dimensionless initial oil volume per unit lateral area
w_m	dimensionless maximum oil volume per unit lateral area
w_t	(dimensionless) trapped oil volume per unit lateral area
$X(x)$	(dimensionless) horizontal coordinate [m]
X_c	characteristic horizontal length [m]
$X_l(x_l)$	(dimensionless) horizontal position of lens outer boundary [m]
$\tilde{y}$	scaled oil flux in similarity solution
$Z(z)$	(dimensionless) vertical coordinate [m]
Z_c	characteristic vertical length [m]
$Z_{ao}(z_{ao})$	(dimensionless) elevation beyond which air is present [m]
$Z_{ow}(z_{ow})$	(dimensionless) elevation beyond which oil is present [m]
$Z_u(z_u)$	(dimensionless) elevation beyond which no oil is present [m]
$Z_w(z_w)$	(dimensionless) elevation with zero water pressure [m]
α	van Genuchten parameter [$\mathrm{m^{-1}}$]
β_{ao},β_{ow}	ratios of air-oil and oil-water to air-water surface tensions
γ	dimensionless parameter in nonlinear diffusion equation
$\eta(\xi)$	(scaled) similarity variable
θ	maximum trapped oil saturation
λ_1,λ_2	constants in power law approximations of z_{ao} and $\bar{k}$
μ,ν	powers in similarity solution
μ_j	phase j viscosity [Pa s]
ρ_j	phase j density [$\mathrm{kg\,m^{-3}}$]
ϕ	porosity
χ	large number in 'iterative' seepage condition [$\mathrm{m^{-1}}$]

Chapter 4

Multi-phase flow modeling of air sparging

4.1 Introduction

A method for remediating an aquifer, which is contaminated by organic liquids (solvents, gasoline) trapped in the saturated zone, is to inject air or oxygen into the aquifer. Injection of air may enhance microbial degradation and volatilization.

For remediation of the unsaturated zone, gas venting has been studied both experimentally and numerically [20, 27, 33]. Besides the use of soil vapor extraction wells, injection of air at a small distance below the water table to remove contaminants at groundwater level has been considered [27].

For remediation of the saturated zone the use of a vacuum vaporizer well has been described [28]. Emphasis was laid on assessing the sphere of influence of the water circulation, where dissolved oxygen enhances microbial degradation.

Direct injection of air in the saturated zone, known as air sparging, together with vapor extraction in the unsaturated zone, has been put forward as an effective in-situ remediation technique. Air sparging has been studied experimentally on both field [12, 42] and laboratory [32, 61] scales in the last few years, with emphasis on the region in the saturated zone where air is present (radius of influence). A numerical study of air sparging at steady state has been provided for the case of injection just below the original water table [46].

Although laboratory experiments with air injection in a glass bead medium [32] showed that air flow can occur as isolated bubbles for bead diameters exceeding 2 mm, it is assumed that under natural subsurface conditions air flow is most likely to occur in small continuous channels [32, 34]. A recent field study for a uniform soil with mean grain size of 0.25 mm [41], indicated that the density of channels in the main region of air flow must be very high. Therefore, it is reasonable to model air flow macroscopically as a continuum.

Air sparging is only possible in relatively coarse-grained soils. The reported injection rates varied from about 3 m^3/hr up to 100 m^3/hr for thick sandy-gravelly deposits [12, 34]. Injection in fine textured soils requires high air entry pressures, which may cause fracturing of the soil. This may result in the formation of a few channels through which air flows upwards [42]. Hence, knowledge of soil layering and heterogeneity is important because these affect the radius of influence [34].

Besides flow continuity air phase compressibility may be a complicating factor in modeling air sparging. In the early stage of sparging when air pathways from the injection filter to the unsaturated zone have not yet been established, air density is not constant. However, emphasizing the steady state situation in which continuous channels to the vadose zone exist, compressibility is expected to play a minor role. This expectation is supported by the field study [41], which describes sparging at a rate of 34.2 m^3/hr, resulting into a pressure increase of 10.5 kPa at a distance of 0.6 m from the filter. This causes an air density increase of about 10 % only.

Important for dimensioning the technique of air sparging is quantitative knowledge of the effect of soil, fluid and filter parameters on the radius of influence of an injection filter. This motivated us to study an axially symmetric model for air injection through a vertically positioned filter in an initially saturated region below the vadose zone. In the model we consider air and water as two immiscible incompressible continuous phases. The interaction between the fluid phases and the soil matrix is described by the saturation dependent relative permeability and capillary pressure functions. Contaminants are assumed to be part of the soil matrix and do not affect the flow process.

The basic equations are given and discussed in Section 4.2, where they are reformulated in terms of dimensionless numbers (that are combinations of the physical parameters). In Section 4.3 we discuss a numerical method, which is based on the mixed form of the Richards equation for both water and air. Results of numerical computations are presented in terms of the distribution of air saturations and the volume of air that is stored in the domain. In Section 4.4 we discuss two analytical approximations which are valid in the relevant part of the flow domain. One is an upper bound that explains the occurrence of small saturations. The other is an explicit solution for the steady state situation, which is derived under the assumptions that water is immobile and that gravity is the dominant effect in the vertical direction. The explicit solution provides an expression for the radius of influence of sparging. In Section 4.5 we quantify the agreement between the analytical and numerical solutions at steady state.

4.2 Model

We use Darcy's Law for both air (a) and water (w)

$$\vec{U}_j = -\frac{K_{\mathrm{abs}}\, k_{rj}}{\mu_j}\, \nabla\, (P_j + \rho_j\, g\, Z), \quad j = w, a \tag{4.1}$$

and the mass balance equations

$$\phi\,\frac{\partial\, S_j}{\partial\, t} + \nabla\cdot\vec{U}_j = 0, \quad j = w, a. \tag{4.2}$$

In Equation (4.2) S_j denotes the effective fluid saturation and ϕ the effective porosity, i.e. redefined according to

$$S_w := \frac{S_w - S_r}{1 - S_r}, \quad S_a := \frac{S_a}{1 - S_r}, \quad \phi := (1 - S_r)\,\phi,$$

where S_r is the residual water saturation. Furthermore, K_{abs} is soil absolute permeability, ϕ soil porosity, $\vec{U}_j$ fluid Darcy velocity, S_j fluid saturation, k_{rj} fluid relative permeability, μ_j fluid viscosity, P_j fluid pressure, ρ_j fluid density and g gravity. We assume that the soil is homogeneous and isotropic and that both fluids are incompressible.

The set of equations (4.1) and (4.2) is completed by the constitutive relations $S_w + S_a = 1$, the capillary pressure $P_c = P_a - P_w$, $S_j = S_j(P_c)$ and $k_{rj} = k_{rj}(S_j)$ and is solved for the unknowns S_w, S_a, P_w, P_a, $\vec{U}_w$ and $\vec{U}_a$. The dependence of capillary pressure and relative permeability on the saturations is given by the well-known expressions [47]

$$P_c(S_w) = \frac{\rho_w\, g}{\alpha}\left(S_w^{-\frac{1}{m}} - 1\right)^{1-m} \tag{4.3}$$

$$k_{rw}(S_w) = S_w^{\frac{1}{2}}\left(1 - (1 - S_w^{\frac{1}{m}})^m\right)^2 \tag{4.4}$$

$$k_{ra}(S_a) = S_a^{\frac{1}{2}}\left(1 - (1 - S_a)^{\frac{1}{m}}\right)^{2m}, \tag{4.5}$$

where $0 < m < 1$ and $\alpha > 0$ are given constants. Note that $S_w(P_c)$ is defined for $P_c \geq 0$. For $P_c < 0$ we set $S_w = S_w(0) = 1$. Hence, $0 \leq S_w \leq 1$ for all values of P_c [35, 47].

Equations (4.1) and (4.2) are solved in the two-dimensional axially symmetric domain of Figure 4.1. The level $Z = 0$ corresponds to the initial position of the water table, where $P_w = 0$. Along the top boundary of the domain, $Z = H_t$, the air pressure equals $P_a = 0$. The water pressure along this
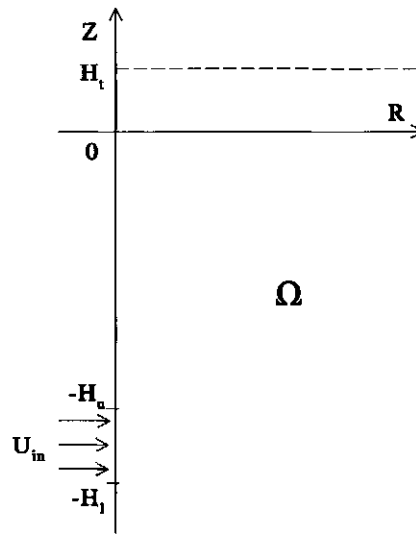
Figure 4.1: Schematic of the domain (Ω) for air sparging.

boundary is selected such that the water table is situated at $Z = 0$. Hence,

$$P_j \;=\; P_{jt} \quad \text{for } R > E,\ Z = H_t, \tag{4.6}$$

for $j = w, a$, where $P_{wt} = -\rho_w\, g\, H_t$ and $P_{at} = 0$. Air is injected with velocity U_{in} into this domain through a filter with radius $E > 0$ and length $H_l - H_u$, giving the total injection rate $Q = 2\,\pi\, E\,(H_l - H_u)\, U_{\text{in}}$. Writing $\vec{U}_j = (U_{j,r}, U_{j,z})$, we have the flux boundary conditions

$$
\left.
\begin{aligned}
U_{w,r} &= 0 \\
U_{a,r} &= U_{\text{in}}
\end{aligned}
\right\}
\quad \text{for } R = E,\ -H_l < Z < -H_u
$$
$$
U_{j,r} = 0 \qquad \text{for } R = E,\ Z < -H_l,\ -H_u < Z < H_t. \tag{4.7}
$$

The initial conditions at $T = 0$, say, are

$$P_j \;=\; P_{jt} + \rho_j\, g\,(H_t - Z) \quad \text{for } r > E,\ Z < H_t. \tag{4.8}$$

We introduce the dimensionless variables

$$
\begin{aligned}
t &= \frac{T\, U_{\text{in}}}{\phi\, H}, \quad r = \frac{R}{H}, \quad z = \frac{Z}{H}, \\[2mm]
\vec{u}_j &= \frac{\vec{U}_j}{U_{\text{in}}}, \quad p_j = \frac{\alpha\, P_j}{\rho_w\, g}, \qquad\qquad j = w, a
\end{aligned}
\tag{4.9}
$$

where $H = \frac{H_u + H_l}{2}$, the depth of the filter center, is chosen as a characteristic length. Furthermore, we define the dimensionless constants

$$\varepsilon = \frac{E}{H}, \quad h_u = \frac{H_u}{H}, \quad h_l = \frac{H_l}{H}, \quad h_t = \frac{H_t}{H}, \quad p_{jt} = \frac{\alpha\, P_{jt}}{\rho_w\, g}.$$

The flow problem is now determined by the the mobility ratio, the gravity numbers for water and air, the capillary number and the dimensionless filter surface, i.e.,

$$M = \frac{\mu_w}{\mu_a}, \quad N_{jg} = \frac{K_{\text{abs}}\, \rho_j\, g}{\mu_a\, U_{\text{in}}}, \quad N_c = \frac{K_{\text{abs}}\, \rho_w\, g}{\mu_a\, U_{\text{in}}\, H\, \alpha}, \quad A = \frac{Q}{U_{\text{in}}\, H^2}. \tag{4.10}$$

For both water and air, equations (4.1) and (4.2) are combined into the mixed form of the Richards equation [13, 35]. Together with the boundary and initial conditions the resulting problem is:

$$
\begin{cases}
\begin{aligned}
\dfrac{\partial S_w}{\partial t} &= \nabla \cdot \left(k_{rw} \nabla \left(\dfrac{N_c}{M} p_w + \dfrac{N_{wg}}{M} z \right) \right) \\
\dfrac{\partial S_a}{\partial t} &= \nabla \cdot \left(k_{ra} \nabla \left(N_c p_a + N_{ag} z \right) \right)
\end{aligned}
\left.\vphantom{\dfrac{\partial S_w}{\partial t}}\right\} \quad \text{in } r > \varepsilon, \ z < h_t, \ t > 0 \\[2ex]
\left.
\begin{aligned}
u_{w,r} &= 0 \\
u_{a,r} &= 1
\end{aligned}
\right\} \qquad\qquad\qquad\quad \text{for } r = \varepsilon, \ -h_l < z < -h_u, \qquad\quad t > 0 \\[2ex]
u_{j,r} = 0 \qquad\qquad\qquad\quad \text{for } r = \varepsilon, \ z < -h_l, \ -h_u < z < h_t, \quad t > 0 \\[1ex]
p_j = p_{jt} \qquad\qquad\qquad\quad \text{for } r > \varepsilon, \ z = h_t, \qquad\qquad\qquad t > 0 \\[1ex]
p_j = p_{jt} + \dfrac{N_{jg}}{N_c}\,(h_t - z) \quad \text{for } r > \varepsilon, \ z < h_t, \qquad\qquad\quad t = 0,
\end{cases}
\tag{4.11}
$$

where $p_{wt} = -\dfrac{N_{wg}}{N_c}\, h_t$ and $p_{at} = 0$. The dimensionless capillary pressure, which depends now on S_a, is, according to the redefinition of the phase pressures,

$$p_c(S_a) = \left((1 - S_a)^{-\frac{1}{m}} - 1 \right)^{1-m}, \tag{4.12}$$

with $S_a = 0$ for $p_c < 0$. Problem (4.11) is solved for one of the phase saturations and one of the phase pressures. In general, however, it cannot be solved explicitly due to the nonlinear nature of the equations.

To develop an understanding of the behavior of the solution, we consider a numerical solution technique based on the formulation of Problem (4.11). In addition, we characterize some aspects of the solutions analytically. To achieve this we construct a single equation for the air saturation only. We find

in terms of S_a [9, 14] :

$$\begin{cases} \dfrac{\partial S_a}{\partial t} + \nabla \cdot \vec{u}_a = 0 \\[3mm] \vec{u}_a = f_a \, \vec{u}_t + N_g \, \lambda \, \vec{e}_z - N_c \, \lambda \, \nabla p_c, \end{cases} \qquad (4.13)$$

where

$$f_a = \frac{M \, k_{ra}}{k_{rw} + M \, k_{ra}} \qquad (4.14)$$

denotes the air fractional flow function and

$$\lambda = \frac{k_{rw} \, k_{ra}}{k_{rw} + M \, k_{ra}} \qquad (4.15)$$

denotes the mobility function. $N_g = N_{wg} - N_{ag}$ and $\vec{e}_z$ is the unit vector in the z-direction. Further, $\vec{u}_t = \vec{u}_w + \vec{u}_a$ denotes the total velocity, which satisfies the incompressibility condition

$$\nabla \cdot \vec{u}_t = 0. \qquad (4.16)$$

Observe that in case gravitational and capillary effects are neglected, the air velocity $\vec{u}_a$ is the fraction f_a of the total velocity.

Setting $S = S_a$ we arrive at the initial-boundary value problem

$$\begin{cases} \left. \begin{array}{l} \dfrac{\partial S}{\partial t} + \nabla \cdot (f_a \, \vec{u}_t + N_g \, \lambda \, \vec{e}_z - N_c \, \lambda \, \nabla p_c) = 0 \\[2mm] \nabla \cdot \vec{u}_t = 0 \end{array} \right\} \\[6mm] \qquad\qquad\qquad\qquad\qquad \text{for } r > \varepsilon, \ z < h_t, \qquad\qquad\qquad t > 0 \\[4mm] \left. \begin{array}{rcl} f_a - N_c \, \lambda \, \dfrac{\partial p_c}{\partial r} &=& 1 \\[2mm] u_{t,r} &=& 1 \end{array} \right\} \quad \text{for } r = \varepsilon, \ -h_l < z < -h_u, \qquad t > 0 \\[4mm] \begin{array}{rcl} \dfrac{\partial S}{\partial r} &=& 0 \\[2mm] u_{t,r} &=& 0 \end{array} \qquad\qquad\ \text{for } r = \varepsilon, \ z < -h_l, \ -h_u < z < h_t, \ \ t > 0 \\[4mm] \begin{array}{rcl} p_c &=& p_t \end{array} \qquad\qquad\quad\ \text{for } r > \varepsilon, \ z = h_t, \qquad\qquad\qquad t > 0 \\[4mm] \begin{array}{rcl} p_c &=& p_t - \dfrac{N_g}{N_c} \, (h_t - z) \end{array} \quad \text{for } r > \varepsilon, \ z < h_t, \qquad\qquad t = 0, \end{cases}$$
$$(4.17)$$

where $p_t = p_{at} - p_{wt} = \dfrac{N_{wg}}{N_c} \, h_t = \alpha \, H \, h_t$. Note that this problem is equivalent to the original description (4.11) in terms of the separate phase saturations and pressures. However, to understand the qualitative behavior of the solution, one often considers $\vec{u}_t$ in (4.17) as given, leading to a nonlinear advection-diffusion equation in terms of S only, which is more accessible to analysis.

In Problem (4.17) $f_a(S)$, $\lambda(S)$ and $p_c(S)$ are nonlinear functions of S. These nonlinearities are grouped in the functions

$$\vec{F}(S, \vec{u}_t) = f_a(S)\,\vec{u}_t + N_g\,\lambda(S)\,\vec{e}_z, \quad D(S) = N_c\,\lambda(S)\,\frac{d\,p_c}{d\,S}(S). \quad (4.18)$$

In Figure 4.2 we show some typical examples of (4.18). We note here that the r-component of the flux F_r is increasing in S for all $u_{t,r} > 0$. The z-component F_z, however, need not be monotone in S [54]. This only occurs if $\dfrac{N_g}{u_{t,z}} > 1$. Under this condition we find a unique value S_t, the threshold saturation, for which F_z satisfies

$$F_z(S_t, u_{t,z}) = F_z(1, u_{t,z}) = u_{t,z}, \quad (4.19)$$

and

$$F_z(S, u_{t,z}) > F_z(1, u_{t,z}), \quad \text{for } S_t < S < 1. \quad (4.20)$$

One easily verifies that (4.19) is equivalent to

$$k_{r,a}(S_t) = \frac{u_{t,z}}{N_g}. \quad (4.21)$$

The formulation of Problem (4.17) shows that the two-phase flow process is determined by the dimensionless numbers M, N_g, N_c, and A, and by the exponent m in the nonlinearities.

4.3 Numerical solution

Using a numerical two-phase flow model we solve Problem (4.11) on the finite domain $E < R < R_b$ and $-H_b < Z < H_t$ ($H_b > H_l$). Hence, we impose also conditions at the lower (no-flow) and right (hydrostatic pressure) boundaries

$$
\begin{aligned}
U_{j,z} &= 0 & &\text{for } E < R < R_b,\ Z = -H_b \\
P_j &= P_{jt} + \frac{N_{jg}}{N_c}\,(H_t - Z) & &\text{for } R = R_b,\ -H_b < Z < H_t.
\end{aligned}
\quad (4.22)
$$

Numerical computations are done in non-transformed physical variables.

The flow domain is discretized by linear triangular finite elements and the time discretization is fully implicit. The resulting algebraic equations are solved by the modified Picard method [13], giving good mass balance. In R-direction, the grid is finest close to the Z-axis (19 nodes in total, the width of an element is 1.08 times the width of the previous element),whereas the grid size is constant in Z-direction (3 nodes per meter). Convergence is obtained
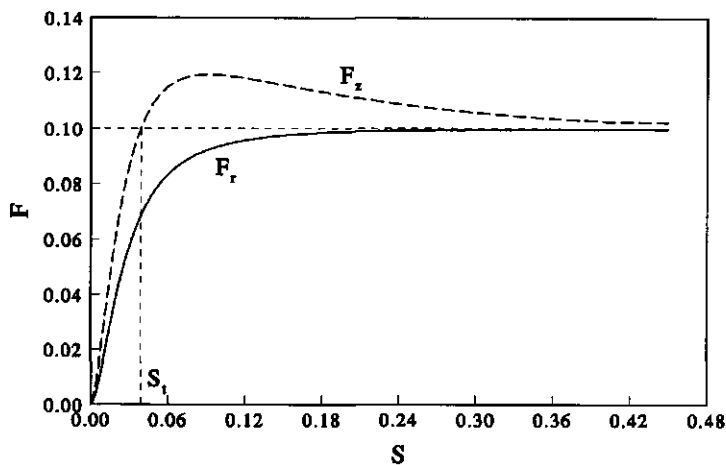
(a)
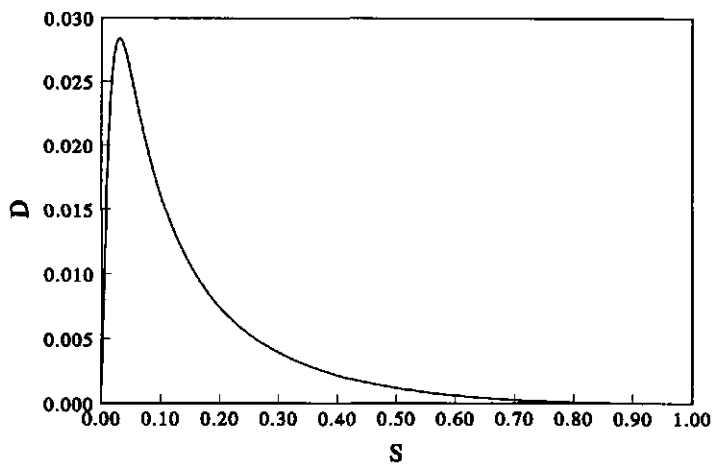
(b)

Figure 4.2: Graphs of (a) the radial component F_r of $\vec{F}$ for $u_{t,r} = 0.1$ and the vertical component F_z for $u_{t,z} = 0.1$, and of (b) D ($M = 73.4$, $N_g = 6.64$, $N_c = 1.48$ and $m = 0.500$).

for the Picard iterations by adjusting the time steps. For the hydraulic head for each phase j at nodal point i,

$$\varphi_{ji} = \frac{P_{ji}}{\rho_w\, g} + \frac{\rho_j}{\rho_w}\, Z_i,$$

we require that

$$\max_{j,i} \left| \frac{\varphi_{ji}^{k+1,n+1} - \varphi_{ji}^{k+1,n}}{\varphi_{ji}^{k+1,n+1}} \right| \leq e_c$$

is reached within 20 Picard iterations. Here k refers to time and n to the Picard iteration level. Due to large differences in density and viscosity between air and water, the flow problem is dominated by advection. This requires relatively small time steps to reach convergence in 20 iterations, and hence large computation times. The initial time step is 0.03 seconds and the maximum allowable time step is 15 seconds. For all computations we use the relative convergence error $e_c = 0.001$.

The following soil and fluid parameters are fixed during all computations:

$$
\begin{array}{llll}
K_{\mathrm{abs}} & = 5.30 \cdot 10^{-11}\ \mathrm{m}^2, & \phi & = 0.390, \\
\mu_a & = 1.77 \cdot 10^{-5}\ \mathrm{Pa\,s}, & \rho_a & = 1.24 \quad\ \ \mathrm{kg\,m}^{-3}, \\
\mu_w & = 1.30 \cdot 10^{-3}\ \mathrm{Pa\,s}, & \rho_w & = 1.00 \cdot 10^3\ \mathrm{kg\,m}^{-3}, \\
g & = 9.8 \quad\qquad\ \ \mathrm{m\,s}^{-2}. &&
\end{array}
$$

The effective porosity $\phi = 0.390$ reflects a soil porosity of 0.400 and a residual water content of 0.010. Parameters involving the boundary conditions are:

$$
\begin{array}{llll}
E & = 5.00 \cdot 10^{-2} \quad \mathrm{m}, & R_b & = 3.65\ \ \mathrm{m}, \\
H_t & = 1.50 \qquad\quad\ \mathrm{m}, & H_l - H_u & = 1.00\ \ \mathrm{m}, \\
P_{wt} & = -1.47 \cdot 10^4\ \ \mathrm{Pa}, & P_{at} & = 0.0 \quad \mathrm{Pa},
\end{array}
$$

whereas H_b is adjusted for each computation, such that the lower boundary does not affect the air flow.

The van Genuchten parameters α and m, the air injection velocity U_{in} and the filter depth H are varied, which implies the variation of the exponent m and the dimensionless numbers N_g, N_c and A. The mobility ratio $M = 73.4$ is kept constant. In Table 4.1 the data for the reference case (case 1) and for the other cases are summarized. Observe that in the reference case, the total injection rate $Q = 5.00\ \mathrm{m}^3\,\mathrm{hr}^{-1}$.

All results are presented in terms of the dimensionless variables (4.9). Typical contourplots of the air saturations for the reference case are shown in Figure 4.3.
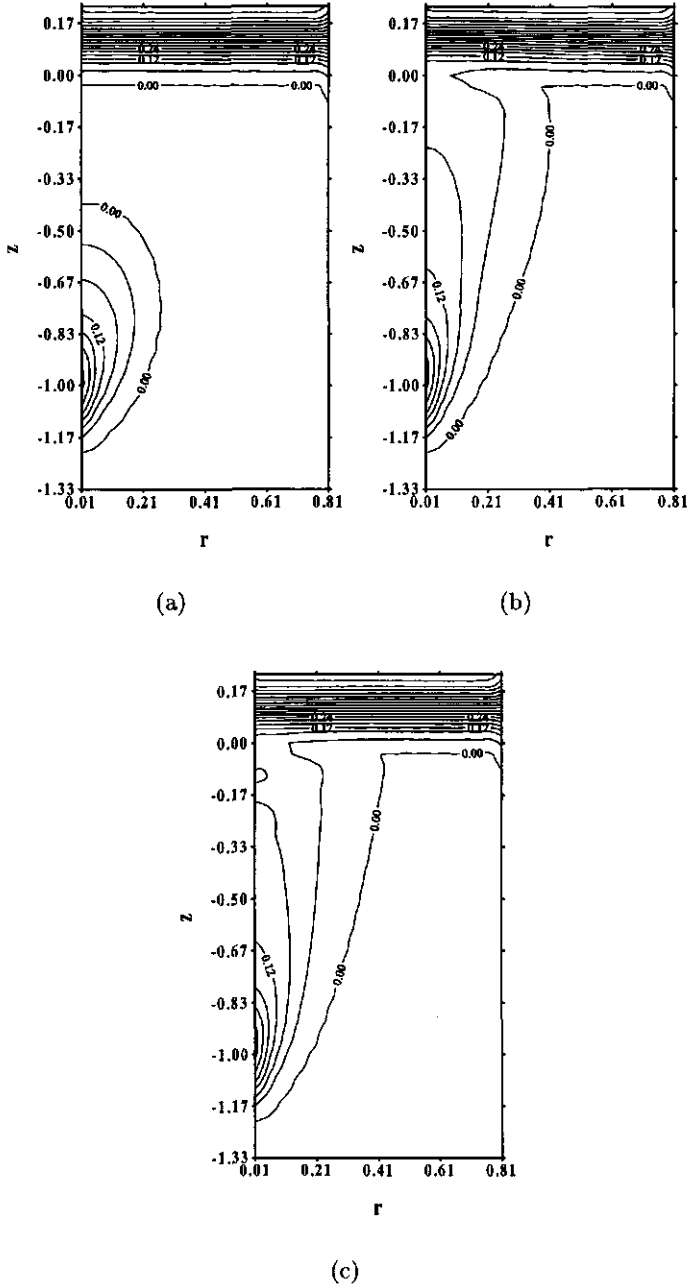
(a)

(b)

(c)

Figure 4.3: Air saturation contourplots at (a) $t = 0.302$, (b) $t = 1.21$ and (c) $t = 15.1$ (case 1).

Table 4.1: Parameters and dimensionless numbers used in computations. Relative to the reference case (case 1), m is varied for cases 2-5, N_g for cases 6-9, N_c for cases 10-13 and A for cases 14-17.

case	α m^{-1}	U_{in} $10^{-3}\,\mathrm{m\,s}^{-1}$	H m	m	N_g	N_c 10^{-3}	A
1	2.00	4.42	4.50	0.667	6.63	0.738	15.5
2	2.00	4.42	4.50	0.400	6.63	0.738	15.5
3	2.00	4.42	4.50	0.500	6.63	0.738	15.5
4	2.00	4.42	4.50	0.750	6.63	0.738	15.5
5	2.00	4.42	4.50	0.800	6.63	0.738	15.5
6	0.800	11.1	4.50	0.667	2.675	0.738	15.5
7	1.00	8.84	4.50	0.667	3.32	0.738	15.5
8	1.50	5.90	4.50	0.667	4.97	0.738	15.5
9	3.00	2.95	4.50	0.667	9.95	0.738	15.5
10	2.50	4.42	4.50	0.667	6.63	0.590	15.5
11	1.67	4.42	4.50	0.667	6.63	0.885	15.5
12	1.00	4.42	4.50	0.667	6.63	1.48	15.5
13	0.500	4.42	4.50	0.667	6.63	2.95	15.5
14	1.20	4.42	7.50	0.667	6.63	0.738	5.59
15	1.46	4.42	6.17	0.667	6.63	0.738	8.26
16	1.64	4.42	5.50	0.667	6.63	0.738	10.4
17	2.57	4.42	3.50	0.667	6.63	0.738	25.6

The time dependence is illustrated by showing the increase of the volume of air that is stored in the domain:

$$V(t) = 2\,\pi \int_{-h_b}^{h_t} \int_{\varepsilon}^{r_b} r\, S(r,z,t)\, dr\, dz - 2\,\pi \int_{-h_b}^{h_t} \int_{\varepsilon}^{r_b} r\, S(r,z,0)\, dr\, dz, \quad (4.23)$$

where $r_b = \dfrac{R_b}{H}$. In Figure 4.4, $V(t)$ is shown for cases 1, 3, 10 and 14. For some cases oscillations occur, which are caused by physical instabilities. When injected air reaches the water table an amount of stored air leaves the flow domain through the unsaturated zone, which takes place much faster than the injection of air. Hence, the stored air volume decreases. This process can occur several times. Note, however, that the resolution of the calculations can also affect the extent of oscillation.

The plots in Figure 4.4 show that a steady situation is reached before $t = 20$ for all cases considered. This is equivalent to about 2 hours in real time. To characterize the numerical results, we show in Figure 4.5 for the reference case a cross-section of the saturation profile at $z = -0.2$ at steady state. For a time $t_1 > 20$, we determine the saturation $S_\varepsilon = S(\varepsilon, -0.2, t_1)$ and the radial position r_1 for which $S(r_1, -0.2, t_1) = \dfrac{1}{2}\, S_\varepsilon$. Both S_ε and r_1
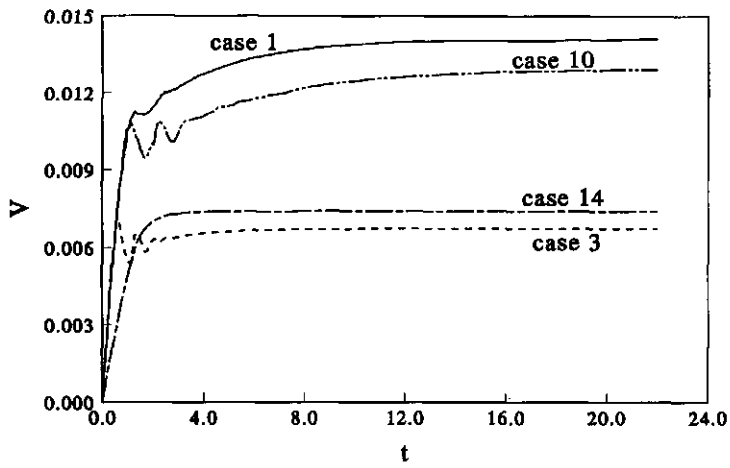
Figure 4.4: Air volume stored in the flow domain (cases 1, 3, 10 and 14).
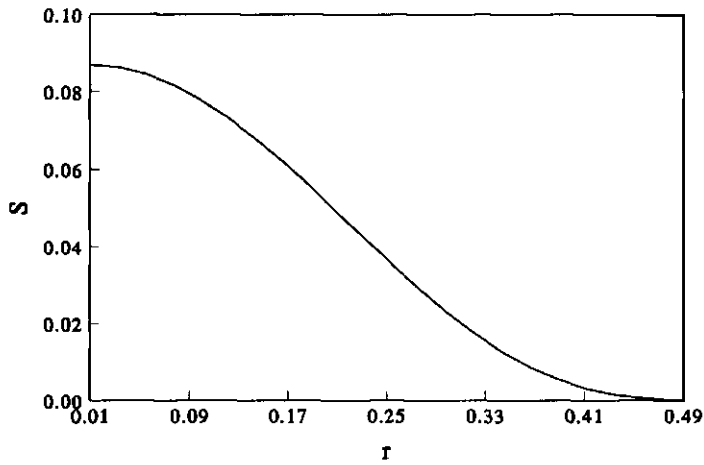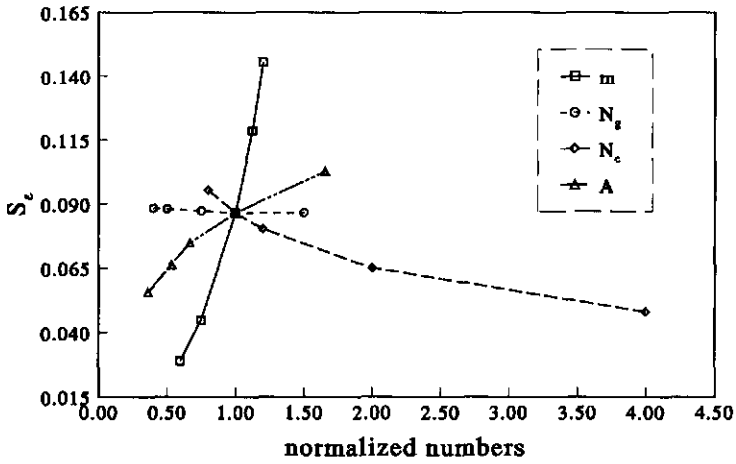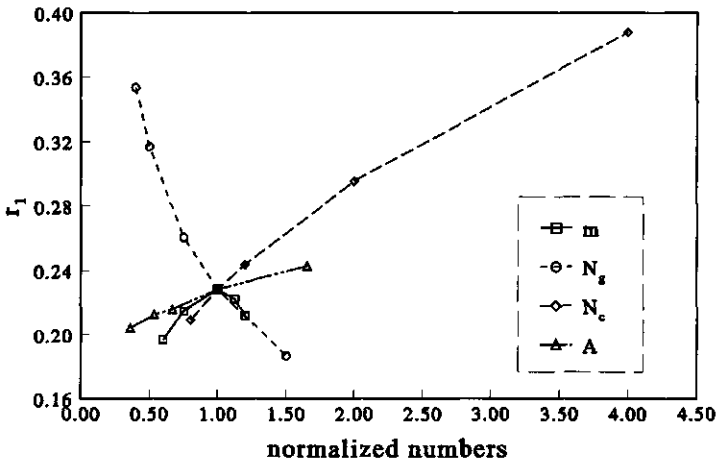

Figure 4.5: Cross-section of the air saturation profile at $z = -0.2$ (case 1).

(a)

(b)

Figure 4.6: Dependence of (a) the maximum saturation S_ε and (b) the radial position r_1 on the dimensionless numbers. For instance, the m-curve reflects values of the parameters for cases 2-5, see Table 4.1.
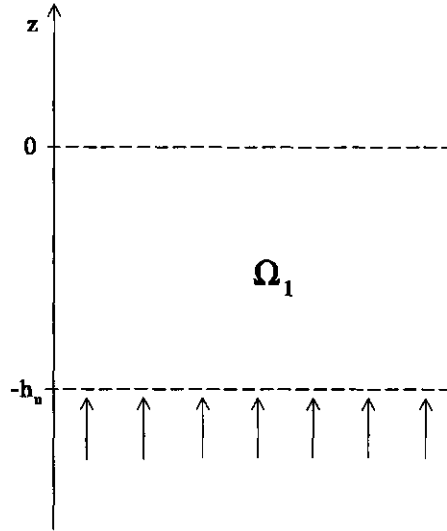
Figure 4.7: Schematic of the domain (Ω_1) for air injection through a horizontal disk.

are shown in Figure 4.6 as a function of the dimensionless numbers, which are normalized with respect to the reference case, indicated by the subscript 1 :

$$m_n = \frac{m}{m_1}, \quad N_{gn} = \frac{N_g}{N_{g1}}, \quad N_{cn} = \frac{N_c}{N_{c1}}, \quad A_n = \frac{A}{A_1}. \qquad (4.24)$$

From the numerical results we conclude that the air saturation is much less than one in the entire flow domain and that the water pressure is almost hydrostatic at large times. This allows us to treat the steady state air flow as a single-phase process.

4.4 Bounds and approximations

4.4.1 One-dimensional flow

To explain the small values of the air saturation in the flow domain, we consider a relatively simple auxiliary problem involving an air saturation, which is above the saturation of Problem (4.17). For this auxiliary problem we assume, as in Figure 4.7, that air is injected through a horizontal disk at $z = -h_u$ with a uniform rate $u_{a,z} = 1$. This leads to a much higher flow rate at $z = -h_u$ than in case of injection through the vertical filter. At $z = 0$ we impose the natural outflow condition $\dfrac{\partial S}{\partial z} = 0$. Consequently, the air saturation in this simplified

case serves as an upper bound for the air saturation in case of injection through a vertical filter.

The injection through the horizontal disk leads to a one-dimensional analog of Problem (4.17), for $-h_u < z < 0$ in which $u_{t,z} \equiv 1$. We therefore consider the problem

$$
\begin{cases}
\dfrac{\partial S}{\partial t} + \dfrac{\partial}{\partial z}\left(F(S) - D(S)\dfrac{\partial S}{\partial z}\right) = 0 & \text{in } -h_u < z < 0, \quad t > 0 \\[2mm]
F(S) - D(S)\dfrac{\partial S}{\partial z} = 1 & \text{for } z = -h_u, \quad t > 0 \\[2mm]
\dfrac{\partial S}{\partial z} = 0 & \text{for } z = 0, \quad t > 0 \\[2mm]
S = 0 & \text{for } -h_u < z < 0, \quad t = 0,
\end{cases}
\tag{4.25}
$$

where the boundary condition at $z = -h_u$, with $F(S) = F_z(S, u_{t,z} = 1)$, ensures the injection of air only. Note that F is non-monotone if $N_g > 1$, see (4.20). We show below that the saturation of the auxiliary Problem (4.25) is below the threshold saturation S_t, see (4.19).

By an elementary argument based on the maximum principle [55], one finds that a solution of Problem (4.25) attains its maximum value at $z = -h_u$, with $\dfrac{\partial S}{\partial z} < 0$. This statement can also be obtained on physical grounds, when remembering that Problem (4.25) describes injection of air from the bottom into a medium which is completely filled with water at $t = 0$. To assess the maximum value, denoted by S_m, we find from the boundary condition at $z = -h_u$

$$
F(S_m) = 1 + D(S_m)\frac{\partial S}{\partial z} < 1,
$$

implying $S_m < S_t$. Hence, we have shown

$$
S(z, t) < S_t, \quad \text{for } -h_u \leq z \leq 0, \quad t \geq 0.
\tag{4.26}
$$

To check the validity of this upper bound we also make a comparison with the numerical solution. To this end we compare the saturation just above the injection filter, $S_{\max} = S(\varepsilon, -h_u, t)$, with the threshold value S_t for $u_{t,z} = 1$ and for all values of the parameters in a relevant range. For example, Figure (4.8) shows S_t as a function of m and N_g, as S_t appears to depend on these numbers, see (4.21). The saturation just above the filter is chosen because it appears to be stationary and maximum on the flow domain.

4.4.2 Steady state flow

At steady state the time derivative in the saturation equation in Problem (4.17) vanishes. The reduced equation must be solved subject to the same bound-
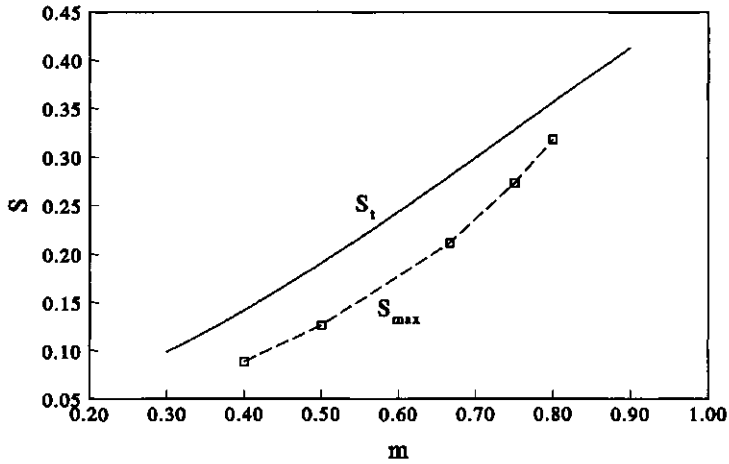
(a)
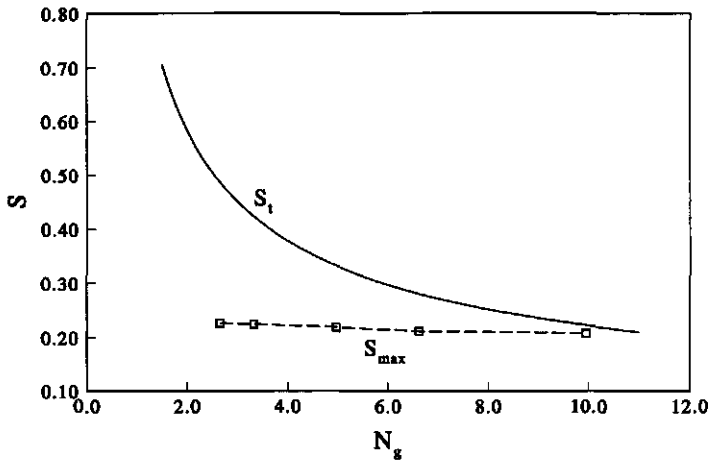
(b)

Figure 4.8: Comparison of S_t for $u_{t,z} = 1$ and $S_{\max}$ as a function of (a) the exponent m and (b) the gravity number N_g. The m-curve reflects values of the parameters for cases 2-5 and the N_g-curve for cases 6-9 of Table 4.1.

ary conditions. Inherited from the initial pressure distribution we impose in addition

$$p_c \to p_t - \frac{N_g}{N_c}(h_t - z) \quad \text{for} \quad \begin{array}{l} r \to \infty, \ z < h_t \\ r > \varepsilon, \ z \to -\infty. \end{array} \tag{4.27}$$

The numerical results show that the water pressure is approximately hydrostatic at large times. This implies that the water velocity can be disregarded with respect to the air velocity, i.e. $\vec{u}_t = \vec{u}_a$. Using this in Problem (4.13) yields for the air velocity

$$\vec{u}_a = N_g \, k_{ra} \, \vec{e}_z - N_c \, k_{ra} \, \nabla p_c. \tag{4.28}$$

Consequently, we obtain in terms of the air saturation the approximate problem:

$$\begin{cases} \nabla \cdot k_{ra}(N_g \, \vec{e}_z - N_c \, \nabla p_c) = 0 & \text{in } r > \varepsilon, \ z < h_t \\[2mm] -N_c \, k_{ra} \, \dfrac{\partial p_c}{\partial r} = 1 & \text{for } r = \varepsilon, \ -h_l < z < -h_u \\[2mm] \dfrac{\partial S}{\partial r} = 0 & \text{for } r = \varepsilon, \ z < -h_l, \ -h_u < z < h_t \\[2mm] p_c = p_t & \text{for } r > \varepsilon, \ z = h_t \\[2mm] p_c \to p_t - \dfrac{N_g}{N_c}(h_t - z) & \text{for } \begin{array}{l} r \to \infty, \ z < h_t \\ r > \varepsilon, \ z \to -\infty. \end{array} \end{cases} \tag{4.29}$$

In view of the large difference between the densities of air and water we assume that upwards from the injection filter and below the water table, flow in the z-direction is dominated by advection, i.e.,

$$\left| N_g \, \frac{\partial k_{ra}}{\partial z} \right| \gg \left| N_c \, \frac{\partial}{\partial z}(k_{ra} \, \frac{\partial p_c}{\partial z}) \right|. \tag{4.30}$$

As a consequence we are left with a nonlinear diffusion equation in the variables r and z. When solving this equation, no boundary condition can be imposed at $z = h_t$, representing a 'future time'. Hence, we consider the flow domain above the well of infinite extent, represented by $z > -h_u$. Interpreting solutions only up to $z = 0$ will produce a reasonable approximation in this region. Assuming furthermore that the well-radius $\varepsilon \ll 1$, we arrive at the problem, setting $k(r, z) = k_{ra}(S(r, z))$:

$$\begin{cases} N_1 \, \dfrac{\partial k}{\partial z} = \dfrac{1}{r} \, \dfrac{\partial}{\partial r}\left(r \, \bar{D}(k) \, \dfrac{\partial k}{\partial r} \right) & \text{in } r > 0, \ z > -h_u \\[2mm] \dfrac{\partial k}{\partial r}(0, z) = 0 & \text{for } z > -h_u \\[2mm] k(\infty, z) = 0 & \text{for } z > -h_u, \end{cases} \tag{4.31}$$
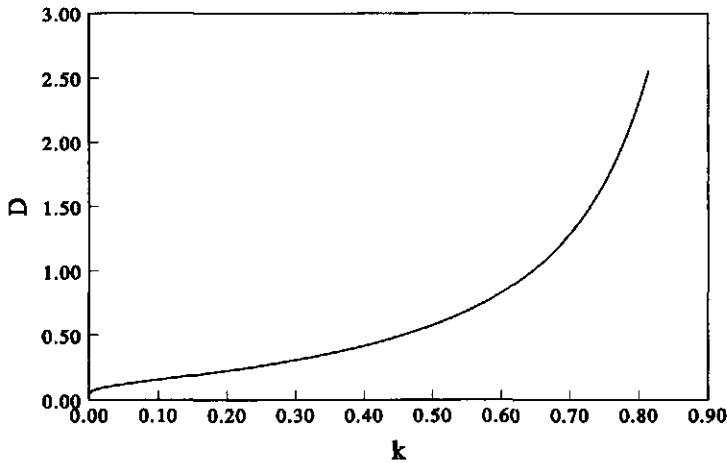
Figure 4.9: Graph of $\bar{D}(k)$ with m=0.750.

where $N_1 = \dfrac{N_g}{N_c}$ and $\bar{D}(k) = k\,\dfrac{d\,p_c}{d\,k}\,(k)$. In Figure 4.9 we show an example of $\bar{D}(k)$.

At $z = -h_u$ we need to impose an 'initial condition', which should reflect the influence of the injection filter. First, we observe by a straightforward continuity argument that

$$2\pi \int_0^\infty r\,u_{a,z}\,dr \;=\; A \quad \text{for all } z \geq -h_u. \tag{4.32}$$

Using the approximation implied by (4.30), this can be rewritten in terms of k :

$$\int_0^\infty r\,k(r,z)\,dr \;=\; \frac{N_2}{2} \quad \text{for all } z \geq -h_u, \tag{4.33}$$

where $N_2 = \dfrac{A}{\pi\,N_g}$. For computational purposes we assume that the injection of air only takes place at the center point of the filter, i.e. $r = 0$, $z = -1$. This leads us to consider (4.31) and (4.33) for all $z > -1$, subject to the 'initial condition'

$$k(r,-1) = 0 \qquad \text{for all } r > 0. \tag{4.34}$$

In other words, the injection of air is described by a delta-distribution at the point $r = 0$, $z = -1$.

Only for special diffusion coefficients $\bar{D}(k)$ Problem (4.31) admits an explicit solution. For example when $\bar{D}$ is a power law function a solution is known

in terms of similarity variables. This solution is known as the Barenblatt-Pattle point source solution [5, 50]. As a result of the upper bound derived in the previous section, we may conclude that k is small throughout the flow domain. We use this observation to approximate $\bar{D}(k)$ by a power law function, see Appendix 4A:

$$\bar{D}(k) \sim n_D \, k^{p_D}, \tag{4.35}$$

where

$$
\begin{aligned}
n_D &= \frac{2\,(1-m)}{4\,m+1}\, m^{\frac{m-1}{4m+1}}, & n_D &> 0, \\
p_D &= \frac{2\,(1-m)}{4\,m+1}, & 0 &< p_D < 2.
\end{aligned}
\tag{4.36}
$$

Note that in most cases of practical interest $p_D < 1$.

Hence, following [5, 50] we find that for sufficiently small k the solution of Problem (4.31) with the conditions (4.33) and (4.34) can be approximated by

$$
k(r,z) = \begin{cases}
\dfrac{p_D+1}{p_D}\,\dfrac{N_2}{f^2(z)}\left(1-\dfrac{r^2}{f^2(z)}\right)^{\frac{1}{p_D}} & \text{for } 0 \le r \le f(z), \quad z > -1 \\[2ex]
0 & \text{for } r > f(z), \quad\quad z > -1,
\end{cases}
\tag{4.37}
$$

where

$$f(z) = f_0 \cdot (z+1)^{\frac{1}{2(p_D+1)}} \quad \text{for } z \ge -1 \tag{4.38}$$

and

$$f_0 = \left(\frac{4\,n_D}{N_1}\,N_2^{p_D}\right)^{\frac{1}{2(p_D+1)}}\left(\frac{p_D+1}{p_D}\right)^{\frac{1}{2}}. \tag{4.39}$$

Observe that the function $f(z)$ represents the interface that separates the region where $k, S > 0$ from the region where $k, S = 0$. In the mathematical jargon the set $\{(f(z), z)\,;\, z \ge -1\}$ is known as the free boundary of Problem (4.31). Strictly speaking, the Barenblatt-Pattle solution (4.37) is valid for all $z > -1$. However, since Problem (4.31) is formulated for z above the injection filter, i.e. $z > -h_u$, we restrict the solution to these values of z. Furthermore, since (4.35) is a good approximation for small k, we expect that the quality of the approximation (4.37) increases with z.

Using (4.48) the expression for k is easily converted into an expression for the saturation S.

4.5 Applicability of the analytical steady state approximation

The approximation for the steady state depends only on the three numbers N_1, N_2 and m and is valid for $z > -h_u$. We check whether the numerically

Table 4.2: Parameters and dimensionless numbers for checking dependence of the steady state solution on N_1, N_2 and m.

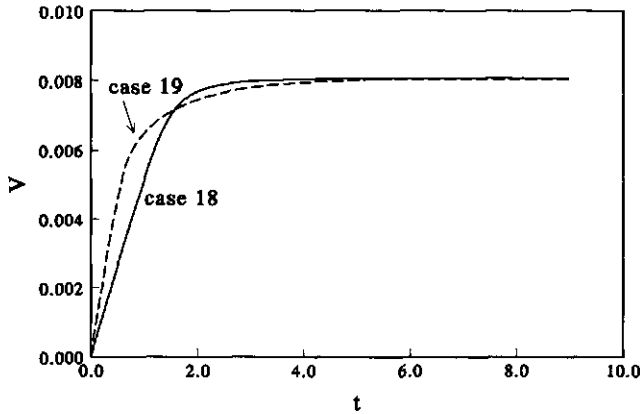| case	α	U_{in}	H	m	N_g	N_c	A
	$\mathrm{m^{-1}}$	$10^{-3}\,\mathrm{m\,s^{-1}}$	m			10^{-3}	
18	1.00	4.42	7.50	0.667	6.63	0.885	5.59
19	1.41	2.21	5.30	0.667	13.3	1.77	11.2

Figure 4.10: Comparison of stored air volumes for cases 18 and 19.

obtained steady state solution also depends on these three numbers for $z >$ $-h_u$. This is done by simulations 18 and 19, for which the input parameters are shown in Table 4.2. The other parameters are the same as in Section 4.3. Observe that although the numbers N_g, N_c and A are different N_1 and N_2 are the same. Computations result into almost identical contour plots of air saturation at steady state, i.e. at large time. However, the transient behavior is different. This is illustrated in Figure 4.10, where the stored air volume $V(t)$ is plotted. We conclude that both steady states are identical. Therefore, also the numerical solutions at steady state depend only on m and the (combined) numbers N_1 and N_2 for $-h_u < z < 0$.

We investigated the agreement between the analytical and numerical solutions at steady state in terms of the relative permeability, $k(r,z)$. For the numerical solution, k is calculated from the air saturation by the van Genuchten relation (4.5). For $-h_u < z < 0$, the relative permeability contour plots of both the analytical and numerical solution for case 1 are shown in Fig-
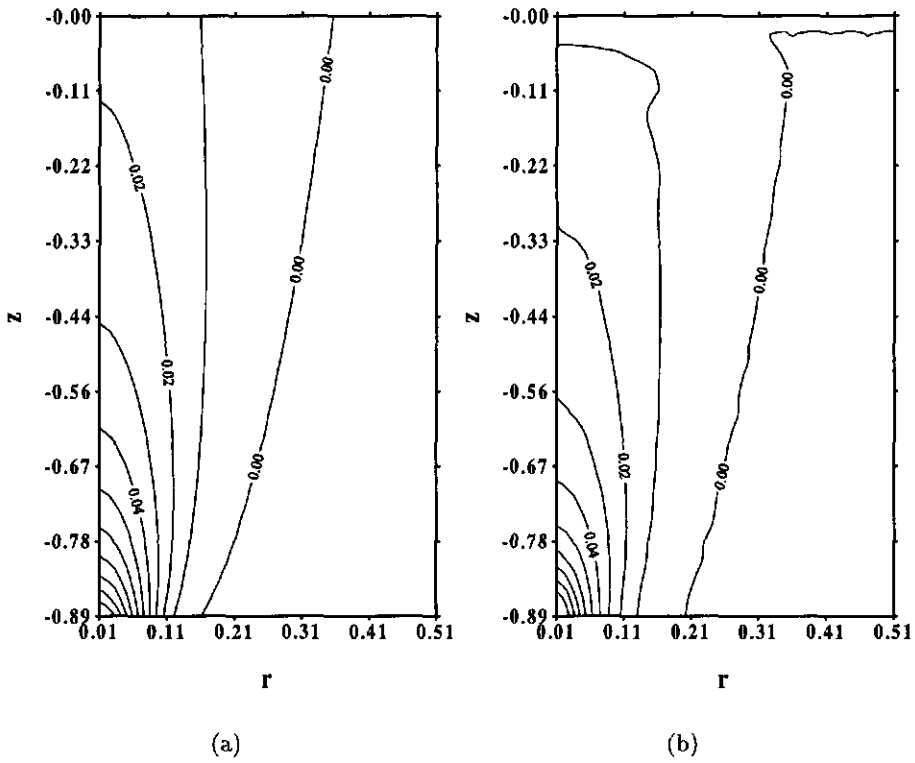
Figure 4.11: Comparison of the relative permeability contour plots of (a) the analytical and (b) the numerical solution (case 1).
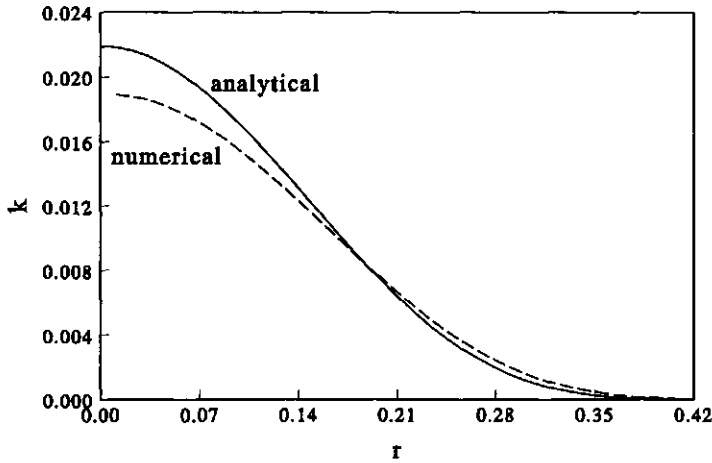
Figure 4.12: Cross-section of the relative permeability profiles $k_{an}(r)$ and $k_{num}(r)$ at $z = -0.2$ (case 1).

ure 4.11. Taking the cross-section of the solutions for $z = -0.2$, we use $k_{an}(r)$ and $k_{num}(r)$ to represent the analytical and numerical solutions respectively, as shown in Figure 4.12. We find that the two profiles give excellent qualitative agreement.

To obtain a quantitative criterion, we compute the masses involved, i.e.

$$I_{an} = \int_0^\infty r \, k_{an}(r) \, dr,$$

see (4.33), and

$$I_{num} = \int_\varepsilon^\infty r \, k_{num}(r) \, dr.$$

Note that I_{num} depends only on N_1, N_2 and m. To plot the relative error $\Delta I = \dfrac{I_{an} - I_{num}}{I_{an}}$ for various values of m, N_1, and N_2, we make use of Table 4.3, which reflects the same computations as shown in Table 4.1. ΔI is shown in Figure 4.13 as a function of the dimensionless numbers, which are normalized with respect to the reference case, indicated by the subscript 1:

$$m_n = \frac{m}{m_1}, \quad N_{1n} = \frac{N_1}{N_{11}}, \quad N_{2n} = \frac{N_2}{N_{21}},$$

for those cases in which only one of the numbers is varied. We observe that the relative error is nearly constant and small (less than 2 %) for most cases, except for values of the parameters taken from case 17. In this case the

Table 4.3: Dimensionless numbers characterizing the steady state.

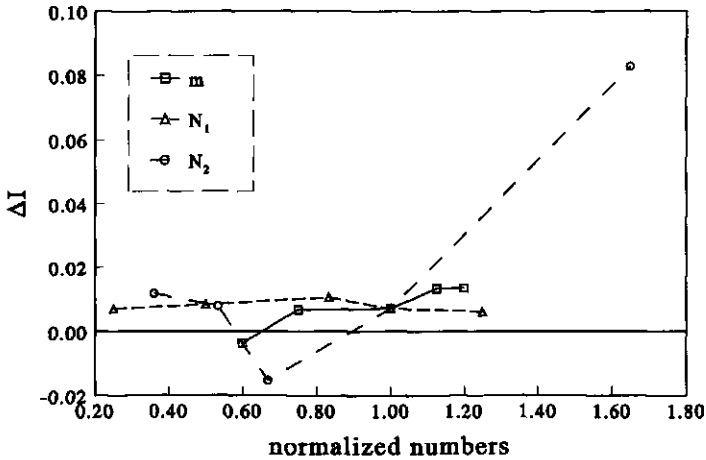| case	m	N_1	N_2 10^{-4}
1	0.667	8.99	7.45
2	0.400	8.99	7.45
3	0.500	8.99	7.45
4	0.750	8.99	7.45
5	0.800	8.99	7.45
6	0.667	3.59	18.6
7	0.667	4.49	14.9
8	0.667	6.74	10.0
9	0.667	13.5	4.96
10	0.667	11.2	7.45
11	0.667	7.49	7.45
12	0.667	4.49	7.45
13	0.667	2.25	7.45
14	0.667	8.99	2.68
15	0.667	8.99	3.97
16	0.667	8.99	4.98
17	0.667	8.99	12.3

Figure 4.13: Relative errors ΔI of the volume integrals versus the dimensionless numbers. The m-curve reflects values of the parameters for cases 2-5, the N_1-curve for cases 10-13 and the N_2-curve for cases 14-17 of Table 4.3.

injection depth h is small and as a consequence both the geometry of the filter and the outflow boundary condition have a relatively large influence on the numerical approximation.

We may conclude that at steady state ($t > 2$ hours) the complex two-phase flow process can be accurately approximated by the relatively simple expressions (4.37) and (4.38). An important qualitative feature of the solution is its radius of influence, $r = f(0) = f_0$, see (4.39), which denotes the outflow radius of the injected air.

4.6   Conclusions

We modeled continuous air injection below the groundwater level as multi-phase flow of two immiscible fluids, with emphasis on the development of the region containing air and the air saturation profile within this region. We found that the solutions depend on four dimensionless numbers, composed of soil, fluid and injection parameters.

Using a numerical model based on the mixed form of the Richards equation for two phases, we made computations for different values of the dimensionless numbers. The computations provided accurate quantitative information about the development of an air cone in the flow domain and about the corresponding saturations. For some cases, the numerical computations showed instabilities during the development of the air cone. Within a short time (about two hours) a steady state situation was reached, which was approximately a single-phase (air) flow process. For all cases air saturations were small in the entire flow domain. Unfortunately, the numerical computations were very time consuming.

An alternative for the use of the two Richards equations is the fractional flow formulation. This formulation involves one equation for the air saturation and one time-independent equation for the total velocity. It presents an understanding of the nonlinearities of the equations and is used for derivation of an upper bound on the air saturation in the flow domain and an approximate analytical solution for the steady state. The observation of small air saturations enabled us to approximate the complicated expressions for the relative permeability and capillary pressure functions by simple power law functions. Assuming that flow in the vertical direction is dominated by advection, we derived the analytical solution for the steady state situation which is valid for the flow domain above the injection filter. This analytical solution was proved to be in good agreement with the numerical results and it depends on three dimensionless numbers, which are a combination of the four numbers mentioned before.

For practical reference we give the expression of the approximate analytical solution for the air saturation and the expression for the dimensionless numbers involved in this approximation. The numbers are

$$N_1 = \frac{(\rho_w - \rho_a)\, H\, \alpha}{\rho_w}, \tag{4.40}$$

$$N_2 = \frac{2\,\mu_a\, U_{\text{in}}\, E\,(H_l - H_u)}{K_{\text{abs}}\,(\rho_w - \rho_a)\, g\, H^2} \tag{4.41}$$

and the exponent m in the nonlinearities. The analytical solution is given by

$$S(r,z) = \begin{cases} n_S\, \left(\dfrac{p_D + 1}{p_D}\,\dfrac{N_2}{f^2(z)}\right)^{p_S} \left(1 - \left(\dfrac{r}{f(z)}\right)^2\right)^{\frac{p_S}{p_D}} \\ \qquad\qquad \text{for} \quad 0 \le r \le f(z), \quad -h_u \le z \le 0 \\[2mm] 0 \qquad\quad\ \text{for} \quad r > f(z), \qquad -h_u \le z \le 0, \end{cases} \tag{4.42}$$

where

$$f(z) = f_0 \cdot (z+1)^{\frac{1}{2\,(p_D+1)}}, \quad \text{for} \ -h_u \le z \le 0 \tag{4.43}$$

with

$$f_0 = \left(\frac{4\,n_D}{N_1}\, N_2^{p_D}\right)^{\frac{1}{2\,(p_D+1)}} \left(\frac{p_D+1}{p_D}\right)^{\frac{1}{2}} \tag{4.44}$$

represents the outer boundary of the air cone.

Note, that in (4.42) dimensionless spatial coordinates r and z need to be inserted. To obtain F_0, the radius of influence in real physical dimension, f_0 must be multiplied by the characteristic length H. Furthermore,

$$n_S = m^{\frac{4\,m}{4\,m+1}}, \qquad\qquad p_S = \frac{2}{4\,m+1},$$

$$n_D = \frac{2\,(1-m)}{4\,m+1}\, m^{\frac{m-1}{4\,m+1}}, \qquad p_D = \frac{2\,(1-m)}{4\,m+1}.$$

For reasonable values of m, such as $0.30 < m < 0.90$, we have $0.52 < n_S < 0.92$, $0.43 < p_S < 0.90$, $0.043 < n_D < 0.93$ and $0.043 < p_D < 0.64$.
To give an impression of the width of air cones, we list the outflow radii F_0 in Table 4.4 for the computations of Section 4.3.

Observe that the coefficient $\dfrac{p_S}{p_D} = \dfrac{1}{1-m}$ in Equation (4.42) satisfies $\dfrac{p_S}{p_D} > 1$ for all $0 < m < 1$, which means that the saturation profile in the r-direction always has zero derivative at the free boundary. Hence, the profile shows a relatively large zone where S is almost zero. Since for remediation purposes a minimum air saturation is necessary, we need to know of the air saturation

Table 4.4: Outflow radii.

case	F_0	case	F_0	case	F_0
	m		m		m
1	2.31	7	3.27	13	4.15
2	1.61	8	2.67	14	3.56
3	1.87	9	1.89	15	3.02
4	2.53	10	2.10	16	2.74
5	2.65	11	2.50	17	1.87
6	3.65	12	3.10	18	3.85

profile to determine at what distance from the injection axis this minimum saturation is reached.

In our calculations we imposed at the filter an influx, which is equally distributed over the length of the filter. However, in practical situations most air leaves the filter near the top [42]. Because for the approximate analytical solution we assumed point source injection, the use of this approximation can be improved by setting the injection level higher than the center of the filter.

Appendix 4A

Power law approximation of the diffusion coefficient

According to the observation that for $z > -h_u$ $S(r, z)$ is significantly smaller than one, we approximate $S(k)$ and $\bar{D}(k) = k\dfrac{d\,p_c}{d\,k}$ by power law functions of the form $n_S\,k^{p_S}$ and $n_D\,k^{p_D}$ respectively, where n_j and p_j $(j = S, D)$ are constants depending on m. The relations (4.5) and (4.12) for the capillary pressure and the relative permeability are:

$$
\begin{aligned}
p_c(S) &= \left((1 - S)^{-\frac{1}{m}} - 1 \right)^{1-m} \\
k(S) &= S^{\frac{1}{2}} \left(1 - (1 - S)^{\frac{1}{m}} \right)^{2m}.
\end{aligned}
$$

Expanding $(1 - S)^{\frac{1}{m}}$ in a binomial series

$$
(1 - S)^{\frac{1}{m}} = 1 - \frac{1}{m}S + \frac{1}{2}\left(\frac{1}{m} - 1 \right)\frac{1}{m}S^2 + O(S^3), \qquad (4.45)
$$

we obtain for k

$$
k(S) = m^{-2m}S^{2m+\frac{1}{2}} + O(S^{4m+\frac{1}{2}}). \qquad (4.46)
$$

For $\bar{D}_k(S) = \bar{D}(k(S)) = k(S)\,\dfrac{d\,p_c}{d\,S}(S)\,/\,\dfrac{d\,k}{d\,S}(S)$ we find

$$\bar{D}_k(S) = \frac{2\,(1-m)}{m}\;\frac{S\left(1-(1-S)^{\frac{1}{m}}\right)^{1-m}}{(1-S)^{\frac{1}{m}}\left(1-(1-S)^{\frac{1}{m}}+4\,S\,(1-S)^{\frac{1}{m}-1}\right)}.$$

Again using the series (4.45), we obtain

$$\bar{D}_k(S) = \frac{2\,(1-m)}{4\,m+1}\,m^{m-1}S^{1-m} + O(S^{2-2\,m}), \qquad (4.47)$$

which is only accurate for S close to zero.

Taking first order terms we get

$$S(k) \quad\sim\quad m^{\frac{4\,m}{4\,m+1}}\,k^{\frac{2}{4\,m+1}} \qquad (4.48)$$

$$\bar{D}(k) \quad\sim\quad \frac{2\,(1-m)}{4\,m+1}\,m^{\frac{m-1}{4\,m+1}}\,k^{\frac{2\,(1-m)}{4\,m+1}}. \qquad (4.49)$$

Observe that these approximations are only good for small m, because when $m \uparrow 1$ the first and the higher order terms of equations (4.46) and (4.47) become of the same order of magnitude. We get

$$
\begin{aligned}
n_S &= m^{\frac{4\,m}{4\,m+1}}, & 0 &< n_S < 1,\\[2mm]
p_S &= \frac{2}{4\,m+1}, & \frac{2}{5} &< p_S < 2,\\[2mm]
n_D &= \frac{2\,(1-m)}{4\,m+1}\,m^{\frac{m-1}{4\,m+1}}, & n_D &> 0,\\[2mm]
p_D &= \frac{2\,(1-m)}{4\,m+1}, & 0 &< p_D < 2.
\end{aligned}
\qquad (4.50)
$$

Note, that using the upper bound for S, i.e. $S < S_t$, see (4.26), or equivalently $k < \dfrac{1}{N_g}$, it is possible to find other power law functions by regression analysis, which approximate $\bar{D}(k)$ for $0 \leq k \leq \dfrac{1}{N_g}$. Figure 4.14 shows the function $\bar{D}(k)$ with approximations for $m = 0.750$, which must be valid for $k \leq \dfrac{1}{N_g} = 0.151$. Because the approximation by binomial series shows the correct limiting behavior of $\bar{D}(k)$ for $k \downarrow 0$, we use this approximation for the derivation of the analytical solution.
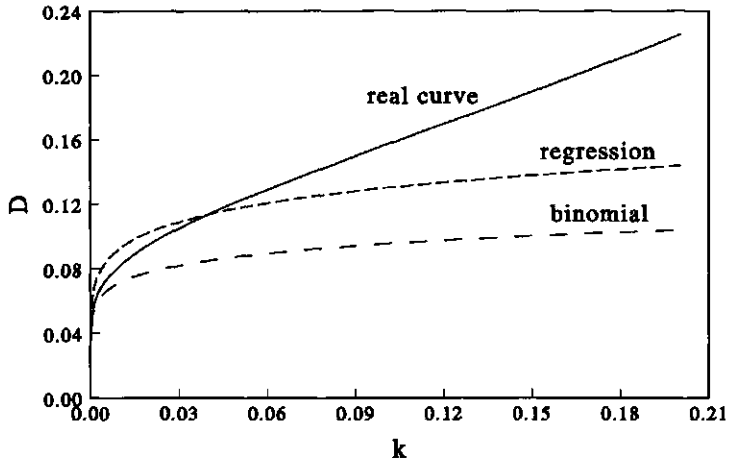
Figure 4.14: Approximations of $\bar{D}(k)$ with $m = 0.750$ for $k \leq 0.151$. Approximation by binomial series yields $(n_D, p_D) = (0.127,\ 0.125)$, whereas regression analysis yields $(n_D, p_D) = (0.182,\ 0.146)$.

Notation

A	dimensionless filter surface
D	dimensionless diffusion function for two-phase flow dependent on S
$\bar{D}$	dimensionless diffusion function for single-phase flow dependent on k
$\vec{e}_z$	unit vector in z-direction
f	dimensionless radial position of free boundary
F	dimensionless z-component of flux function
$\vec{F}$	dimensionless flux function
$F_0\ (f_0)$	(dimensionless) radial position of free boundary at water table [m]
f_a	air fractional flow function
g	gravity [$\mathrm{m\,s^{-2}}$]
H	filter depth [m]
$H_b\ (h_b)$	(dimensionless) vertical position of bottom boundary [m]
$H_l\ (h_l)$	(dimensionless) vertical position of lower side of filter [m]
$H_t\ (h_t)$	(dimensionless) vertical position of top boundary [m]
$H_u\ (h_u)$	(dimensionless) vertical position of upper side of filter [m]
k	redefined air relative permeability
K_{abs}	absolute permeability [$\mathrm{m^2}$]
k_{rj}	phase j relative permeability
m	van Genuchten parameter

M	mobility ratio
$N_1,\ N_2$	dimensionless numbers determining steady state situation
N_c	capillary number
N_{jg}	phase j gravity number
N_g	gravity number
$n_S,\ n_D$	constants in power law approximations
$P_c\ (p_c)$	(dimensionless) capillary pressure [Pa]
$P_j\ (p_j)$	(dimensionless) phase j pressure [Pa]
$P_{jt}\ (p_{jt})$	(dimensionless) phase j pressure at top boundary [Pa]
$p_S,\ p_D$	powers in power law approximations
p_t	dimensionless capillary pressure at top boundary
Q	air injection rate [$\text{m}^3\,\text{s}^{-1}$]
$R\ (r)$	(dimensionless) radial coordinate [m]
$R_b\ (r_b)$	(dimensionless) radial position of right boundary [m]
S	redefined air saturation
S_j	phase j saturation
S_r	residual water saturation
S_t	air threshold saturation
$T\ (t)$	(dimensionless) time [s]
$\vec{U}_j\ (\vec{u}_j)$	(dimensionless) phase j Darcy velocity [$\text{m}\,\text{s}^{-1}$]
U_{in}	air injection velocity [$\text{m}\,\text{s}^{-1}$]
$\vec{u}_t$	dimensionless total fluid velocity
V	dimensionless air volume in flow domain
$Z\ (z)$	(dimensionless) vertical coordinate [m]
α	van Genuchten parameter
$E\ (\varepsilon)$	(dimensionless) filter radius [m]
λ	mobility function
μ_j	phase j viscosity [$\text{Pa}\,\text{s}$]
ρ_j	phase j density [$\text{kg}\,\text{m}^{-3}$]
ϕ	porosity

Chapter 5

Modeling of air sparging in a layered soil: numerical and analytical approximations

5.1 Introduction

A method for remediating an aquifer which is contaminated by organic liquids (solvents, gasoline) trapped in the saturated zone, is to inject air or oxygen into the aquifer. Injection of air into the saturated zone, known as air sparging, may enhance microbial degradation and volatilization.

Air sparging has been studied experimentally on both field [34, 41, 42] and laboratory [32, 61] scales, with emphasis on defining the region in the saturated zone where air is present (radius of influence). These studies emphasize that variations in soil texture strongly affect the air flow. Air sparging is only possible in relatively coarse-grained soils [34] and in most cases air flow appears to occur in small continuous channels.

The assumption of flow continuity has been used to model air sparging as a multi-phase flow process, see also [43, 46, 57] and Chapter 4. Besides flow continuity, air-phase compressibility may be a complicating factor in modeling air sparging. In Chapter 4 the conclusion was reached, supported by a field study [41], that in the steady state situation in which continuous channels to the vadose zone exist, compressibility is likely to play a minor role.

Considering air and water as two immiscible incompressible continuous phases, in Chapter 4 the effect of soil, fluid and filter parameters on the radius of influence of a single injection filter in a homogeneous medium was analyzed. In many situations, however, aquifers contain less permeable regions, which may control the main direction of air flow. The effect of heterogeneities has been demonstrated by several numerical studies [43, 57]. In this chapter we model air sparging below a less permeable horizontal layer with large lateral extension. We assume that the different layers have similar structure but different mean pore size, i.e. the similar media assumption [40, 44]. Our purpose was to investigate the air flow through layered soils, in particular

the quantitative effect of the degree of heterogeneity and the position of the interface, that separates the layers, on the resulting radius of influence.

In Section 5.2 we present the transient model: the basic equations with their saturation dependent relative permeability and capillary pressure functions and the geometry of the domain including the two different layers. To accommodate analysis of the steady state situation, we reformulate the problem in dimensionless form and identify the governing dimensionless numbers. Thus, we present similar equations with different parameters for the two subdomains, which are linked by continuity of capillary pressure and of the vertical air velocity component at the interface.

In Section 5.3 we analyze the steady state situation that occurs when air flow from the injection well to the vadose zone has been established. Emphasis is given to the region just below the interface, where air mainly spreads horizontally. We assume that flow in this region is ruled by vertical equilibrium, despite a small vertical air velocity component across the interface. An ordinary differential equation for the capillary pressure at the interface governs the radial extension of air below the interface.

In Section 5.4 we present the results of numerical simulations that are based on the transient model, which show that indeed a steady state situation is approached. In terms of capillary pressure the numerical solutions are compared to the analytical approximation. On the basis of our analytical approximation, we carried out a sensitivity analysis of the effect of the dimensionless numbers, especially the measure of the heterogeneity, on the saturation profile at the interface.

Our analysis is related to a study on DNAPL flow on a low permeable layer of finite horizontal extension, where conditions for DNAPL infiltration into the layer in terms of the contrast in entry pressures were derived [22]. Therefore, we show in Appendix 5B that with a few modifications, the present study may also reveal how DNAPL leaks through a low permeable layer.

5.2   Model

According to Chapter 4 we use for both air (a) and water (w) Darcy's Law

$$\vec{U}_j = -\frac{K\,k_j}{\mu_j}\,\nabla\,(P_j + \rho_j\,g\,Z), \quad j = w, a \tag{5.1}$$

and the mass balance equations

$$\phi\,\frac{\partial S_j}{\partial t} + \nabla \cdot \vec{U}_j = 0 \quad j = w, a, \tag{5.2}$$
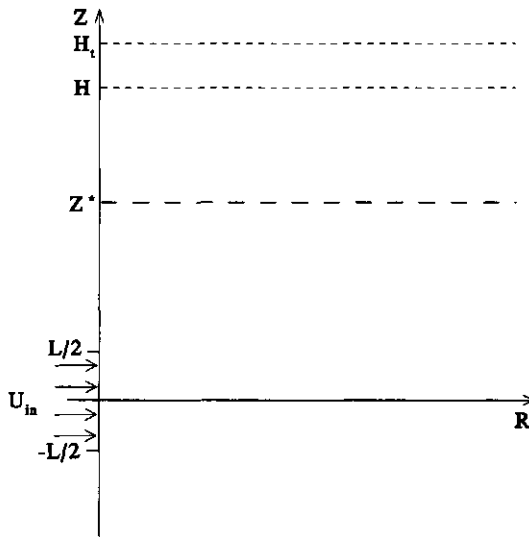
Figure 5.1: Schematic of the domain for air sparging.

where K denotes soil absolute permeability, ϕ soil porosity, S_j effective fluid saturation, $\vec{U}_j$ fluid Darcy velocity, k_j fluid relative permeability, μ_j fluid viscosity, P_j fluid pressure, ρ_j fluid density and g gravity. We assume that both fluids are incompressible and that the soil is isotropic, but consists of two layers.

The set of equations (5.1) and (5.2) is completed by the constitutive relations $S_w + S_a = 1$, the capillary pressure $P_c = P_a - P_w$, $S_j = S_j(P_c)$ and $k_j = k_j(S_j)$. The dependence of capillary pressure and relative permeability on the saturations is given by the expressions [47]

$$P_c(S_a) = \frac{\rho_w g}{\alpha} \left((1 - S_a)^{-\frac{1}{m}} - 1 \right)^{1-m} \tag{5.3}$$

$$k_w(S_w) = S_w^{\frac{1}{2}} \left(1 - (1 - S_w^{\frac{1}{m}})^m \right)^2 \tag{5.4}$$

$$k_a(S_a) = S_a^{\frac{1}{2}} \left(1 - (1 - S_a)^{\frac{1}{m}} \right)^{2m}, \tag{5.5}$$

where $0 < m < 1$ is a given constant and $\alpha > 0$ differs for each layer.

Equations (5.1) and (5.2) are solved in the two-dimensional axially symmetric domain of Figure 5.1 for time $T > 0$. The level $Z = H$ corresponds to the initial position of the water table. Hence, the water pressure along the top boundary of the domain, $Z = H_t$, is $P_w = \rho_w g (H - H_t)$, and the air pressure equals $P_a = 0$. For $T > 0$, air is injected with velocity U_{in} into this domain

through a vertical filter with radius $E > 0$, located between $Z = \pm L / 2$. This yields a total injection rate $Q = 2 \pi E L U_{\text{in}}$. The remaining part of the vertical line $R = E$ that represents the injection well tube, is considered to be impermeable.

We consider two subdomains, separated by an interface at depth $Z = Z^*$, where

$$K = \begin{cases} K^- & \text{for } Z < Z^* \\ K^+ & \text{for } Z > Z^* \end{cases} \quad \text{and} \quad \alpha = \begin{cases} \alpha^- & \text{for } Z < Z^* \\ \alpha^+ & \text{for } Z > Z^*. \end{cases} \tag{5.6}$$

We assume that the two layers have similar structure, reflected by a single m-value for the entire domain, but that they have different mean pore size. Hence, in agreement with the scaling theory of similar media [40, 44] we take $K^+ = \gamma^2 K^-$ and $\alpha^+ = \gamma \alpha^-$, with constant K^- and α^- and heterogeneity factor $0 < \gamma < 1$. At the interface $Z = Z^*$, we have continuity of capillary pressure P_c and of the vertical components of the Darcy velocities $U_{j,z}$.

With numerical simulations, which are described in Section 5.4, we show that flow approaches a steady state. At steady state the water pressure is approximately hydrostatic, see [43] and Section 4.3, and air flow is described by the mass balance

$$\nabla \cdot \vec{U}_a = 0, \tag{5.7}$$

with

$$\vec{U}_a = -\frac{K k_a}{\mu_a} \nabla (P_c - \Delta \rho g Z), \tag{5.8}$$

where $\Delta \rho = \rho_w - \rho_a$.

We introduce the dimensionless variables

$$r = \frac{R}{H}, \quad z = \frac{Z}{H}, \quad \vec{u}_a = \frac{\vec{U}_a}{U_{\text{in}}}, \quad p_c = \frac{\alpha^- P_c}{\rho_w g}, \tag{5.9}$$

where H, the depth of the filter center below the water table, is chosen as a characteristic length. Furthermore, we define the dimensionless constants

$$\varepsilon = \frac{E}{H}, \quad z^* = \frac{Z^*}{H}, \quad h_t = \frac{H_t}{H}$$

and

$$N_g = \frac{K^- \Delta \rho g}{\mu_a U_{\text{in}}}, \quad N_c = \frac{K^- \rho_w g}{\mu_a U_{\text{in}} H \alpha^-}, \quad A = \frac{Q}{U_{\text{in}} H^2} \tag{5.10}$$

which are the gravity number, the capillary number and the dimensionless filter surface respectively. The resulting equations are

$$\nabla \cdot \vec{u}_a = 0, \tag{5.11}$$

with

$$\vec{u}_a = \begin{cases} -N_c\,k_a\,\nabla\,p_c + N_g\,k_a\,\vec{e}_z & \text{for } z < z^* \\ -\gamma\,N_c\,k_a\,\nabla\,p_c + \gamma^2\,N_g\,k_a\,\vec{e}_z & \text{for } z > z^*, \end{cases} \tag{5.12}$$

where $\vec{e}_z$ is the unit vector in the vertical direction. The capillary pressure function has transformed into

$$p_c(S_a) = \begin{cases} \bar{p}_c(S_a) & \text{for } z < z^* \\ \dfrac{1}{\gamma}\,\bar{p}_c(S_a) & \text{for } z > z^*, \end{cases} \quad \text{with } \bar{p}_c(S_a) = \left((1 - S_a)^{-\frac{1}{m}} - 1\right)^{1-m}.$$
$$\tag{5.13}$$

As shown in Chapter 4 the steady state flow problem is determined by the combined dimensionless numbers

$$N_1 = \frac{N_g}{N_c} \quad \text{and} \quad N_2 = \frac{A}{\pi\,N_g} \tag{5.14}$$

and the exponent m. The number N_2 is derived from the total flow rate

$$2\,\pi \int_0^\infty r\,u_{a,z}\,dr = A, \tag{5.15}$$

Furthermore, z^* and γ characterize the position and the degree of heterogeneity.

5.3 Steady state flow analysis

To analyze the steady state situation we distinguish three regions which have different air flow regimes as shown in Figure 5.2. Provided that the distance between the injection filter and the interface is large enough, we assume that upwards from the filter a region (I) exists where the vertical velocity component is dominated by advection. In view of a study on DNAPL infiltration above a low permeable layer [22] and supported by our numerical simulations, we expect that just below the interface that separates the low and the high permeable subdomains, a region (II) exists where the radial spreading of the air flow is much larger than in the advection dominated region, whereas in the vertical direction diffusion and advection are of equal magnitude. We assume that above the interface and below the water table (region III) advection dominates the vertical velocity component. The three regions are enclosed outward by the free boundaries $r = f_I(z)$, $r = f_{II}(z)$ and $r = f_{III}(z)$ respectively.

In region I saturations are significantly smaller than one, which allows approximation of the relations between saturation, relative permeability and (reduced) capillary pressure by simple power law functions, see Appendix 4A.
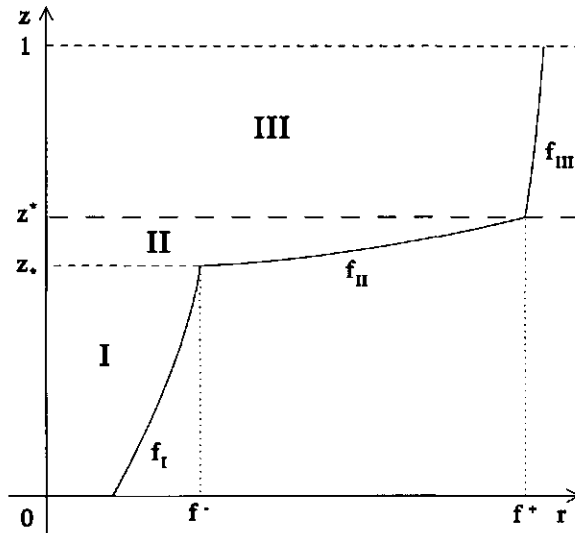
Figure 5.2: Regions with different steady state air flow regimes.

The relations for the saturation and the (reduced) capillary pressure in terms of the relative permeability are given according to Appendix 4A by

$$S_a(k_a) \sim n_S\, k_a^{p_S} \quad \text{and} \quad \bar{p}_c(k_a) \sim \frac{n_D}{p_D}\, k_a^{p_D}, \tag{5.16}$$

where

$$n_S = m^{\frac{4\,m}{4\,m+1}}, \quad p_S = \frac{2}{4\,m+1}, \quad n_D = \frac{2\,(1-m)}{4\,m+1}\, m^{\frac{m-1}{4\,m+1}}, \quad p_D = \frac{2\,(1-m)}{4\,m+1}. \tag{5.17}$$

Considering the filter as a point source and neglecting the filter diameter, the air flow is described by a similarity solution, the Barenblatt-Pattle point source solution (4.37), that in terms of capillary pressure is given by

$$p_c(r,z) = \begin{cases} \left(\dfrac{p_D+1}{p_D} \dfrac{N_2}{f^2(z)} \right)^{p_D} \left(1 - \dfrac{r^2}{f^2(z)} \right) & \text{for } 0 \le r \le f(z), \quad z > 0 \\ 0 & \text{for } r > f(z), \quad z > 0. \end{cases} \tag{5.18}$$

The free boundary f separating the regions with and without air is given by

$$f(z) = f_0\, z^{\frac{1}{2\,(p_D+1)}} \quad \text{for } z \ge 0 \tag{5.19}$$

with

$$f_0 = \left(\frac{4\,n_D}{N_1}\, N_2{}^{p_D} \right)^{\frac{1}{2\,(p_D+1)}} \left(\frac{p_D+1}{p_D} \right)^{\frac{1}{2}}. \tag{5.20}$$

This approximation is valid for (r, z) in region I, where $f_I(z) = f(z)$.

To develop an approximate solution for region II, we consider the continuity conditions at the interface. Continuity of the vertical component of the velocity yields with (5.12)

$$\lim_{z \uparrow z^*} -N_c \, k_a \, \frac{\partial p_c}{\partial z} + N_g \, k_a \sim \lim_{z \downarrow z^*} \gamma^2 \, N_g \, k_a \qquad (5.21)$$

assuming that above the interface advection is dominant. Continuity of pressure yields with (5.13)

$$\lim_{z \downarrow z^*} \bar{p}_c = \gamma \lim_{z \uparrow z^*} \bar{p}_c, \qquad (5.22)$$

which shows for $\gamma < 1$ that saturations and relative permeabilities above the interface are smaller than below, i.e.

$$\lim_{z \downarrow z^*} k_a < \lim_{z \uparrow z^*} k_a. \qquad (5.23)$$

Hence, we may neglect the right-hand side of relation (5.21), and we obtain for the pressure gradient just below the interface

$$\frac{\partial p_c}{\partial z} \sim \frac{N_g}{N_c}. \qquad (5.24)$$

Equation (5.24) is the vertical equilibrium assumption, which controls flow in region II. Neglecting for convenience the transition zone between the advection dominated and the vertical equilibrium regime, regions I and II meet at some level $z = z_*$ $(0 < z_* < z^*)$ as shown in Figure 5.2. Here, we define f^- as the radial position where f_I changes into f_{II}. Furthermore, f^+ indicates the radial position where f_{II} changes into f_{III}.

Especially if the contrast of material properties below and above the interface is large $(\gamma \ll 1)$, we expect that $f^- \ll f^+$. Consequently, we assume that the advection dominated regime only slightly affects the vertical equilibrium regime. Hence, we analyze the flow in region II separately, thus neglecting continuity with region I at $z = z_*$, except that the total flow rate condition (5.15) is satisfied for every horizontal plane.

We vertically integrate in region II the hydrostatic pressure relation (5.24) until the interface, i.e.

$$p_c(r, z) = p(r) - \frac{N_g}{N_c} (z^* - z), \qquad (5.25)$$

which shows that the capillary pressure at the interface $p(r) = p_c(r, z^*)$ also determines the capillary pressure elsewhere in the vertical equilibrium region.

Furthermore, relation (5.25) specifies a boundary $z = z_f(r)$ for $\varepsilon \le r \le f^+$, where $p_c = 0$, i.e.

$$z_f(r) = z^* - \frac{N_c}{N_g} p(r). \tag{5.26}$$

We vertically integrate the mass balance equation (5.11) from z_f to z^*, which yields

$$\frac{\partial}{\partial r} \left(r \int_{z_f}^{z^*} u_{a,r}\, dz \right) + r\, u_{a,z}(r, z^*) = 0 \quad \text{for } \varepsilon < r < f^+. \tag{5.27}$$

To evaluate the integral, i.e. the effective horizontal flux, we derive from relation (5.25)

$$\frac{\partial p_c}{\partial r} = \frac{dp}{dr} \quad \text{and } dz = \frac{N_c}{N_g}\, dp_c, \tag{5.28}$$

leading to

$$\int_{z_f}^{z^*} u_{a,r}\, dz = -N_c \int_{z_f}^{z^*} k_a \frac{\partial p_c}{\partial r}\, dz = -\frac{N_c^2}{N_g} D(p) \frac{dp}{dr}. \tag{5.29}$$

The effective 'diffusion' coefficient is defined by $D = \int_0^p k(\xi)\, d\xi$, with $k(p_c) = k_a(S_a(p_c))$, where ξ is a dummy variable for integration over the range of p_c values. By continuity the vertical velocity component $u_{a,z}(r, z^*)$ is given by the right-hand side of relation (5.21). Using also continuity of capillary pressure (5.22), we obtain

$$-\frac{N_c^2}{N_g} \frac{d}{dr} \left(r\, D(p) \frac{dp}{dr} \right) + r\, \gamma^2 N_g\, k(\gamma p) = 0. \tag{5.30}$$

Integration of equation (5.27) over r from ε to f^+ and application of the mass balance condition (5.15) at the interface yields the boundary condition

$$-2\pi \frac{N_c^2}{N_g} \left(r\, D(p) \frac{dp}{dr} \right) \Bigg|_{r=\varepsilon} = A \tag{5.31}$$

where we have used that the flux (5.29) vanishes at $r = f^+$. Hence, we must solve the boundary value problem

$$\begin{cases} \dfrac{d}{dr} \left(r\, D(p) \dfrac{dp}{dr} \right) - r\, \gamma^2 N_1^2\, k(\gamma p) = 0 \quad \text{for } \varepsilon < r < f^+ \\[2ex] -\left(r\, D(p) \dfrac{dp}{dr} \right) \Bigg|_{r=\varepsilon} = \dfrac{N_1^2 N_2}{2}, \quad p(f^+) = 0, \end{cases} \tag{5.32}$$

for $p(r)$, where we have used definitions (5.14) for N_1 and N_2. In Appendix 5A we show that at $r = f^+$ the derivative $\dfrac{dp}{dr}(f^+)$ satisfies

$$\frac{dp}{dr}(f^+) = -\gamma^{1+\frac{1}{2p_D}} N_1. \tag{5.33}$$

Hence, we solve problem (5.32) simultaneously for $p(r)$ and f^+ as described in Appendix 5A.

Using the solution $p(r)$ in equation (5.26), we find $z = z_f(r)$. Intersection of $z = z_f(r)$ and $r = f(z)$ (5.19), yields the pair (f^-, z_*). Hence, we approximate capillary pressure for $z < z_*$ (region I) by equation (5.18) and for $z_* < z < z^*$ (region II) by equation (5.25) and the solution $p(r)$ of system (5.40). The free boundary $r = f_{II}(z)$ along region II is given by $r = z_f^{-1}(z)$ for $z_* < z < z^*$.

Assuming that above the interface flow is dominated by advection and saturations are small, we may expect that the pressure distribution satisfies approximately the similarity profile (5.18). However, the radial extension of the air distribution is already so large at the interface, that upwards to the unsaturated zone the radial spreading according to this profile will be small. Moreover, numerical simulations show that in the vicinity of the water table the extension tends to decrease. Hence, we approximate for region III

$$p_c(r, z) = p_c(r, z^*) \quad \text{for } z > z^*, \tag{5.34}$$

with $f_{III}(z) = f^+$.

5.4 Results

5.4.1 Numerical computations

Using the numerical model of Section 4.3 we solved the transient two-phase flow problem of Section 5.2 described by equations (5.1-5.6) on the finite domain $E < R < R_b$ and $-H_b < Z < H_t$ $(H_b > 0)$, where R_b and H_b were chosen such that injected air never reached these boundaries. We imposed at the lower boundary a no-flow condition $(U_{j,z} = 0)$. At the right boundary we imposed hydrostatic water pressures $(P_w = \rho_w\, g\, (H - Z))$, no air flow below the water table $(U_{a,r} = 0$ for $Z < H)$ and hydrostatic air pressures above the water table $(P_a = \rho_a\, g\, (H_t - Z)$ for $Z > H)$. The flow domain was discretized by linear triangular finite elements and time discretization was fully implicit. The resulting algebraic equations were solved by the modified Picard method, that gave good mass balances [13]. In R-direction we used 30 elements of linearly increasing width (the width of the last element was 4.63 times the width of the first element). The Z-grid was uniform with 0.25 m elements, except

Table 5.1: Parameters and dimensionless numbers used in computations. Relative to the reference case (case 1), γ is varied for cases 2-6, z^* for cases 7-10, N_1 for cases 11-12, N_2 for cases 13-14 and m for cases 15-16.

case	γ	z^*	m	N_1	N_2 10^{-5}
1	0.600	0.500	0.700	16.0	20.0
2	1.00	0.500	0.700	16.0	20.0
3	0.800	0.500	0.700	16.0	20.0
4	0.700	0.500	0.700	16.0	20.0
5	0.500	0.500	0.700	16.0	20.0
6	0.400	0.500	0.700	16.0	20.0
9	0.600	0.188	0.700	16.0	20.0
10	0.600	0.313	0.700	16.0	20.0
11	0.600	0.688	0.700	16.0	20.0
12	0.600	0.875	0.700	16.0	20.0
13	0.600	0.500	0.700	7.99	20.0
14	0.600	0.500	0.700	32.0	20.0
15	0.600	0.500	0.700	16.0	50.0
16	0.600	0.500	0.700	16.0	4.00
17	0.600	0.500	0.800	16.0	20.0
18	0.600	0.500	0.556	16.0	20.0

for a 0.5 m thick layer from the interface downward, where we expected the vertical equilibrium regime. There, we used 5 elements of linearly decreasing thickness (the thickness of the last element was 0.220 times the thickness of the first element at the top of the layer). Convergence was obtained for the Picard iterations by adjusting the time steps. Computations were done in non-transformed physical variables.

The following soil and fluid parameters were fixed during all computations: ϕ=0.400, μ_a=1.77 $\cdot$ 10^{-5} Pa s, ρ_a=1.24 kg m^{-3}, μ_w=1.30 $\cdot$ 10^{-3} Pa s, ρ_w=1.00 $\cdot$ 10^3 kg m^{-3}, g=9.8 m s^{-2}, U_{in} = 7.07 $\cdot$ 10^{-3} m s^{-3}, whereas the latter reflects a total injection rate of 8.00 m^3 h^{-1}. Parameters involving the boundary conditions were: E=5.00$\cdot$$10^{-2}$ m, L=1.00 m, H=8.00 m, H_t=9.00 m. We varied the exponent m, the dimensionless numbers N_1 and N_2 and the heterogeneity parameters γ and z^* with respect to the reference case (case 1) as is summarized in Table 5.1. Variations in N_1 and N_2 were due to variations in α^- and K^- respectively: for the reference case we used $K^- = 1.00 \cdot 10^{-10}$ m^2 and $\alpha^- = 2.00$ m^{-1}.

The numerical results revealed that in every case the air flow became stationary. Defining the steady state time as the time where after the increase of air volume stored in the domain, see Section 4.3, is less than 1 percent,

we found that this time varied between 1 and 5 h for all cases, except for case 5 (7 h), case 6 (35 h) and case 18 (25 h). The simulations required large computation times: roughly between 8 and 48 h on a HP 9000 735/125 workstation.

Results are presented in dimensionless form, see (5.9). We use capillary pressure (p_c) as the main variable, because it is continuous over the entire domain and has a non-zero gradient normal to the free boundary, which makes it easy to determine the position of this boundary. In Figure 5.3 the capillary pressure contours for case 1 and case 6 (large material contrast) at steady state are shown. These contours show a sharp transition from the advection dominated region to the vertical equilibrium region just below the interface. Furthermore, we observe that above the interface the solution is almost constant in the z-direction. As the solution at the interface is characteristic for air injection in layered media, we present in Figure 5.4 the development of capillary pressure at the interface towards the steady state. After injected air has reached the water table (which occurred between 10 and 15 min), air still accumulates at larger radial distances until a steady state is attained.

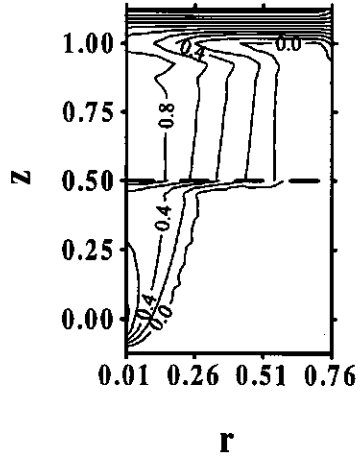### 5.4.2 Applicability of the analytical approximation

In Figure 5.5 we present the capillary pressure contours for case 6 as computed according to the analysis of Section 5.3 in regions I, II and III, which describe the situation between the upper part of the filter and the water table. Comparison with Figure 5.3.b shows good agreement between the two solutions. In Figure 5.6 we show the numerical $p_n(r)$ and analytical $p_a(r)$ steady state capillary pressure functions at the interface for case 1 and 6. Observe that the agreement is much better for the larger material contrast (smaller γ) of case 6.

To quantify the agreement we compared the positions of the free boundary at the interface of the numerical f_n^+ and the analytical f_a^+ solution. Despite the fine discretization just below the interface the numerical profiles exposed small fluctuations near the free boundary. Nevertheless, we were able to accurately estimate f_n^+ from the almost constant slope of the profile at the left side of the fluctuations. In Figure 5.7 we present the relative errors
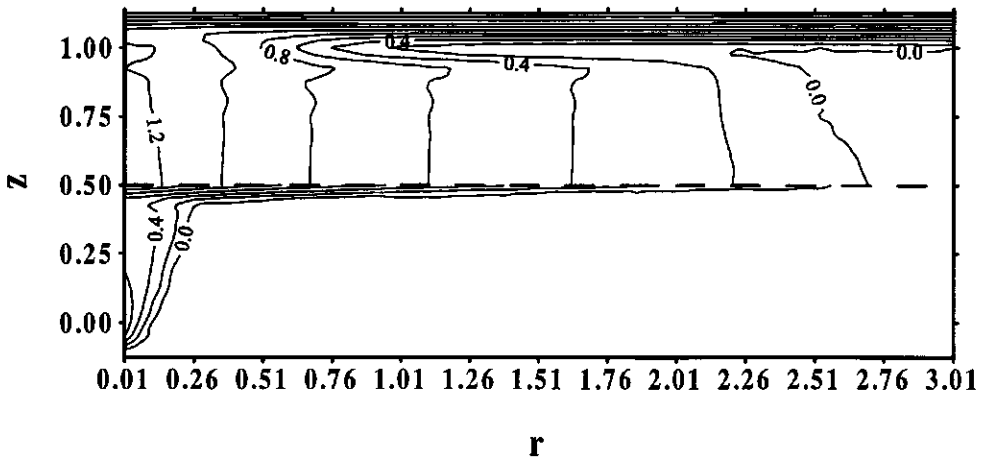
$$\Delta f^+ = \frac{f_n^+ - f_a^+}{f_a^+} \tag{5.35}$$

as functions of

$$\tilde{\gamma} = \frac{\gamma}{\gamma_r}, \quad \tilde{z}^* = \frac{z^*}{z_r^*}, \quad \tilde{m} = \frac{m}{m_r}, \quad \tilde{N}_1 = \frac{N_1}{N_{1r}}, \quad \tilde{N}_2 = \frac{N_2}{N_{2r}}, \tag{5.36}$$

(a)

(b)

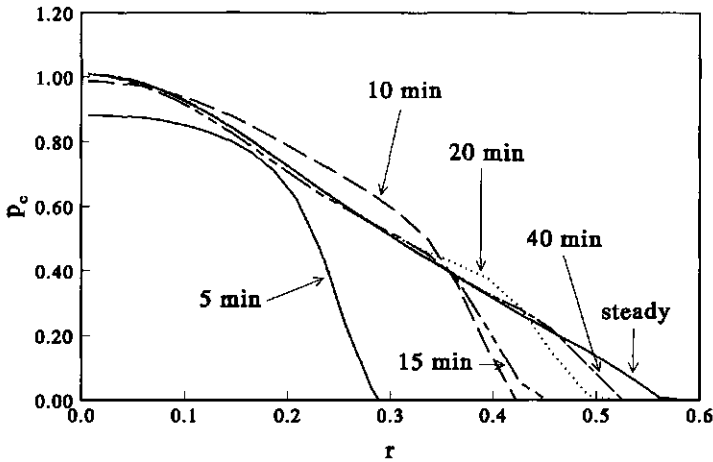**Figure 5.3:** Capillary pressure contours for (a) case 1 and (b) case 2.
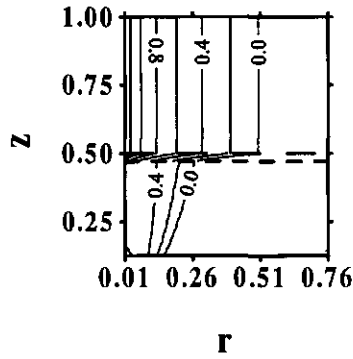
Figure 5.4: Capillary pressure as a function of the radial coordinate at the interface for different times.

which are the dimensionless numbers of Table 5.1 that are normalized with respect to the numbers of the reference case (subscript r). Observe that for larger values of z^*, i.e. the distance between the filter and the interface, the agreement became worse, because the advection dominated solution below the interface resulted in wider air cones, that lead to larger spreading at the interface. Furthermore, we observe that the various soil and fluid parameters, which are combined in N_1, N_2 and m, affect the error Δf^+, but we expect that in every situation with sufficiently small γ the vertical equilibrium assumption is satisfied and that the error Δf^+ is negligible. In most practical situations the value of γ is much smaller than for the reference case ($\gamma = 0.600$) and the analytical approximation performs very well.
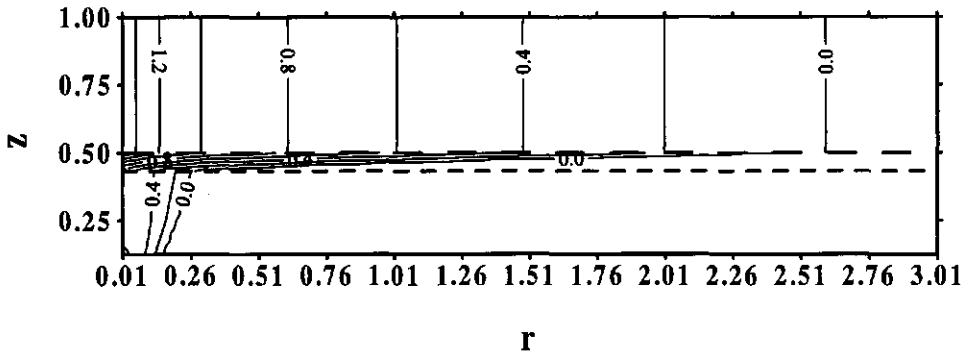
5.4.3 Sensitivity analysis

For remediation purposes saturation is more directly related with mass transfer limitations to volatilization of organic contaminants and to biodegradation than capillary pressure. Therefore, we present in Figure 5.8 for several values of γ, but with the other parameters as in case 1, the saturation profiles at the upper side of the interface, which are based on the analytical approximation. Because for smaller γ the profile has a very long tail with almost zero saturations, we use the first moment

$$M = \frac{\int_\varepsilon^{f^+} r^2 S_a(r, z^*) \, dr}{\int_\varepsilon^{f^+} r \, S_a(r, z^*) \, dr} \tag{5.37}$$
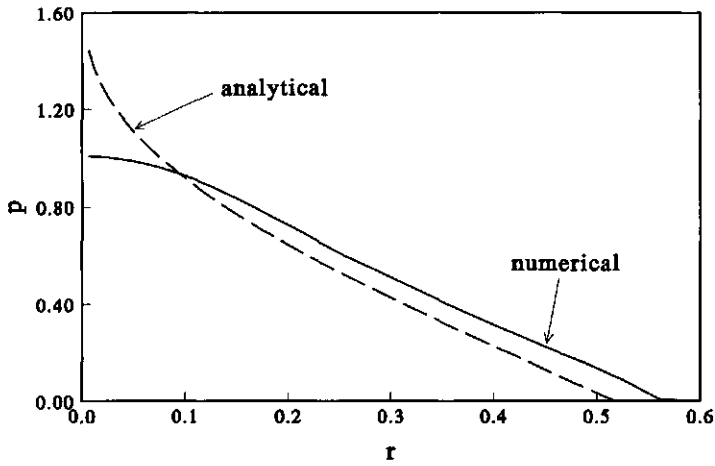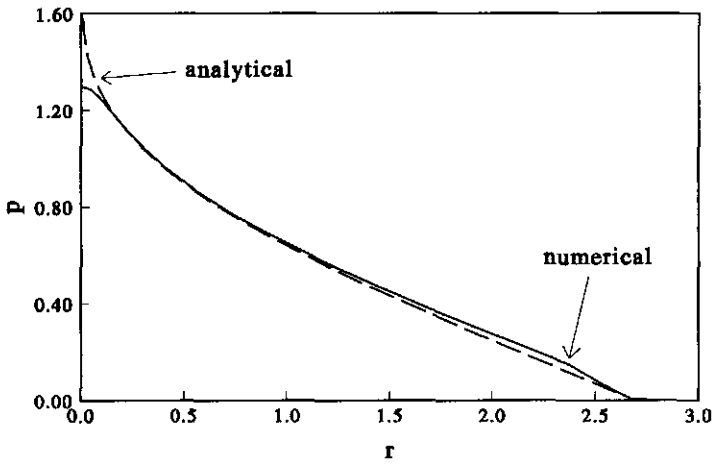
(a)

(b)

Figure 5.5: Contours of the analytically approximated capillary pressure for (a) case 1 and (b) case 6.

(a)

(b)

Figure 5.6: Comparison of the numerically and analytically computed capillary pressures as a function of the radial coordinate for (a) case 1 and (b) case 6 at the interface.

Figure 5.7: Relative errors Δf^+ of the position of the free boundary at the interface versus the normalized dimensionless numbers. The γ-curve reflects values of the parameters for cases 2-6, the z^*-curve for cases 7-10, the m-curve for cases 15-16, the N_1-curve for cases 11-12 and the N_2-curve for cases 13-14.

Figure 5.8: Analytical approximations of the saturation at the upper side of the interface as a function of the radial coordinate for several degrees of heterogeneity.

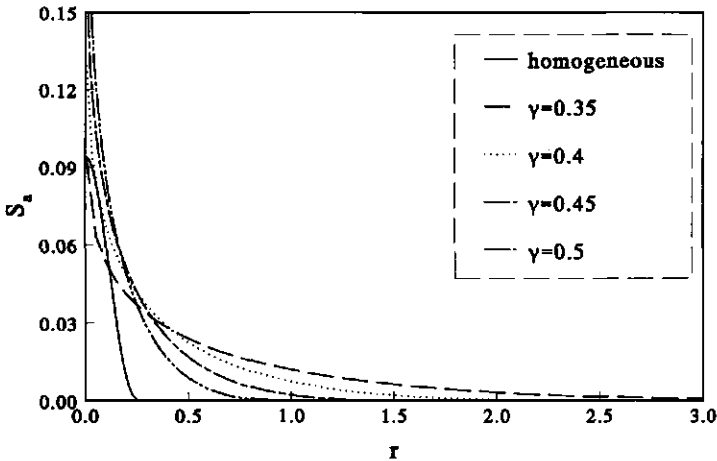as a characteristic distance for the horizontal extension of these profiles rather than the number f^+. M is shown in Figure 5.9 as a function of γ for several sets of the dimensionless numbers m, N_1 and N_2. For small contrasts we expect that the analytical approximation is not valid. To obtain an upper bound γ_s on the values of γ for which we may apply the approximation, we computed the first moment M_s of the similarity solution (5.18) at the interface for the homogeneous situation. Hence, we define γ_s such that $M(\gamma_s) = M_s$ and we present in Figure 5.9 M versus γ up to this upper bound γ_s.

The analysis shows that the spreading is almost insensitive to variations of N_2, but that it varies significantly with N_1 and m. Observe that the analytical approximation does not depend on the position of the interface z^*, whereas the results of the numerical simulations reveal an effect of this parameter which diminishes for decreasing γ, as we showed earlier.

5.5 Conclusions

We modeled air sparging into an aquifer below a less permeable horizontal layer as multi-phase flow of two immiscible fluids. The two layers were assumed to have similar structure but different mean pore size.

We found that flow approaches a steady state, that is characterized by three dimensionless numbers which also control the flow problem for a homogeneous domain and by two numbers which correspond to the position of the interface between the two layers and to the degree of material contrast respectively. Analyzing the steady state situation we distinguished three regions with different flow regimes. In the lower layer above the injection filter the vertical flow component is dominated by advection. Just below the interface a regime with almost vertical flow equilibrium conditions develops, where air tends to spread mainly horizontally. Above the interface the vertical flow component is dominated by advection. In the lowest region steady state flow is approximated by a similarity solution that applies in homogeneous situations, see Section 4.4.2. We analyzed the region just below the interface separately from the lowest region, but incorporated continuity of pressure and vertical flow velocity at the interface towards the less permeable region. Assuming hydrostatic pressures we derived a diffusion equation for the capillary pressure at the interface with a 'loss term' corresponding to the flow through the interface. With a simple numerical procedure we obtained the solution of this ordinary differential equation, which is non-zero within a finite interval of the radial coordinate. This solution determines the capillary pressures in the region below the interface and the free boundary enclosing this region, beyond which air is absent. Between the interface and the water table we assumed that no further changes occur in the radial direction compared to the solution
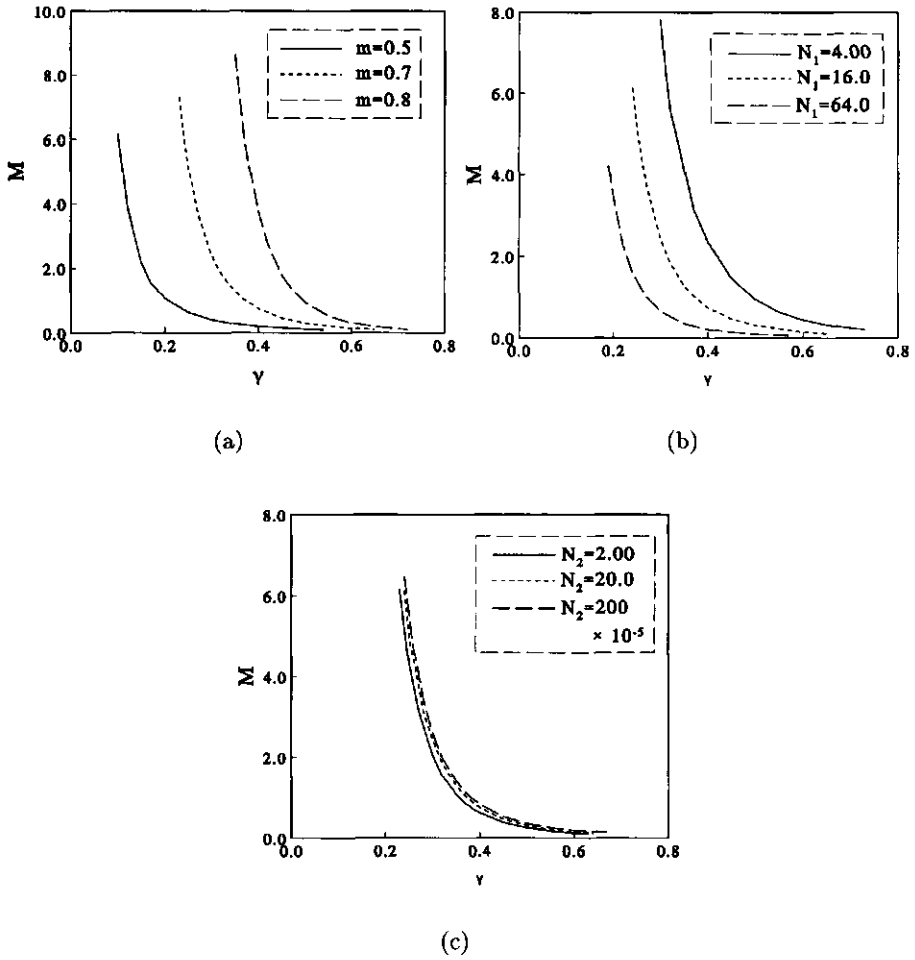
(a)

(b)

(c)

Figure 5.9: First moment M of the horizontal extension of the analytically approximated saturation profiles at the interface versus heterogeneity γ for several values of (a) m, (b) N_1 and (c) N_2.

at the interface.

Using a numerical two-phase flow model we made transient computations for several values of the dimensionless numbers. These computations were very time consuming. In every case we found that the flow reached a steady state situation. However, the time that this was the case and the horizontal spreading of air below the interface increased much with increasing heterogeneity and with increasing values of the exponent m. Only for almost homogeneous flow domains, the position of the interface relative to the injection filter affected the steady state air flow significantly.

We compared the numerical and analytical approximations of the steady state situation with emphasis to the solution at the interface. The agreement between the numerically and analytically obtained radii of influence at the interface was very good when these radii were large compared to the radii of the corresponding homogeneous situations. Else, the vertical equilibrium assumption was less satisfied or the flow below the region with vertical equilibrium affected the numerical solution at the interface significantly.

Because from the remediation point of view the saturation is one of the most important variables, we considered the analytically obtained saturation profile at the interface. We observed that for large values of the radii of influence saturations are almost zero in a large part of the profile. Therefore, we carried out an analysis of the relation between the degree of heterogeneity and the first moment of the horizontal extension of the saturation profile at the interface for several values of the remaining dimensionless parameters. As was expected this spatial moment increases much with increasing heterogeneity and is most sensitive to variations in the exponent m and the dimensionless number N_1.

With minor modifications the present analysis enables the description of the maximum radius of horizontal spreading in case of DNAPL flow over a low permeable layer.

Appendix 5A

Evaluation of the boundary value problem

For steady state flow the free boundary $z_f(r)$ is tangential to the air flow direction. This yields at $r = f^+$

$$\left.\frac{dz_f}{dr}\right|_{r=f^+} = \lim_{r \to f^+} \frac{u_{a,z}(r, z^*)}{u_{a,r}(r, z^*)} = \lim_{r \to f^+} \frac{\gamma^2 N_g \, k(\gamma \, p(r))}{-N_c \, k(p(r)) \frac{dp}{dr}(r)}, \quad (5.38)$$

where we have used the right-hand side of relation (5.21) for $u_{a,z}(r, z^*)$. We differentiate equation (5.26) with respect to r and use it in relation (5.38),

which yields

$$\lim_{r \to f^+} \left(\frac{dp}{dr}(r, z^*) \right)^2 = \lim_{r \to f^+} \gamma^2 N_1^2 \frac{k(\gamma p(r))}{k(p(r))}. \tag{5.39}$$

Using the power law approximation for $k(p)$ (5.16), which is exact if k and p approach zero, we obtain condition (5.33).

Setting $q = p'$, where primes $'$ denote differentiation with respect to r, we transform problem (5.32) into the system of first order equations

$$\begin{cases} p' &= q \\ q' &= -\dfrac{q}{r} - k(p) \dfrac{q^2}{D(p)} + \lambda_1 \dfrac{k(\gamma p)}{D(p)}, \end{cases} \tag{5.40}$$

for $r \in (\varepsilon, f^+)$, with boundary conditions

$$(r \, D(p) \, q)|_{r=\varepsilon} = -\lambda_2, \quad p(f^+) = 0, \quad q(f^+) = -\lambda_3, \tag{5.41}$$

where

$$\lambda_1 = \gamma^2 \, N_1^2, \quad \lambda_2 = \frac{N_1^2 \, N_2}{2}, \quad \lambda_3 = \gamma^{1 + \frac{1}{2 p_D}} \, N_1. \tag{5.42}$$

Using again the power law approximation for $k(p)$ in system (5.40), we obtain additionally $q'(f^+) = \dfrac{\lambda_3}{f^+} \dfrac{p_D}{3 p_D + 2}$, with p_D given by (5.17). Hence, we use a fourth order Runge-Kutta routine to integrate (5.40) iteratively from $r = f^+$ to $r = \varepsilon$, while varying f^+ until the condition at $r = \varepsilon$ is matched.

Appendix 5B

Applicability of the analytical approximation to a DNAPL spill above a less permeable layer

With only minor modifications the analysis of this chapter also describes DNAPL flow below the phreatic surface towards and through a low permeable layer of large horizontal extension. In [22] DNAPL flow above a low permeable layer of finite horizontal extension was investigated. It was assumed that to enter this layer DNAPL must overcome a positive entry pressure. An analysis of the steady state situation for which all DNAPL migrates downward along the lateral boundaries of the layer, revealed the conditions under which the entry pressure is exceeded and DNAPL may infiltrate into the low permeable layer.

Here, we assume that a possible entry pressure has been overcome and that at steady state all DNAPL flows through the low permeable layer. As in [22] we assume that the distance between the DNAPL source and the low permeable

layer is large enough for the development of a region with mainly horizontal flow. Provided that the DNAPL can flow downward away from the interface, after sufficiently large time a steady state situation is reached at the interface. Hence, the steady state solution for the vertical equilibrium region provides an estimate of the maximum horizontal spreading at the interface.

With emphasis on steady state flow above and across the interface, we outline the modifications of the air sparging analysis, that are necessary for the DNAPL flow problem. For this case, the interface Z^* of Figure 5.1 separates the high permeable top and low permeable bottom layers, such that (for $0 < \gamma < 1$)

$$K = \begin{cases} K^- & \text{for } Z > Z^* \\ K^+ & \text{for } Z < Z^* \end{cases} \quad \text{and} \quad \alpha = \begin{cases} \alpha^- & \text{for } Z > Z^* \\ \alpha^+ & \text{for } Z < Z^*, \end{cases} \tag{5.43}$$

with $K^+ = \gamma^2 K^-$ and $\alpha^+ = \gamma \alpha^-$ as before. Assuming that the horizontal extension of the source and of the DNAPL flow field in the high permeable layer is small, horizontal spreading mainly occurs just above the interface. For convenience we still consider a domain with $R > E$ to avoid singularities at $R = 0$.

Equations (5.1) and (5.2) are used with the subscript a for air replaced by o for oil (DNAPL). Because in this steady state situation the water velocity is not negligible due to the smaller difference in density and viscosity [22], we use instead of equation (5.8), the fractional flow formulation for the oil velocity, see e.g. [9, 14],

$$\vec{U}_o = F_o \vec{U}_t - \frac{K k_w}{\mu_w} F_o \nabla (P_c - \Delta \rho g Z), \tag{5.44}$$

where the oil fractional flow function F_o and the mobility ratio M are defined by

$$F_o = \frac{k_o}{k_o + M k_w} \quad \text{and} \quad M = \frac{\mu_o}{\mu_w}, \tag{5.45}$$

the total flow velocity $\vec{U}_t = \vec{U}_w + \vec{U}_o$ and $\Delta \rho = \rho_o - \rho_w$. We obtain in dimensionless form

$$\nabla \cdot \vec{u}_o = 0, \tag{5.46}$$

and

$$\vec{u}_o = \begin{cases} F_o \vec{u}_t - M k_w F_o (N_c \nabla p_c - N_g \vec{e}_z) & \text{for } z > z^* \\ F_o \vec{u}_t - M k_w F_o (\gamma N_c \nabla p_c - \gamma^2 N_g \vec{e}_z) & \text{for } z < z^*, \end{cases} \tag{5.47}$$

with the obvious substitution of the newly defined $\Delta \rho$ in N_g, N_1 and N_2.

Using similar assumptions as in equations (5.21-5.23) we arrive at the vertical equilibrium assumption

$$\frac{\partial p_c}{\partial z} \sim -\frac{N_g}{N_c} \tag{5.48}$$

for the entire region of thickness $z_f - z^*$ on top of the low permeable layer. If oil saturations are small, we may assume that the total velocity $\vec{u}_t = 0$, i.e. counter-current flow $\vec{u}_w = -\vec{u}_o$ [22].

Following the derivation of Section 5.3 we obtain the boundary value problem for the pressure at the interface $p(r)$:

$$\begin{cases} \dfrac{d}{dr}\left(r\,\tilde{D}(p)\,\dfrac{dp}{dr}\right) - r\,\gamma^2\,N_1^2\,\lambda(\gamma p) = 0 & \text{for } \varepsilon < r < f^+ \\[2mm] -\left(r\,\tilde{D}(p)\,\dfrac{dp}{dr}\right)\bigg|_{r=\varepsilon} = \dfrac{N_1^2\,N_2}{2}, \quad p\,(f^+) = 0, \end{cases} \tag{5.49}$$

where $\tilde{D} = \int_0^p \lambda(\xi)\,d\xi$, with $\lambda(p_c) = M\,k_w(S_o(p_c))\,F_o(S_o(p_c))$. However, as p and S_o are small, the water mobility k_w/μ_w is much larger than the oil mobility k_o/μ_o and as a result the function $\lambda(p)$ is approximately equal to $k(p)$. Hence, the boundary condition

$$\frac{dp}{dr}\,(f^+) = -\gamma^{1+\frac{1}{2p_D}}\,N_1 \tag{5.50}$$

is also valid for problem (5.49). Furthermore, we conclude that for small p and S_o problem (5.32) is a good approximation of problem (5.49).

The number f^+ provides an estimate of the maximum spreading radius of DNAPL on top of the low permeable layer.

Notation

A	dimensionless filter surface
D	dimensionless effective diffusion function
$\vec{e}_z$	unit vector in z-direction
f	dimensionless radial position of free boundary in homogeneous soil
f_0	dimensionless radial position of free boundary at water table in homogeneous soil
$f_I,\,f_{II},\,f_{III}$	dimensionless radial positions of free boundaries enclosing various flow regions
f^-	dimensionless radial position where f_I changes into f_{II}
f^+	dimensionless radial position where f_{II} changes into f_{III}
g	gravity $[\mathrm{m\,s^{-2}}]$
H	height of water table above filter [m]
H_b	vertical position of bottom boundary [m]
$H_t\,(h_t)$	(dimensionless) vertical position of top boundary [m]
k	redefined air relative permeability

K	absolute permeability $[\mathrm{m^2}]$
k_j	phase j relative permeability
L	length of injection filter $[\mathrm{m}]$
m	van Genuchten parameter
M	dimensionless first spatial moment of air saturations at interface
$N_1,\ N_2$	dimensionless numbers determining steady state situation
N_c	capillary number
N_g	gravity number
$n_S,\ n_D$	constants in power law approximations
$P_c\ (p_c)$	(dimensionless) capillary pressure $[\mathrm{Pa}]$
$P_j\ (p_j)$	(dimensionless) phase j pressure $[\mathrm{Pa}]$
$P_{jt}\ (p_{jt})$	(dimensionless) phase j pressure at top boundary $[\mathrm{Pa}]$
p	dimensionless capillary pressure at interface
$\bar{p}_c$	dimensionless reduced capillary pressure
$p_S,\ p_D$	powers in power law approximations
Q	air injection rate $[\mathrm{m^3\,s^{-1}}]$
$R\ (r)$	(dimensionless) radial coordinate $[\mathrm{m}]$
R_b	radial position of right boundary $[\mathrm{m}]$
S_j	phase j saturation
T	time $[\mathrm{s}]$
$\vec{U}_j\ (\vec{u}_j)$	(dimensionless) phase j Darcy velocity $[\mathrm{m\,s^{-1}}]$
U_{in}	air injection velocity $[\mathrm{m\,s^{-1}}]$
$Z\ (z)$	(dimensionless) vertical coordinate $[\mathrm{m}]$
$Z^*\ (z^*)$	(dimensionless) vertical position of interface between soil layers $[\mathrm{m}]$
z_*	dimensionless vertical position where lower regions meet
z_f	dimensionless vertical position of free boundary enclosing vertical equilibrium region
α	van Genuchten parameter
γ	degree of heterogeneity
$E\ (\varepsilon)$	(dimensionless) filter radius $[\mathrm{m}]$
μ_j	phase j viscosity $[\mathrm{Pa\,s}]$
ρ_j	phase j density $[\mathrm{kg\,m^{-3}}]$
ϕ	porosity

Bibliography

[1] Abriola, L.M. & Pinder, G.F., A multiphase approach to the modeling of porous media contamination by organic compounds, 1. equation development. *Water Resour. Res.*, **21** (1985) 11-18.

[2] Aronson, D.G., The porous medium equation. In *Some problems in nonlinear diffusion*, edited by A. Fasano and M. Primecerio, Lecture notes in mathematics, No. 1224, Springer Verlag, New York, 1986.

[3] Aziz, K. & Settari, A., *Petroleum reservoir simulation*, Academic Press, New York, 1979.

[4] Baiocchi, C. & Capelo, A., *Variational and quasivariational inequalities*, John Wiley, New York, 1984.

[5] Barenblatt, G.I., On some unsteady motions of a liquid or a gas in a porous medium. *Prikl. Mat. Mekh.*, **16** (1952), 67-78 (in Russian).

[6] Barenblatt, G.I., *Dimensional analysis*, Gordon and Breach, New York, 1987.

[7] Barenblatt, G.I., Entov, V.M. & Ryzhik, V.M., *Theory of fluid flows through natural rocks*, Kluwer Academic Publishers, Dordrecht, 1990.

[8] Barenblatt, G.I. & Zel'dovich Y.B., On dipole-solutions in problems of non-stationary filtration of gas under polytropic regime. *Prikl. Mat. Mekh.*, **21** (1957) 718-720.

[9] Bear, J., *Dynamics of fluids in porous media*, Elsevier, New York, 1972.

[10] Bear, J., Ryzhik, V., Braester, C. & Entov, V., On the movement of an LNAPL lens on the water table. *Transport in Porous Media*, **25** (1996) 283-311.

[11] Blunt, M., Dengen Z. & Fenwick, D., Three phase flow and gravity drainage in porous media. *Transport in Porous Media*, **20** (1995) 77-103.

140

[12] Böhler, U., Brauns, J., Hötzl, H. & Nahold, M., Air injection and soil air extraction as a combined method for cleaning contaminated sites-observations from test sites in sediments and solid rocks. In *Contaminated soil '90*, edited by F. Ahrendt e.a., Kluwer Academic Publishers, Dordrecht, 1990, pp. 1039-1044.

[13] Celia, M.A., Bouloutas, E.T. & Zarba, R.L., A general mass-conservative numerical solution for the unsaturated flow equation. *Water Resour. Res.*. **26** (1990) 1483-1496.

[14] Chavent, G. & Jaffré, J., *Mathematical models and finite elements for reservoir simulation*, edited by J.L. Lions, Studies in mathematics and its applications, Vol 17, North-Holland, Amsterdam, 1986.

[15] Chen, M.-R., Hinkley, R.E. & Killough, J.E., Computed tomography imaging of air sparging in porous media. *Water Resour. Res.*, **32** (1996) 3013-3024.

[16] Corapcioglu, M.Y., Tuncay, K., Lingam, R. & Kambham, K.K.R., Analytical expressions to estimate the free product recovery in oil-contaminated aquifers. *Water Resour. Res.* **30** (1994) 3301-3311.

[17] Corapcioglu, M.Y., Tuncay, K. & Ceylan, B.K., Oil mound spreading and migration with ambient groundwater flow in coarse porous media. *Water Resour. Res.*, **32** (1996) 1299-1308.

[18] Crank, J., *Free and moving boundary problems*, Clarendon Press, Oxford, 1984.

[19] Craven, A.H. & Peletier, L.A., Similarity solutions for degenerate quasi-linear parabolic equations. *J. Math. Anal. Appl.*, **38** (1972) 73-81.

[20] Crow, W.L., Anderson, E.P., & Minugh, E.M., Subsurface venting of vapors emanating from hydrocarbon product on groundwater. *Ground Water Mon. Rev.*, **7** (Winter 1987), 51-57.

[21] Dake, L.P., *Fundamentals of reservoir engineering*, Elsevier, Amsterdam, 1978.

[22] De Neef, M.J. & Molenaar, J., Analysis of DNAPL infiltration in a medium with a low permeable lens. *Comp. Geosciences* (1997) in press.

[23] Dullien, F.A.L., *Porous media : fluid transport and pore structure*, 2nd ed., Academic Press, San Diego, 1992.

[24] Duvaut, G. & Lions, J.L., *Inequalities in mechanics and physics*, Springer, Berlin, 1976.

[25] Dracos, T., Theoretical considerations and practical implications on the infiltration of hydrocarbons in aquifers. In *Proc. IAH Int. Symp. on Ground Water Pollution by Oil Hydrocarbons*, June 5-9, Prague, 1978, pp. 127-137.

[26] El-Kadi, A.I., Applicability of sharp-interface models for NAPL transport: 2. Spreading of LNAPL. *Ground Water*, **32** (1994) 784-793.

[27] Forsyth, P.A. & Shao, B.Y., Numerical simulation of gas venting for NAPL site remediation. *Adv. Water Resources*, **14** (1991), 354-367.

[28] Herrling, B. & Stamm, J., Numerical results of calculated 3D vertical circulation flows around wells with two screen sections for in situ or on-site aquifer remediation. In *Computational methods in water resources IX, Vol.1 : Numerical methods in water resources*, edited by T.F. Russel e.a., Elsevier Applied Science, London, 1992, pp. 483-492.

[29] Hulshof, J. & Vazquez, J.L., Self-similar solution of the second kind for the modified porous medium equation. *Eur. J. Appl. Math.*, **5** (1994) 391-403.

[30] Hulshof, J. & Vazquez, J.L., The dipole solution for the porous medium equation in several space dimensions. *Ann. d. Scu. Norm. Sup. d. Pisa*, Serie IV, **20** (1993) 193-217.

[31] Huyakorn, P.S., Wu, Y.S. & Park, N.S., An improved sharp-interface model for assessing NAPL contamination and remediation of groundwater systems. *J. Contam. Hydrol.*, **16** (1994) 203-234.

[32] Ji, W., Dahmani, A., Ahlfeld, D.P., Lin, J.D. & Hill III, E.H., Laboratory study of air sparging: air flow visualization. *Ground Water Mon. Rev.*, **13** (Fall 1993), 115-126.

[33] Johnson, P.C., Kemblowski, M.W. & Colthart, J.D., Quantitative analysis for the cleanup of hydrocarbon-contaminated soils by in-situ soil venting. *Ground Water*, **28** (1990), 413-429.

[34] Johnson R.L., Johnson P.C., McWorther, D.B., Hinchee, R.E. & Goodman, I., An overview of in situ air sparging. *Ground Water Mon. Rev.*, **13** (Fall 1993), 127-135.

142

[35] Kaluarachchi, J.J. & Parker, J.C., An efficient finite element method for modeling multiphase flow. *Water Resour. Res.*, **25** (1989) 43-54.

[36] Kaluarachchi, J.J. & Parker, J.C., Multiphase flow with a simplified model for oil entrapment. *Transport in Porous Media*, **7** (1992) 1-14.

[37] Land, C.S., Calculation of imbibition relative permeability for two- and three-phase flow from rock properties. *Trans. Am. Inst. Min. Metall. Pet. Eng.*, **243** (1968) 149-156.

[38] Lenhard, R.J. & Parker, J.C., A model for hysteretic constitutive relations governing multiphase flow, 2. permeability-saturation relations. *Water Resour. Res.*, **23** (1987) 2197-2206.

[39] Lenhard, R.J. & Parker, J.C., Estimation of free hydrocarbon volume from fluid levels in monitoring wells. *Ground Water* **28** (1990) 57-67.

[40] Leverett, M.C., Capillary behavior in porous solids. *Trans. Am. Inst. Min. Metall. Pet. Eng.*, **142** (1941) 152-169.

[41] Lundegard, P.D. & LaBrecque, D., Air sparging in a sandy aquifer (Florence, Oregon, U.S.A.): Actual and apparent radius of influence. *J. Contam. Hydrol.*, **19** (1995) 1-27.

[42] Marley, M.C., Hazebrouch, D.J. & Walsh M.T., The application of in situ air sparging as an innovative soils and ground water remediation technology. *Ground Water Mon. Rev.*, **12** (Spring 1992) 137-145.

[43] McCray, J.E. & Falta, R.W., Defining the air sparging radius of influence for groundwater remediation. *J. Contam. Hydrol.*, **24** (1996) 25-52.

[44] Miller, E.E., Similitude and scaling of soil-water phenomena. In *Applications of soil physics*, edited by D. Hillel, Academic Press, New York, 1980.

[45] Miller, C.A. & Van Duijn, C.J., Similarity solutions for gravity-dominated spreading of a lens of organic contaminant. In *Environmental studies: mathematical, computational and statistical analysis*, edited by M.F. Wheeler. IMA Volumes in Mathematics and its Applications, Vol. 79, Springer-Verlag, New York, 1995.

[46] Mohtar, R.H., Wallace, R.B. & Segerlind, L.J., Finite element simulation of oil spill cleanup using air sparging. In *Computational methods in water resources X, Vol. 2*, edited by A. Peters e.a., Kluwer Academic Publishers, Dordrecht, 1994, pp. 967-974.

[47] Parker, J.C., Lenhard, R.J. & Kuppusamy, T., A parametric model for constitutive properties governing multiphase flow in porous media. *Water Resour. Res.*, **23** (1987) 618-624.

[48] Parker, J.C. & Lenhard, R.J., A model for hysteretic constitutive relations governing multiphase flow, 1. saturation-pressure relations. *Water Resour. Res.*, **23** (1987) 2187-2196.

[49] Parker, J.C. & Lenhard, R.J., Vertical integration of three-phase flow equations for analysis of light hydrocarbon plume movement. *Transport in Porous Media*, **5** (1989) 187-206.

[50] Pattle, R.E., Diffusion from an instantaneous point source with a concentration-dependent coefficient. *Quart. J. Mech. Appl. Math.*, **12** (1959) 407-409.

[51] Payatakes, A.C., Dynamics of oil ganglia during immiscible displacement in water-wet porous media. *Ann. Rev. Fluid Mech.*, **14** (1982) 365-393.

[52] Peletier, L.A., The porous medium equation. In *Applications of Nonlinear Analysis in the Physical Sciences*, edited by H. Amann e.a., Pitman Advanced Publishing Program, London, 1981.

[53] Philip, J.R., Horizontal redistribution with capillary hysteresis. *Water Resour. Res.*, **27** (1991) 1459-1469.

[54] Proskurowski W., A note on solving the Buckley-Leverett equation in the presence of gravity. *J. Comput. Phys.*, **41** (1981) 136-141.

[55] Protter M.H. & Weinberger, H.F., *Maximum principles in differential equations*, Prentice-Hall, London, 1967.

[56] Richards, L.A., Capillary conduction of liquids through porous mediums. *Physics*, **1** (1931) 318-333.

[57] Unger, A.J.A., Sudicky, E.A. & Forsyth, P.A., Mechanisms controlling vacuum extraction coupled with air sparging for remediation of heterogeneous formations contaminated by dense nonaqueous phase liquids. *Water Resour. Res.*, **31** (1995) 1913-1925.

[58] Van Duijn, C.J. & Peletier, L.A., A class of similarity solutions of the nonlinear diffusion equation. *Nonlinear Anal. Theory Methods Appl.*, **1** (1977) 223-233.

[59] Van Duijn, C.J., Molenaar, J. & De Neef, M.J., The effect of capillary forces on immiscible two-phase flow in strongly heterogeneous porous media. *Transport in Porous Media*, **21** (1995) 71-93.

[60] Van Duijn, C.J. & De Neef, M., Similarity solutions for capillary redistribution of two phases in a porous medium with a single discontinuity. *Adv. Water Resour.* (1997) in press.

[61] Wehrle, K., In-situ cleaning of CHC contaminated sites: model-scale experiments using the air injection (in-situ stripping) method in granular soils. In *Contaminated soil '90*, edited by F. Ahrendt e.a., Kluwer Academic Publishers, Dordrecht, 1990, pp. 1061-1062.

[62] Wilson, D.J., Norris, R.D. & Clarke, A.N., Ground water cleanup by in-situ sparging X : Air channeling model for biosparging of nonaqueous phase liquid. *Sep. Sci. Technol.*, **29** (1994) 1357-1376.

[63] Wu, Y.-S., Huyakorn, P.S. & Park, N.S., A vertical equilibrium model for assessing nonaqueous phase liquid contamination and remediation of groundwater systems. *Water Resour. Res.*, **30** (1994) 903-912.

[64] Wu, Y.-S., Forsyth, P.A. & Jiang, H., A consistent approach for applying numerical boundary conditions for multiphase subsurface flow. *J. Contamin. Hydrology*, **23** (1996) 157-184.

[65] Yortsos, Y.C., A theoretical analysis of vertical flow equilibrium. *Transport in Porous Media*, **18** (1995) 107-129.

Samenvatting

Eén van de grootste bedreigingen van ons milieu is verontreiniging van de bodem. Wanneer verontreinigende stoffen adsorberen aan bodem-deeltjes of ingevangen blijven in de bodem-poriën en daarna slechts langzaam weer desorberen of oplossen, kunnen ze jarenlang gewassen blijven aantasten en het grondwater besmetten. Daarom is sanering van verontreinigde bodems van groot belang. Zo mogelijk gebeurt dit in-situ, dat wil zeggen op de locatie van de verontreiniging zelf, omdat dit relatief goedkoop is.

In dit proefschrift worden verontreiniging met organische vloeistof of 'non-aqueous phase liquid' (NAPL), verwijdering van deze verontreiniging door middel van afpompen en reiniging van de bodem door middel van injectie van lucht in grondwater bestudeerd. De techniek van luchtinjectie of 'air sparging' bevordert vervluchtiging en biologische afbraak van organische verontreinigingen. In al deze situaties vereist een effectieve sanering grondige kennis van het gedrag van de fasen water, verontreinigende vloeistof en lucht in de bodem. Dit gedrag wordt beschreven met zogeheten meer-fasen stromingsmodellen, omdat er sprake is van meer dan één naast elkaar voorkomende fasen die verondersteld worden onderling niet oplosbaar te zijn.

Met behulp van een numeriek meer-fasen stromingsmodel wordt in twee dimensies, al dan niet axiaalsymetrisch, de tijdsafhankelijke stroming van de verschillende fasen berekend. Nauwkeurige simulaties vergen echter veel rekentijd. Daarom worden de afzonderlijke problemen met behulp van passende aannames gereduceerd tot deelproblemen die een lagere geometrische dimensie hebben of de stationaire tijdsonafhankelijke situatie beschrijven. Daarnaast domineert steeds één fase het totale stromingsprobleem, zodat alleen bestudering van het gedrag van die fase noodzakelijk is. De zogeheten analytische oplossingen van deze deelproblemen bieden gewoonlijk meer inzicht in het stromingsgedrag dan de numerieke resultaten en leveren relatief simpele relaties tussen invoer- en uitvoer-parameters.

In drie van de vier gevallen wordt gebruik gemaakt van 'gelijkvormigheidsoplossingen', wat simpel gezegd betekent dat in termen van plaats- en tijds-afhankelijkheid de vorm van de oplossing op ieder tijdstip hetzelfde is, maar dat de grootte met de tijd verandert. Voor toepassing van deze expliciete of bijna expliciete oplossingen op praktijkproblemen worden relatief gemakkelijk meetbare criteria geformuleerd. Zo wordt onder andere gebruik gemaakt van de totale massa van de onderzochte fase die op een bepaald moment in het systeem aanwezig is.

Hoofdstuk 2 beschrijft het gedrag van organische vloeistof die lichter is dan water en die zich als een zogenaamde drijflaag op een horizontale grondwaterspiegel bevindt. De oorspronkelijk dikke laag zakt onder invloed van

de zwaartekracht in horizontale richting uit. Daardoor wordt in het centrum van de laag de verzadiging met organische vloeistof steeds kleiner en vindt zogeheten 'entrapment' plaats waarbij de verontreiniging druppelsgewijs wordt ingesloten in de poriën-structuur van de bodem. Deze insluiting zorgt dat de verontreiniging immobiel is en bemoeilijkt de sanering. De snelheid waarmee de laag in horizontale richting uitspreidt en de hoeveelheid organische vloeistof die ingesloten raakt, worden geanalyseerd als functie van de verschillende bodem- en vloeistofparameters.

Hoofdstuk 3 beschrijft verwijdering van een drijflaag via een ontrekkingsfilter of gegraven sloot. Omdat bij onttrekking hooguit de hoeveelheid maar niet de samenstelling van de onttrokken vloeistof kan worden opgelegd, wordt speciale aandacht besteedt aan implementatie van randvoorwaarden die deze onttrekking goed beschrijven. De onttrekkingssnelheid en de horizontale uitbreiding van de overblijvende verontreiniging worden onderzocht.

In hoofdstuk 4 wordt een meer-fasen model geformuleerd voor injectie van lucht in grondwater via een verticaal injectiefilter. Hierbij wordt het gedrag van verontreinigende vloeistof buiten beschouwing gelaten, zodat de stroming van de twee fasen water en lucht overblijft. De lucht beweegt zich snel in verticale richting naar het grondwater-oppervlak door een zich in horizontale richting uitbreidende conus. De straal van deze conus, de invloedsstraal, bepaalt hoeveel injectiefilters nodig zijn om een bepaald gebied te reinigen. Voor de stationaire situatie waarin de hoeveelheid geïnjecteerde lucht gelijk is aan de hoeveelheid lucht die via de grondwaterspiegel verdwijnt, worden de invloedsstraal en de luchtverzadigingen binnen de conus berekend.

Hoofdstuk 5 beschrijft luchtinjectie in grondwater in een horizontaal gelaagde bodem met een goed doorlatende laag onder een minder goed doorlatende laag. Door het verschil in doorlatendheid spreidt geïnjecteerde lucht zich vlak onder het scheidingsvlak tussen de twee lagen ver uit in horizontale richting. Hierdoor wordt de invloedsstraal groter, maar worden de luchtverzadigingen in de slecht doorlatende laag aanzienlijk kleiner. Deze grootheden, die de effectiviteit van de luchtinjectie-operatie bepalen, worden geanalyseerd als functie van onder andere het verschil in doorlatendheid.

Curriculum vitae

Marinus Izaäk Jan van Dijke werd op 6 juli 1968 geboren te Vlissingen. Hij behaalde in 1986 het VWO-diploma aan de Christelijke Scholengemeenschap Walcheren te Middelburg. Van 1986 tot 1992 volgde hij de studie Technische Wiskunde aan de Technische Universiteit Delft. In 1992 studeerde hij af bij de vakgroep Algemene Wiskunde.

Van 1 december 1992 tot 1 januari 1997 was hij als Onderzoeker in Opleiding werkzaam aan de Landbouwuniversiteit Wageningen bij de Vakgroep Bodemkunde en Plantenvoeding in het kader van het onderzoeksproject van de Nederlandse Organisatie voor Wetenschappelijk Onderzoek (NWO) getiteld 'Nonlinear Transport Phenomena in Porous Media'. Vanaf 1 februari 1997 is hij als projectmedewerker in dienst bij het Centrum voor Wiskunde en Informatica te Amsterdam in het kader van het Nederlands Onderzoeksprogramma Biotechnologische In-situ Sanering.

De resultaten van het promotie-onderzoek in Wageningen zijn terug te vinden in dit proefschrift.

Nawoord

Na afronding van dit proefschrift is het goed om terug te blikken op mijn OIO-tijdperk en enkele personen met name te noemen die daarin een rol hebben gespeeld.

In het voorstel voor het NWO-project 'Niet-lineaire transport-verschijnselen in poreuze media', gecoördineerd door Hans van Duijn, werd onder het kopje 'oil spills' melding gemaakt van een promovendus die in Wageningen onder leiding van Sjoerd van der Zee onderzoek zou gaan verrichten. Ik heb die onderzoeksplaats gekregen en ik stelde mezelf ten doel om mijn wiskundige kennis uit Delft in het Wageningse milieu-onderzoek toe te passen.

Het is vooral Hans van Duijn geweest, die direct of indirect de specifieke onderwerpen voor het onderzoek heeft aangedragen. In eerste instantie kwam hij met 'air sparging' op de proppen, een techniek die pas later populair is geworden in Nederland en waar ik mijn huidige NOBIS-contract aan heb te danken. Via het werk van Clarence Miller en Hans kwam ik terug bij het oorspronkelijke onderwerp 'oil spills', wat resulteerde in de drijflaag-artikelen. Daarnaast ben ik Hans erkentelijk voor zijn inbreng op het gebied van partiële differentiaalvergelijkingen.

Op de Wageningse 'werkvloer' was het vooral Sjoerd met wie ik in de overwegend chemische omgeving van de vakgroep Bodemkunde en Plantenvoeding de fysische aspecten van het onderzoek grondig bediscussiëerde. Verder heeft hij steeds kritisch meegekeken bij het schrijven van de artikelen en geholpen bij allerlei voorkomende aangelegenheden rondom het onderzoek, zoals het voorbereiden van presentaties voor congressen.

Op vakinhoudelijk gebied wil ik ook Michel de Neef expliciet bedanken voor de gevoerde discussies over stroming in gelaagde bodems. Daarnaast zijn er nog veel anderen, onder meer bij Wiskunde en bij Mijnbouw in Delft en bij het CWI in Amsterdam, die meegeholpen hebben bij het onderzoek.

Of ik ben geslaagd in mijn opzet om wiskunde in te brengen in het Wageningense milieu-onderzoek, laat ik graag aan de lezers van dit proefschrift over. Naast het bezig zijn met mijn eigen onderzoek heb ik het leuk gevonden om deze en gene bij de vakgroep te helpen bij het oplossen van zijn of haar 'sommen' en Richard Walet en Robert Huiberts bij de begeleiding van hun afstudeervak 'bodemhygiëne en bodemverontreiniging'.

De vakgroep wordt voor mij gepersonifiëerd door Frans de Haan, die mij ook geholpen heeft bij alle formaliteiten rond de promotie. Ik bedank met hem de medewerkers van de vakgroep voor hun collegialiteit.

Omdat ik niet altijd even handig ben met computers, heb ik veel te danken aan de ondersteuning op dit gebied door Ron Beuger en later door Joost de Groot in Wageningen en door Gerard van Hoorn in Delft. En zonder de en-

thousiaste hulp van LaTeX-er Chris van Uffelen had dit boekje er waarschijnlijk een stuk minder mooi uitgezien.

Op 'sociaal' gebied wil ik speciaal mijn waardering uitspreken voor de collega's uit 'de kelder', die mij onder andere consequent bleven uitnodigen voor de lunch, ook al gaf ik er zelf vaak de voorkeur aan om mijn boterhammen op mijn kamer te nuttigen.

Buiten het werk was het mijn vrouw Margrethe die me geholpen heeft om het hele onderzoeksgebeuren wat te relativeren. Juist haar relativeringsvermogen zorgde voor de motivatie om met frisse moed verder te gaan op momenten dat het onderzoek weer eens dreigde vast te lopen. Vrijwel tegelijk met de geboorte van onze dochter Anne werd ook dit boekje 'geboren'. Het leek me daarom goed om het proefschrift aan haar op te dragen.

Rink van Dijke

Ede, oktober 1997